# Geometry Based Prediction of Laminar Flow Characteristics through Non-Homogeneous Porous Media

A Thesis submitted in fulfilment of the requirements for the Degree of a Master in Engineering specialising in Mechanical Engineering at the University of Canterbury


David Collinson

Department of Mechanical Engineering
University of Canterbury
Christchurch, New Zealand
November 2015

# Table of Contents

# Acknowledgements

Firstly, I would like thank my Supervisor Dr Sid Becker for providing me with the opportunity to undertake the thesis presented here as well as the continued discussions and cups of coffee provided during its completion.

Sincere thanks must also go to the University of Canterbury and its Masters Scholarship program, which was the source of funding for this thesis.

Additional mention must also go to my office mates Jeremy and Brad who were always able to help keep the mood light and occasionally provide helpful suggestions.

Finally and most importantly, I have to thank my Mum and Dad whose belief that I have the ability to achieve what I set my mind to has been a source of comfort and confidence for 22 years.

# Abstract

The prediction of flow rate and local pressure for Darcian flow through porous media that is non-homogenous in the direction of bulk fluid flow has previously been achieved through the use of numerical simulations. This thesis develops a model to predict Darcian flow behaviour by building a non-dimensional representation of flow through Cartesian geometries that are non-homogeneous along the direction of bulk flow. To construct the model, simulations were conducted in COMSOL™ by numerically modelling laminar flow through a tortuous Cartesian geometry and then normalising the results to produce a non-dimensional representation of flow behaviour as a function of the geometry. Through this method the permeability of the simulation domain was related to geometrical parameters. By splitting the geometry into simply defined 'blocks' the relationship between the permeability of the block to fluid flow was clearly defined with regard to the characteristic block length. The simulations were conducted across two case studies.

The first case study examined the flow characteristics through a geometry with the characteristic length varying along the direction of bulk fluid flow. The major outcome of this case study was to prove that the block permeability was proportional to the square of the characteristic length of the block. In addition it is shown that the when the geometry varies, the flow rate and local pressure through a tortuous series of connected non-homogeneous blocks could be predicted using a linear equation within a maximum error of -0.4% and ~2 Pa (when the total pressure drop was 1000 Pa) respectively.

The second case study expanded the length variation to include the variation of the characteristic lengths perpendicular to the direction of bulk fluid flow. The resulting data was used to create a model that successfully predicts the permeability, flow rate and local pressure through tortuous geometries that are non-homogeneous parallel and perpendicular to the path of bulk fluid flow. Local pressure was predicted with a maximum error of 2.5 Pa.

The model developed in this thesis provides the foundation for developing a method that could decouple Fluid-Solid interface simulations in the field of deformable porous media, other future directions for this research are also discussed. Currently, the method can provide a tool to predict Darcian flow through non-homogeneous porous media.

# Nomenclature

| Symbol | Definition |
|---|---|
| $A$ | Area |
| $a_0$ | Case Study Two: y-intercept correlation coefficient |
| $a_1$ | Case Study Two: linear correlation coefficient |
| $a_2$ | Case Study Two: quadratic correlation coefficient |
| $b_1$ | Case Study 1: linear correction coefficient |
| $b_0$ | Case Study 1: constant correction coefficient |
| $C_\varepsilon$ | Case Study 1: linear correlation coefficient |
| $C_0$ | Case Study 1: y-intercept correlation coefficient |
| $f$ | Friction factor |
| $h_m$ | Head loss |
| $K$ | Permeability |
| $\Delta K$ | Change in permeability |
| $K_L^P$ | Predicted local permeability |
| $K_L^S$ | Simulated local permeability |
| $L$ | Length |
| $\Delta L$ | Change in length |
| $L_0$ | Un-deformed pore length |
| $P$ | Local pressure |
| $\Delta P$ | Pressure drop |
| $Q$ | Flow rate |
| $Q_G^P$ | Predicted global flow rate |
| Re | Reynolds number |
| $\vec{V}$ | Fluid velocity |
| $\forall$ | Volume |
| $z$ | Location in direction of bulk fluid flow |
| $\beta$ | Forcheimer coefficient |
| $\varepsilon$ | Length variation |
| $\Delta\varepsilon$ | Length variation change |
| $\mu$ | Dynamic viscosity |
| $\nu$ | Variation ratio |
| $\rho$ | Density |
| $\tau$ | Tortuosity |
| $\phi$ | Porosity |

# 1 Introduction

Fluid permeates and flows through materials with complex micro-scale structures in numerous engineering applications. Some examples are geological materials, microfluidic devices, biological materials such as bone, metal foams and composites with a viscoelastic fluid. Some of these examples require design and development to optimise them for intended applications. For other examples such as the geological and biological materials, it is important to understand the flow behaviour of the fluid through these materials in an effort to understand the natural world as well as improve the ability to design methods that are able to improves processes such as oil and gas extraction, or bone regrowth and repair

The problem with complex geometries is that when researchers aim to study fluid flow through them, simulation methods often become prohibitively computationally expensive. The problem becomes compounded when the geometry changes in response to the fluid flow. To be able to model this behaviour fluid-solid interface simulations are conducted. However not only are such simulations computationally expensive, but they are difficult to initialise. As such, a method that simplifies the simulation process would be very beneficial to analysing and designing flow characteristics through complex geometries. The complexity of a media geometry can arise from irregular and quasi-periodic flow paths (i.e. the characteristic geometric length of the pores within the media varies in the direction of flow), this thesis provides the groundwork to decouple the solid and the fluid domains in the simulation, as such simplifying the problem formulation greatly. Such a method would also look to be applicable to a wide range of different characteristic length scales within a particular class of geometries.

This thesis takes steps to develop a method that can predict flow characteristics through complex geometry. In this thesis, a predictive model has been developed that takes data from laminar flow simulations and normalises the resulting relationship between flow characteristics and the media geometry to allow the prediction of flow behaviour along non-homogeneous porous media. The non-homogeneity of the geometries examined arises from characteristic length scale variation in the direction of bulk fluid flow. To develop the model a non-uniform, quasi-periodic matrix in Cartesian space was developed and presented in this thesis that is used to illustrate the applicability of the developed predictive model. In the first of two case studies, the flow behaviour through the geometry is studied with the porosity of the media maintained at a constant value. In the second case study, the characteristic lengths of the geometry perpendicular to the fluid flow are altered so that the porosity varies along the direction of bulk fluid flow. Future development aims to use the local pressure prediction as a means to determine the deformation in the solid domain of the permeable material and apply it as a boundary condition for simulations to determine the length variation of the solid in response to fluid pressure. The deformation can be converted to a boundary condition to be used in the model

developed in this thesis to predict the local fluid pressure thereby successfully decoupling the fluid and solid domains and simplifying the simulation process.

## 1.1 Previous Research

The flow of fluid through the complex geometries and porous media has been examined at studied at length for decades. A key regime for understanding how the flow behaves was first defined in 1856 by Henry Darcy as part of his study on the flow of fluid through various soils. Darcian flow is a low Reynolds number regime that assumes that inertial effects are negligible and defines the flow rate as linearly proportional to the pressure gradient along the direction of bulk fluid otherwise known as Darcy's law. Over the 150 years since, Darcy's law has been developed to describe a greater range of Reynolds numbers and cases such as the Forcheimer regime [1] which deals with laminar flow where inertial effects are no longer negligible. Darcian flow through homogeneous media such as geological soils is greatly studied and techniques to predict, simulate or test flow characteristics through them are well established [2-4].

A major component of describing flow through such media is the impact of geometric parameters such as porosity on the fluid flow behaviour. Porosity is described as a ratio of void space to solid within a porous media and there has also been a large amount of work on describing how fluid behaviour changes as porosity changes homogeneously throughout the media [5, 6]. However, research is lacking in predicting flow characteristics in deformable porous materials where porosity is non-homogeneous through the media without resorting to computationally expensive simulations such as fluid-solid interactions (FSI).

A lack of work has been done on developing a simpler method to predict Darcian flow behaviour through non-homogeneous matrices without resorting to FSI simulations. While fluid-solid interaction simulations are an effective method for the investigation of fluid flow through non-homogenous porous media, the complexity and computational cost of FSI simulations prohibit the ability of CFD researchers to examine a wide range of cases studies and options as the process would take too long or is prohibitively complex. Out of this problem, a need is generated that allows for a simplified method to predict flow characteristics in deformable, non-homogeneous porous media without resorting to intensive simulation.

The potential benefit of developing a simplified method to predict Darcian flow in complex geometries extends beyond deformable porous media to microfluidic applications as well. If the flow characteristics can be predicted for a whole class of geometries based on the geometry of a representative sample, the amount of experimental and simulation work required for developing microfluidic devices for applications such as fuel cells and heat exchangers could be greatly reduced. A method that predicts flow based purely on geometric characteristics would allow for optimisation

of not just microfluidic devices, but deformable porous medias as well assuming that the interior pore structure is well defined.

## 1.2 Current Research

The proposed solution to this problem is a non-dimensional predictive equation that uses permeability as a resistance to predict volumetric flow rate and local pressure in a non-homogeneous geometry, i.e. a geometry that varies in porosity based upon the location inside the geometry. The inspiration for the geometry used in this thesis is based upon a geometry developed at the University of Canterbury for experimental research into deformable porous media. A major benefit of the geometry for the study conducted here is its well defined pore structure and well-posed dimensions that can be easily manipulated as required. In addition, it was able to be reduced through the use of suitable boundary conditions to reduce the domain that required numerical solving. To manipulate the dimensions a parameter termed the 'length variation' is developed for the study and can be used to ultimately control every aspect of the pore geometry.

This thesis describes the construction of a normalised model that relates length variation to permeability using taylor series expansion to identify the non-dimensional relationship. The commercial CFD package COMSOL v4.3b is utilised to provide simulation data for a wide range of geometry under different length variations, all of which are based on the Cartesian geometry. Once permeability is determined as a function of length variation, a summation equation is built that predicts local pressure along the length of the geometry by determining the required pressure drop across a specified interval. Then the final relationship is stress tested to determine the maximum error developed and the limitations of the model. The work concludes with discussion on what the next required steps for the model are and specific opportunities for application of the model in its current and potential future states.

The outline of this thesis describes a study that utilises CFD simulations of Darcian flow through local pore geometry in order to determine the relationship between permeability and local geometry. In turn the developed relationships can be used to predict the local and global flow behaviour based solely on predefined geometrical parameters of the porous media. Chapter 2 outlines the scope of the project and the objectives it aims to complete. Chapter 3 provides the background literature review to provide the necessary information to successfully develop the model and the geometry. Chapter 4 builds the simulation geometry based on the chosen 3-D matrix and develops its relationship with the length variation. Chapter 6 provides a comparison of two candidate methods for curve fitting empirical data: Method of Least Squares and Taylor Series approximation. Chapter 7 discusses the methodology used to conduct the simulations using COMSOL. Chapter 8 checks that the solution provided by COMSOL is converged and that assumptions made about the flow are valid. Chapter 9 provides the development and results of the model for the

constant porosity case. Chapter 10 provides the development and results of the model for the variable porosity case. Chapter 11 discusses what the required next steps are to optimise the method for deformable porous media and widen its applicability. Chapter 12 discusses the possibilities and long term applications for the predictive model. Finally Chapter 13 reiterates the key conclusions of this study. Appendix A and B provide additional data used in each case study to develop the figures and relationships presented in the bulk of the thesis. From Chapter 3, a short summary is given on the contents of the Chapter.

# 2 Thesis Objectives/Scope of the Predictive Model

As outlined in Chapter 1, the ultimate aim of the study is to provide a simplified alternative method for the prediction of fluid flow through complex geometries. Here key steps are taken to develop and understand the geometry to be used for investigation and then use the geometry to create simulation data that allows for non-dimensional relationships between the simulation geometry and the fluid flow to be identified. The work presented in this thesis focuses on the geometry and the method to generate the model and the application to variable and constant porosity cases. The main achievements of the thesis are:

- A developed model that can be used to provide a clear relationship between geometric parameters and flow characteristics (local pressure and flow rate) for non-homogeneous porous media.
- A method to extract simulation data from COMSOL™ and use it to relate flow characteristic to geometric parameters.
- Refinement studies that determined the accuracy of COMSOL™ software in modelling the flow field through the specified geometry and an assessment of the validity of assumptions required for a Darcian flow regime.
- Used the developed method to create an accurate non-dimensionalised prediction equation for pressure and flow rate for geometry with variable characteristic lengths and constant porosity in the direction of bulk flow.
- Used the developed method to create an accurate non-dimensionalised prediction equation for pressure and flow rate for geometry with variable characteristic lengths and variable porosity in the direction of bulk flow.
- Developed the prospective next steps for continuation of the prediction method for use in deformable porous media and other relevant applications.

The following aspects were outside the scope of this study and are not presented in this thesis:

- Creating an empirical model for the relationship between permeability and large length variation $(\varepsilon > 0.5)$.
- Developing the model for geometries outside of the developed Cartesian geometry (e.g. spherical or cylindrical unit cells).

# 3 Background

*A literature review was conducted that identified an opportunity to provide a solution for simple prediction of local pressure in complex, non-homogeneous geometries at the microscale without resorting to resource intensive computer simulations. The model was developed for the Darcy regime (Section 3.1) as an initial case due to its extensively supported linear relationship between pressure gradient and geometry. The concept of porosity* $(\phi)$ *and tortuosity* $(\tau)$*, their use in porous media, how they relate to the work conducted here were all discussed (Sections 3.1.1 and 3.1.2). The impact of minor losses on fluid flow through the geometry was discussed, particularly the contractions and expansions of the area perpendicular to fluid flow, changes in direction for the flow stream and entrance effects (Section 3.3). It was concluded that directional changes in fluid flow had negligible impact on fluid flow, any losses associated with expansion and contraction would be repetitive between blocks, and could be accounted for in the permeability calculation and that the entrance effects may be present in simulations, but are small enough that removing blocks at the inlet and outlet from analysis would sufficiently remove the impact of entrance effects on calculations. Frictional effects were also considered and thought to be linear with respect to pressure gradient. The reduced Navier-Stokes equations were presented for each flow regime. It is proposed that the Reynolds numbers intended for use in this study* $(\mathrm{Re} < 1)$ *are sufficiently low such that laminar or creeping flow could be assumed when conducting simulations (Section 3.1.3).*

## 3.1 Fundamental Background of Porous Media

A porous medium is defined as a matrix of solid material with interconnected void space. The presence of the connected space allows for the transport of a fluid through the medium. The simplest case, which is studied in this thesis is for the void space to be saturated with one Newtonian fluid (Single-Phase Flow). In general engineering applications, the porous medium can either be rigid, or undergo small length variation either through external forces, or as a result of driving fluid pressure as an interstitial fluid flow through the void space in the porous media. Description of the fluid flow through porous media is largely based on the length-scale that the investigation is conducted at. For a small length-scale, the investigation may only concern a singular channel, as is the case in this thesis. The alternative approach is to take a global view of the porous media and consider the effects of multiple channels and the overall properties of the porous media. At this length-scale, the impact of a single channel is difficult to understand, such is the complexity of porous media. Instead volume average methods and global parameters are used instead to describe the fluid-saturated media [7].

Pore structure parameters are important to consider as part of any analysis associated with porous media as a means to provide context to what particular case or cases have been studied. Within the field of deformable porous media,

there is huge variety in behaviour between specific cases (Section 12.1), the use of parameters such as porosity and tortuosity aim to make some means of categorising the variety of cases. Along with flow parameters (e.g. Reynolds Number and Forchheimer Number) a full description of behaviour can be made.

### 3.1.1 Porosity

Porosity $(\phi)$ is defined as the bulk volume fraction of a porous media that is occupied by fluid. The major difference between the case studies presented in Chapter 9 and 10 is that the porosity is constant for the geometry in Chapter 9 and variable in Chapter 10 [8, 9]. Dependent on the porous medium, the porosity can be as low as 0 and asymptotically approach 1. Porosity can be described by

$$\phi = 1 - (\forall_S / \forall_B) = 1 - (\rho_b / \rho_s) \tag{3.1}$$

where $\rho_b$ is the bulk density of the porous media and the $\rho_s$ is the density of the solid. $\forall_B$ and $\forall_S$ are the corresponding volume fractions representing bulk volume and volume occupied by the solid. The porosity of a media can range from very low porosities ($0 < \phi \leq 0.3$) for sedimentary materials such as shale and limestone, intermediate porosities ($0.3 < \phi \leq 0.8$) for soils and loose gravels and high porosities ($0.8 < \phi < 1$) for metal foams [10-13]. For this study, the porosity is maintained at intermediate values, the exact derivation for the porosity of the geometry used can be found in Section 5.3.1.

### 3.1.2 Tortuosity

The geometric characteristic of tortuosity is a measure of the distance that a fluid flowing through a media must travel to cross from Point A to Point B compared to distance travelled by the fluid if it instead flowed in a direct path [14, 15]. Tortuosity is a key geometrical characteristic that allows complex geometry pathways to be differentiated to straight channels and is denoted by $\tau$ . Figure 3-1 helps illustrate the difference between pathways with high tortuosity and low tortuosity. Tortuosity as well as porosity provide a mechanism for understanding how complex pathways increase the permeability of a media or channel beyond what is calculated for straight channels with similar pore characteristics.

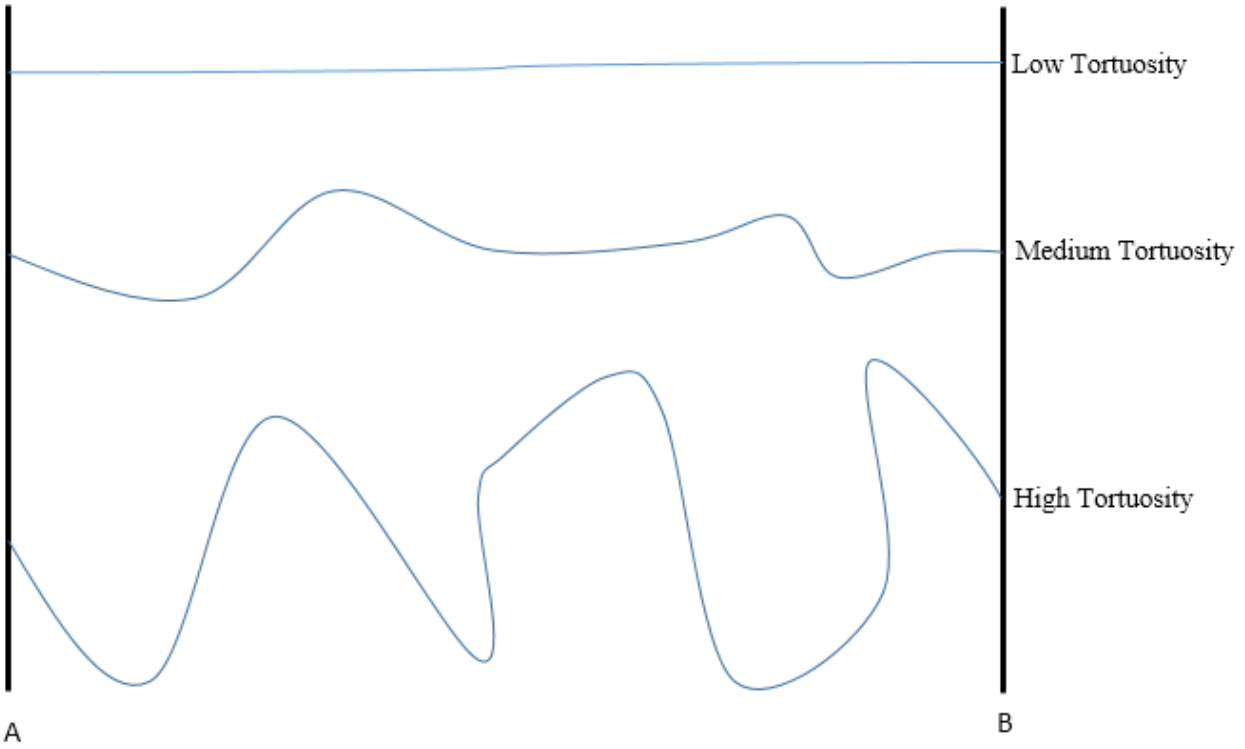


*Figure 3-1. Three fluid streams with low, medium and high tortuosity that illustrates how tortuosity increases with the length of the flow path required to traverse an equivalent distance*

The high tortuosity fluid path takes a much longer path than the medium tortuosity streamline, which in turn takes a longer path than the low tortuosity streamline cover the distance from line A to line B. From [13], tortuosity is defined as

$$\tau = \left( \frac{L}{L_e} \right)^2 < 1 \tag{3.2}$$

Where $L$ is the length from A to B. $L_c$ is the effective path length i.e. the length the fluid must actually travel. The squared term is developed from the concept that an increase in path length increases the driving force for fluid flow at the local scale as well as the fluid velocity in the streamline. For this definition, $\tau < 1$ as when $L = L_e$ , there is no tortuosity. An alternative definition is presented by Kutilek and Nielsen [14] where tortuosity is the ratio between the effective path length $(L_e)$ and the total length $(L)$.

$$\tau = \frac{L_e}{L} > 1 \tag{3.3}$$

Here tortuosity always greater than one and is the inverse of the relationship shown in (3.2). The tortuosity is equal to zero when $L_e = L$. Both of these definitions are based on the Kozeny-Carman model and are only applicable to saturated media and channels, such as the case in this study.

### 3.1.3 Reynolds Number

Here Reynolds number is developed for this study by examining its use in the context of porous media. The main reason to introduce Reynolds number in this manner is that Darcy's law is most frequently used in porous media, and that its main assumption that inertial effects in the fluid flow is negligible requires the Reynolds number to indicate that the flow is in the Laminar regime.

The use of Darcy's law (3.7) relies on viscous effects dominating inertial effects in the fluid to the point where the inertial effects can be ignored. Previous efforts have been made in literature to define the critical point at which Darcy's law is applicable [11, 16]. The main purpose of Reynolds number in the field of Deformable Porous media is to specify a flow regime for fluid as it moves though a medium. Due to the many different geometries and types of media that are defined and porous, there is great difficulty in determining an appropriate universal definition for Reynolds number [16]. Various studies have defined the Reynolds number differently as suited to the needs of the research. For each definition, an expression is given, and a critical value or range of values are given that specify the observed transition from the Forchheimer flow regime to the Darcy regime. A few are outlined here to give some context to the variety of ways Reynolds number is expressed. An exhaustive account was conducted in [16].

The classic definition for Reynold's number originates from the original experiments conducted by Darcy for water through various loose sediments. A formal definition was developed in [2]. Equation (3.4) describes the expression. The definition lends itself well to flow around immersed bodies, typical of groundwater as it moves through sediment composed of individual granules with a measureable diameter.

$$\mathrm{Re} = \frac{\rho D_p \overline{V}}{\mu} \tag{3.4}$$

$\rho$ is the density of the fluid. $D_p$ is the diameter of an individual particle in the porous media. $\overline{V}$ is the bulk fluid velocity, $\mu$ is the dynamic viscosity of the fluid. The most problematic aspect of (3.4) is what can be designated as the characteristic length to substitute in for $D_p$ in medias that do not have a well-defined or homogeneous particle diameter. The range of critical Reynolds numbers was shown to be 40-80. In this range, the flow is transitional between

the Forcheimer Regime and the Darcy Regime. Below a Reynolds number of 40, the flow is in the Darcy regime, above a Reynolds number of 80 the flow is in the Forcheimer regime.

A second definition seeks to remove the issue of having an ill-defined characteristic length by the replacing $D_p$ from to instead replace it with the square root of permeability $\left(\sqrt{K}\right)$ for the media [12]. Equation (3.5) describes the redefined definition.

$$\mathrm{Re} = \frac{\rho\sqrt{K}}{\mu}\overline{V} \tag{3.5}$$

Here $K$ refers to permeability, all other symbols used maintain the same definition as (3.4). For the definition presented in (3.5), the range of critical Reynolds numbers was shown to be approximately 0.1. A major problem with (3.5) is that to be able to determine the Reynolds number, the permeability of a media has to be known, this is not an easily measurable property and requires either experimentation or simulation to determine a value before $\mathrm{Re}$ can be calculated.

The final definition of Reynolds number moves away from the conventional description of a ratio of inertial and viscous forces to a definition that is based on porosity [6]. The new relationship is described in (3.6).

$$\mathrm{Re}_c = \frac{50.8\phi(1-\phi)^{1/3}}{c_d\left[1-(1-\phi)^{1/3}\right]} \tag{3.6}$$

Where $\mathrm{Re}_c$ is the critical Reynolds number, $\phi$ is the porosity of the medium, and $c_d$ is the dimensionless form drag coefficient. For the study in [6], the form-drag coefficient $(c_d)$ was determined to be 1.9. This definition approaches the problem from a global perspective where the flow velocity is high enough so that Darcy's law can no longer describe the pressure drop. This critical Reynolds number specifies the point of departure from the Darcy regime. At higher Reynolds number, the flow is in the Forcheimer regime, which is briefly described in Section 3.2. Other regimes are also used to describe special cases of flow which apply only to specific cases and geometries.

## 3.2 Darcian Regime and its Extensions

### 3.2.1 Darcian Flow

Darcy's law was developed in 1856 as part of research in the flow of fluids through various geological sediments [17]. Equation (3.7) describes the relations and describes a linear relationship between flow rate and the pressure drop

across a length of porous media. It is dependent on the assumption that the flow is incompressible and that the inertial effects of fluid transport are negligible [7, 13, 18].

$$Q = -\frac{K}{\mu}\frac{\Delta P}{\Delta L}A \tag{3.7}$$

In this equation $\Delta P/\Delta L$ is the pressure drop across a length in the direction of flow, $\mu$ is the dynamic viscosity of the fluid, $A$ is the cross-sectional area perpendicular to bulk fluid flow, and $Q$ is the volumetric flow rate. The coefficient $K$ is dependent on the geometry of the porous media and is known as the permeability of the medium [18]. Permeability is a measure of the conductivity of a porous medium with respect to penetration of the medium by a Newtonian fluid. In this respect it can be thought of as similar to Young's modulus as a measure of resistance. From literature it is found that the permeability $(K)$ is solely dependent on geometry at low Reynolds numbers [19, 20].

Two major approaches can be conducted to analyse the flow through a porous media. The first is to consider flow around objects immersed in the fluid, applicable for media with high porosities. The second is to consider flow inside channels through porous media, applicable for media with low-medium porosities. The second case is most applicable for the geometry present in the studies conducted for this thesis. The model created in Chapter 4 was developed neglecting fluid velocity in the *x* and *y* directions (the directions perpendicular to bulk fluid flow), resulting in a Hagen-Poiseuille flow.

### 3.2.2 Forcheimer Regime

The Forcheimer regime is based on high velocity flow of fluids through porous media which are fully saturated by a Newtonian fluid [10]. The pressure drop in the Forcheimer regime is described by Equation, which aims to modify Darcy's law (3.7) to include microscopic inertial effects that occur in fluid flow that operates above the critical Reynolds numbers discussed in Section 3.1.3.

$$-\frac{dP}{dz} = \frac{\mu u}{K} + \frac{\rho\beta}{\sqrt{K}}u^2 \tag{3.8}$$

Where $dP/dz$ is the pressure gradient in the direction of flow, $\mu$ is the viscosity of the fluid, $u$ is the mean velocity in the z-direction, $\rho$ is the fluid density, $\beta$ is the Forcheimer or inertial coefficient and $K$ is the permeability. This particular flow regime is out of scope for this study, but, the simple second-order term added to Darcy's law may allow for the empirical predictive model developed here to be extended to include flows that maintain Reynolds numbers within the Forcheimer regime.

### 3.2.3 Brinkman's Equation

Brinkman's equation is an alternative description to Darcy's law for the relationship between fluid velocity and pressure drop [7]. With the inertial terms omitted, Brinkman's equation takes the form.

$$\nabla P = -\frac{\mu}{K}\mathbf{u} + \tilde{\mu}\nabla^2\mathbf{u} \tag{3.9}$$

The Brinkman's equation, a second viscous term has been added. The first term in the LHS of the equation is the standard Darcy term, but the second term is analogous to the Laplacian term found in the Navier-Stokes equations. The $\tilde{\mu}$ term is the effective viscosity which is highly dependent on the structure of the porous media as well as the strength of fluid flow. However, Brinkman's equation is only valid for media with high porosity $(\phi > 0.6)$ and is therefore pretty limited in its scope and application to engineering materials.

### 3.2.4 Non-Newtonian Fluids

To allow for Darcy's law to be applicable to non-Newtonian fluids, the viscosity term $(\mu)$ has been altered in previous studies to increase the applicability of (3.7). One suggestion that was made was to replace $\mu$ with $(\mu^* / K^*)\upsilon^{n-1}\mathbf{u}$. Here $n$ is the power-law index, $\mu^*$ is the non-Newtonian coefficient for fluid viscosity, $K^*$ is the modified permeability and $\upsilon$ is the dynamic viscosity of the fluid.

## 3.3 Contributors to Pressure Loss for Darcian Flow

### 3.3.1 Inertial Effects

The geometry developed in Section 4.2.1, is a Cartesian geometry composed of blocks that interface in such a way that fluid flowing through the geometry undergoes a series of sudden expansions and contraction. In addition, the fluid velocity vectors periodically change direction along the proposed fluid path, due to the torturous path created by the complex geometry. For further development on the geometry refer to Chapter 4.

Previous studies have demonstrated that for low Re $(\mathrm{Re} < 100)$ the head loss caused by a change in fluid flow direction associated with a sharp bend in the geometry is negligible [21-23]. The flow regime for this study maintained at a much lower Re $(\mathrm{Re} < 1)$. Therefore, the effect of changes in fluid direction on the pressure drop across the tested geometry is ignored. The remaining source of losses that cause pressure drop is friction at the fluid-solid interface and the periodic expansion and contraction of the area open to fluid flow.

### 3.3.2 Expansion and Contraction

For fluid flow in enclosed systems, sudden expansions and contractions refer to step changes in a pipe of channel diameter [24]. In porous media, this is shown to be a significant component of pressure loss as a fluid moves through the media [2]. Whether a step change in pipe diameter is termed a sudden expansion or sudden contraction is based upon the whether the entrance or the exit is a finite reservoir. When the entrance is a finite reservoir, the change in diameters in termed a sudden contraction. When the exit is a finite reservoir, the change in diameters is termed an expansion. The relationship between head losses and the change in diameters is very well established, particularly so for sudden expansions. Equation (3.10) describes the relationship.

$$R_{SE} = \left(1 - \frac{d^2}{D^2}\right)^2 = \frac{h_m}{V^2/(2g)} \tag{3.10}$$

$R_{SE}$ is the loss coefficient, $d$ is the diameter of the pipe at the entrance, $D$ is the diameter of the pipe at the exit, $h_m$ is the head loss resulting from the sudden expansion, V is the velocity of the fluid moving through the sudden expansion, g is acceleration due to gravity. The relationship is similar for a sudden contraction, however the fluid dynamics has not been as well developed [24] and the loss coefficient is calculated using experimental data and the empirical formula in (3.11).

$$R_{SC} \approx 0.42\left(1 - \frac{d^2}{D^2}\right) \tag{3.11}$$

$R_{SC}$ is the loss coefficient for a sudden contraction, $d$ is the diameter of the pipe at the exit of the contraction, $D$ is the diameter of the pipe at the entrance to the contraction. (3.11) is used to predict the loss coefficient up until $d/D = 0.76$ above which it merges with the predictions made by (3.10). In the study presented, the influence of the sudden contractions and expansions in the geometry on the fluid is discussed and developed further using experimental data in Chapter 5.

### 3.3.3 Frictional Losses

Frictional losses are a major contribution to pressure drop that occurs across the individual blocks in the model. Here, friction is developed considering single phase flow through microscale channels. The flow is considered to be incompressible. The theoretical understanding of the behaviour of friction at this scale is the introduction of the friction factor $f$ . For this study, the Fanning friction factor will be used which is defined by (3.12) as the ratio of wall shear stress to the kinetic energy per unit volume of flow.

$$f = \frac{1}{2}\frac{\tau_w}{\rho \bar{V}^2} \tag{3.12}$$

$\tau_w$ is the wall shear stress, $\rho$ is the density of the fluid , $\bar{V}$ is the average velocity of the fluid. The friction factor can also be expressed in terms of pressure gradient and mass flow rate as shown.

$$f = \frac{\rho D_h}{2G^2}\frac{\Delta P}{\Delta L} \tag{3.13}$$

Where $\Delta P/\Delta L$ is the pressure gradient, $D_H$ is the hydraulic diameter, and $G$ is the mass flux. Equations (3.12) and (3.13) have both been shown to be applicable to flow in the Darcy regime. Especially important is that the frictions laws can be accurately predicted by the Navier-Stokes equations with classical no-slip boundary conditions [25, 26]. This has been shown to hold for channels larger than $4\mu m$ in height. The dimension used in this study has a length of $100\mu m$, several orders of magnitude larger than $4\mu m$ . Therefore, it is expected that Navier-Stokes models as discussed in Sections 8.1.1 and 8.1.2 will accurately model pressure drop for our chosen geometry compared to experimental conditions.

There are past studies that conducted experiments to determine the friction factor associated with micro-channels that determined that the friction factor for micro-channels deviated from classical theory. However it was shown that the studies that exhibited deviation from classical behaviour failed to account for entrance or exit effects and the losses that are associated with them [4]. It is important to consider the potential impact of not taking entrance effects into account for this study, as a model considering fully developed flow will not accurately represent the resistance of a single block affected by additional entrance or exit losses.

### 3.3.4 Entrance Effects

Entrance effects have caused issues in the past in determining pressure drop in microfluidic and porous media applications [11, 26, 27]. Here, the impact of entrance effects on experimentally and numerically determined values for pressure drops are investigated as to be aware of their potential contribution to pressure drop found in this study's numerical simulations. The configuration of the inlet, the inlet conditions, flow developments, and the viscous dissipation are all considered as 'entrance effects'[27]. These effects may be particularly pervasive in microfluidic applications where the channel length are typically quite short.

A study conducted by Koo and Kleinstreuer [27] concludes that the entrance effects in micrometre-scale channels, are dependent on channel length, aspect ratio and Reynolds number.. Entrance effects were shown to be most prevalent for short channels with high aspect ratios and Reynolds numbers. Here aspect ratio is defined as the height-to-width

ratio i.e. $\alpha = L_x / L_y$ for the study conducted in this thesis. The aspect ratio varies from 1 for a square cross-section to 0 for a parallel plate channel. Simulations conducted implied that channels with a square cross-section have the lowest friction factor within channels with rectangular cross sections. The reason provided for this is that as the aspect ratio decreases, the maximum centreline velocity of the channel also decreases. Therefore a smaller driving pressure gradient is required to accelerate the flow. The length variation $(\varepsilon)$ will alter the aspect ratio of the cross-section of the blocks in the second case study (Section 10). In this situation, the influence of aspect ratio on the friction factor for a block and therefore the additional resistance to flow must be considered.

The geometry used in simulations has a maximum $L/D_h$ of 16, placing the entire length of the geometry well within the specified range of entrance effect influence for what is admittedly comparatively high Reynolds numbers. The Reynolds numbers for flow used in this study are less than 1. This being the case, it is expected that the impact of entrance effects on the resistance of blocks to fluid flow may be minimal. Some analysis can be conducted during the study that compares the permeability of the blocks near the inlet and the outlet to those within the bulk of the geometry. The pressure drop may follow a where the rate of pressure drop for simulated local pressure gradient deviate at the inlet and outlet and maintains a constant value for the interior blocks.

From Koo and Kleinstreuer, there is clear deviation at the inlet and outlet of the channel, with approximately constant values for pressure gradient in the interior. It is expected that the simulation results in this study will provide similar, but less dramatically varied profiles as the Reynolds numbers of the fluid flow are maintained at values less than 1. If the permeability of blocks near the inlet and outlet are shown to deviate from the interior blocks, then permeability calculations based on simulation data may have to take into account the deviation. The method chosen here was to calculate values for permeability based on the pressure data for interior nodes, excluding the data for blocks at the inlet and outlet of the geometry.

# 4 Geometry of Porous Media

*This chapter describes a geometry for a single fluid flow path was developed based on a repeating on a regular three-dimensional Cartesian grid. The Cartesian grid can be described by quasi-periodic flow paths which are termed as 'elements' and are composed of four 'blocks' which are orientated in a quasi-periodic structure. The block geometries are defined such that their length scales vary in the direction of bulk fluid flow. A special case is also considered where the length scales vary in the direction transverse to fluid flow. The geometric parameters of the structure were expressed simply to assist in providing a clear relationship between the geometry and the pressure drop through the geometry. A new parameter was introduced called the length variation* $(\varepsilon)$ *(Section 4.2.2). The length variation was introduced to control the length of a block* $(L_z)$*. Another constant to control transverse variation with respect to longitudinal variation* $(\nu)$ *was introduced and used to relate the dimensions transverse to fluid flow (* $L_x$ *and* $L_y$*) to the length variation (Section 4.2.1). By doing this, the geometry had been developed such that all the dimensions of the block could be altered by changing the length variation.*

## 4.1 General Geometry

### 4.1.1 Unit cell structure

A unit cell system allows the application of permeability as a measure of resistance to fluid flow for each individual cell. Each cell is connected to two neighbouring cells through coincident faces, creating a domain consisting of discrete components. By allowing the geometry of each cell to be controlled, it is then possible to create a non-homogeneous structure where the resistance to fluid flow can be calculated for each individual cell. The combined resistances of each cell lead to an overall value that takes into account the individual contributions of cells connected along the length of the overall geometry. The permeability can be used as a functional cell property to relate fluid flow and pressure drop for each cell. A major aim of the study is to develop the cell in such a way that the permeability of a cell can be determined empirically solely from geometric parameters and then used as a resistance to predict the pressure drop across the cell.

To be able to determine the permeability of the geometry used in simulations, it is important to develop the geometry in such a way that all the parameters involved are strictly controlled. When a parameter is altered, it would be desirable for its relationship to permeability to be clearly evident. Especially important in this sense is to create a geometry for use in simulations that allows for a clearly defined $\Delta L$, and $A$ as defined in Chapter 5.

To this end the model developed for this study, is a two phase system is established in Cartesian space. A 3D geometry is created that consists of volume impervious to fluid flow, i.e. a solid and volume that allows for free transport of fluid through the geometry. In fundamental practice, each is a subdomain existing within an overall domain [29, 30].

### 4.1.2 Detailed Geometry Description

This study is focused on the flow through the porous media described by Figure 3-1. This particular structure is inspired by the deformable porous media developed in [31] and is based upon four repeating layers that consist of four variations of a base structure . Here, the solid represents volume permeable to fluid flow and empty space is impervious solid. Figure 4-2 describes a single 'element' which is comprised of four layers and is the smallest repeating element in the matrix. The four layer repeating pattern is created in two steps. Firstly, the rectangular volumes are shifted across one pore length ( $L_0$ ) in the *xy*-plane for the bottom two layers as shown in Figure 4-2 and Figure 4-3. Then, the second and fourth layers are rotated 90° clockwise so that the unit structure between adjacent layers are orthogonal. Placed on top of one another, the four layers comprise one 'element'.

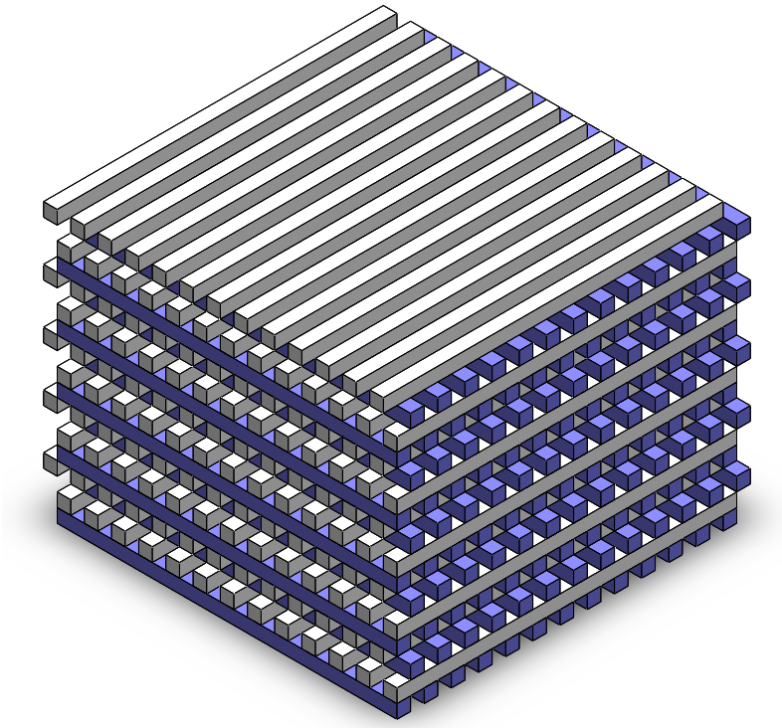

*Figure 4-1. A sample matrix comprised of 5 elements that describes the long range repetition of the layers*

This matrix architecture was chosen due to its simplicity while ensuring that there is no direct path for fluid flow through the geometry so as to introduce tortuosity into the flow channel. It is shown in Section 5.3 that the porosity

of this matrix is equivalent to $\phi = 0.5$. The geometry will be developed in Section 4.2.1 to be non-homogeneous, based on quasi-periodic elements where each layer in the media deviates from the original block dimension $(L_0)$.

Each layer consists of parallel equi-spaced rectangular solids where each gap between the permeable volumes is equal to the width of the permeable volume (i.e. the height and width are equal to $L_0$). Each dimension used to construct the layers are equivalent as shown in Figure 4-3.

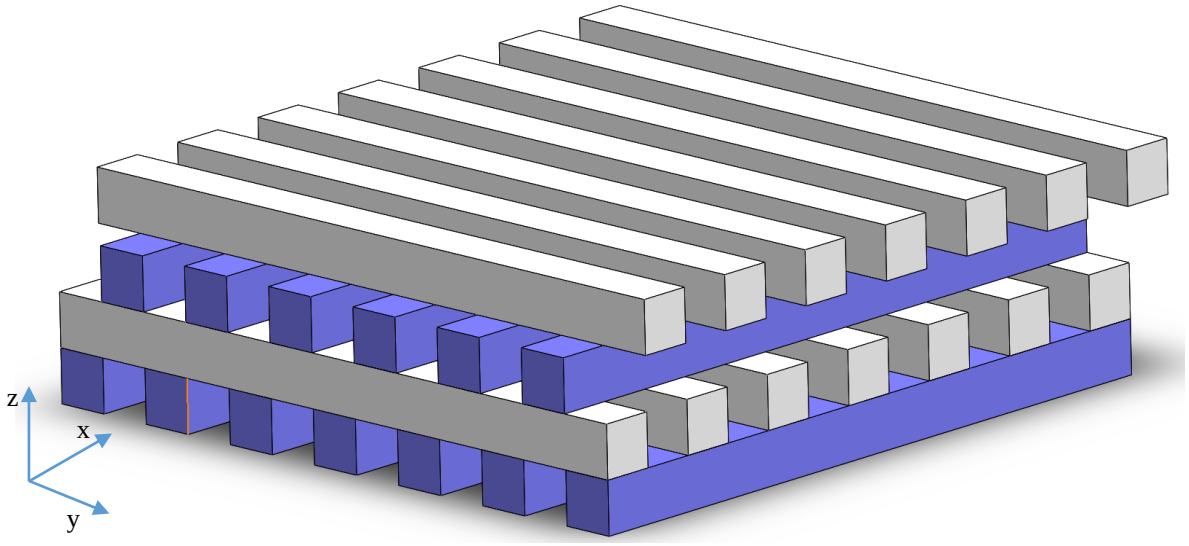


*Figure 4-2. A single element, which is the smallest repeating matrix pattern in the z-axis.*

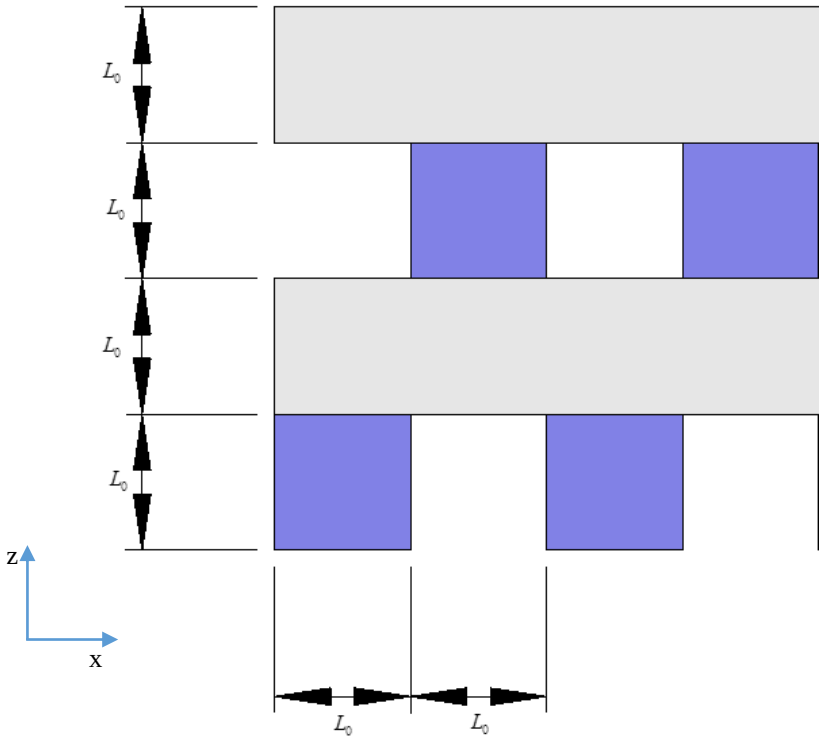


*Figure 4-3. An elevation view of a single element highlighting the dimensions used to construct the matrix*

Many models have been developed to determine flow characteristics though homogeneous porous medias such as these. The challenge arises when the media loses homogeneity. In this case, the pore dimensions are varied and can no longer be purely described through the use of $L_0$. Section 4.2 develops the matrix to have a controlled non-homogeneous nature.

## 4.2 Non-homogeneous Porous Media

A non-homogeneous porous media does not use equidistant pore lengths and the length-scales of the pores that make up a channel can vary along its length. An example of a non-homogeneous element is shown in Figure 4-4. Here, the height of each layer is reduced as the distance along the *z*-axis is increased. Here, a matrix made of the non-homogeneous elements is only quasi-periodic as long-range order is no longer guaranteed. Two major alterations are made to the dimensions in Figure 4-4. As mentioned, the height of the rectangular solids are reduced. In addition. The width of the rectangular solid is also reduced as the height reduces. The controlling relationships for the reduction of the height and width of the rectangular solid are developed in Section 4.2.3.

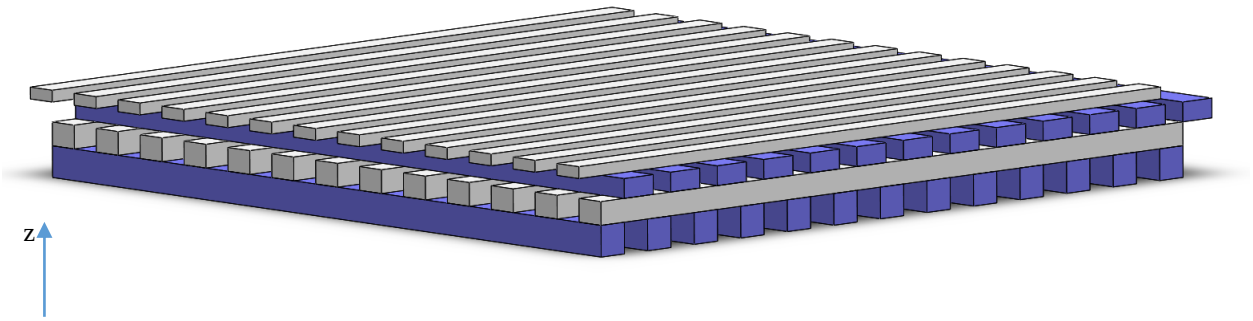


*Figure 4-4. Isometric view of a single element composed of non-homogeneous blocks*

As the dimensions are no longer constant they can no longer be universally described by $L_0$ . As such, new parameters need to be introduced that are defined in such a manner that they can represent the dimensions of the solid and pores across multiple non-homogeneous layers. Section 4.2.1 develops new parameters for the non-homogeneous layers.

### 4.2.1 Non-homogeneous Unit Cells

An important feature of this study is to develop an empirical prediction model that can cope with changes in geometry along the path of fluid flow that affect the permeability of the geometry to fluid. To facilitate this, several new constants and parameters are introduced here. The geometry is then developed to be dependent on introduced parameters.

To alter the layers to create non-homogeneous geometries, the geometry needs to be described by parameters that can easily be controlled. For this study a layer is described by the conventional, height and width. The side lengths of a single rectangular solid in a layers is described in Figure 4-5. Here the dimensions are labelled based on the axis they are parallel to. The main reason for defining the side length in this way is to simplify the description of the geometry used in simulations. The process behind reducing the geometry for use in simulation is outlined in Chapter 5.

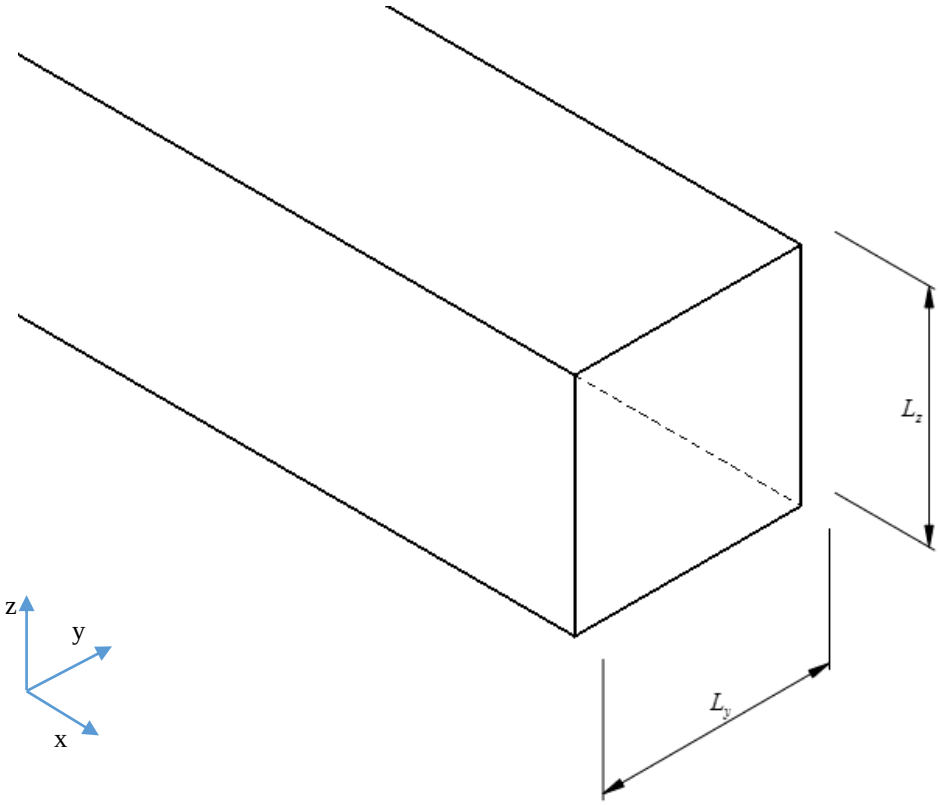


*Figure 4-5. Dimensions of a single 'block' in a layer.*

As shown, $L_z$ defines the height of the layer, and $L_y$ defines the width of a rectangular solid that is orientated perpendicular to the *y*-axis. The parameter $L_x$ denotes the width of a rectangular solid that is orientated perpendicular to the *x*-axis. To easily alter $L_y$ and $L_z$ a controlling parameter is introduced that linearly shortens the length of the dimensions as required during geometry initialisation for simulations. The process is explained in the following sections.

### 4.2.2 Length Variation

Here a new parameter is introduced called length variation, and is denoted by the symbol $(\varepsilon)$. The Length variation is inspired by compressive strain used in Mechanics of Materials [32]. For the purposes of this study, length variation is described as shown in (4.1) with respect to $L_z$.

$$\varepsilon = \frac{L_0 - L}{L_0} \tag{4.1}$$

$L_0$ (Section 4.1.1) is the value of the un-varied side length i.e. when $\varepsilon = 0$, $L_x = L_y = L_z = L_0$. $L_x$ is the varied side length for a given $\varepsilon$. By rearranging (4.1) a functional relationship can be derived that linearly relates $L_x$, $L_y$ and $L_z$ to $\varepsilon$.

$$\begin{aligned} L_z &= L_0\left(1-\varepsilon_z\right) \\ L_y &= L_0\left(1-\varepsilon_y\right) \\ L_x &= L_0\left(1-\varepsilon_x\right) \end{aligned} \tag{4.2}$$

Therefore as $\varepsilon$ increases, $L_x$, $L_y$ and $L_z$ decreases. In particular, $\varepsilon_z$ is the length variation parallel to the z-axis (the direction of bulk fluid flow), and $\varepsilon_x$ and $\varepsilon_y$ is the transverse length variation relative to the direction of bulk fluid flow. Equation (4.2) is used to control the side lengths of an individual block within a geometry. In Section 4.2.3 an additional parameter called the variation ratio is added to (4.2) to control the side lengths $L_x$ and $L_y$ with respect to $\varepsilon_z$. From this point, it possible to alter all the dimensions that describe a block in the geometry using $\varepsilon_z$.

### 4.2.3 Variation Ratio

The next step is to relate the transverse length variations ( $\varepsilon_x$ and $\varepsilon_y$ ) to the longitudinal length variation $\left(\varepsilon_z\right)$. Rather than make a direct correlation where $\varepsilon_x = \varepsilon_y = \varepsilon_z$, a variation ratio is used to control the magnitude of transverse length variation in response to a change in longitudinal length variation. The variation ratio is defined as

$$\nu = -\frac{\varepsilon_{lat}}{\varepsilon_{long}} \tag{4.3}$$

Where $\varepsilon_{lat}$ is the perpendicular (or transverse) variation, and $\varepsilon_{long}$ is the longitudinal strain. For the purposes of this study the variation ratio is defined as:

$$\nu = \frac{\varepsilon_x}{\varepsilon_z} = \frac{\varepsilon_x}{\varepsilon_z} \tag{4.4}$$

The relationships presented are maintained as positive due to the interaction between void spaces and solid in experimentation [19, 20]. As solids are compressed longitudinally ( $-\varepsilon_{long}$ ), they expand laterally. The solid expands into the void space reducing the cross-sectional area available to fluid transport. Therefore for this study, $L_x$ and $L_y$

must have a positive relationship to $\varepsilon_z$ so that when the solid is compressed the dimensions of the block lateral to fluid are also reduced. The geometry is developed such that the longitudinal length $(L_z)$ of both the solid and pore space reduce identically under for an increasing length variation. For the first case study (Section 9), $\varepsilon_x$ and $\varepsilon_y$ do not change with respect to $\varepsilon_z$, maintaining a geometry with constant porosity. For the second case study (Section 10), $\nu$ is given a value of 0.4 and then by subbing (4.4) into the system of equations presented in (4.2), a new system of equations is derived that relates all the layer dimensions to $\varepsilon_z$ and allows the porosity of the geometry to change . From (4.5), it can be seen that the lateral dimensions of the layers $L_x$ and $L_y$ decrease as the longitudinal length variation increases as desired.

$$\begin{aligned} L_z &= L_0(1-\varepsilon_z) \\ L_y &= L_0(1-\nu\varepsilon_z) \\ L_x &= L_0(1-\nu\varepsilon_z) \end{aligned} \tag{4.5}$$

The Elevation view shown in Figure 4-4 shows how $L_y$ and $L_z$ can be used to describe multiple non-homogeneous layers based on the labelled length variation stated for each layer. Now the dimensions of each layer in a matrix can be independently controlled and altered based on the length variation specified. At this point, the first major step in this thesis has been completed. A simple, non-homogeneous porous media has been developed with clear geometrical relations and easily controlled variables through the use of the introduced length variation. To progress to the next step in the study, the geometry was reduced to minimise the size of the computational domain that required solution. The main objective here is to reduce the matrix created to the smallest representative geometry possible to improve computation time. The integrity of the simulation esd maintained, and ensuref that the geometry used in simulation accurately models the fluid flow that would occur through the channels present in the overall matrix. The required steps for this process are conducted in Chapter 5.

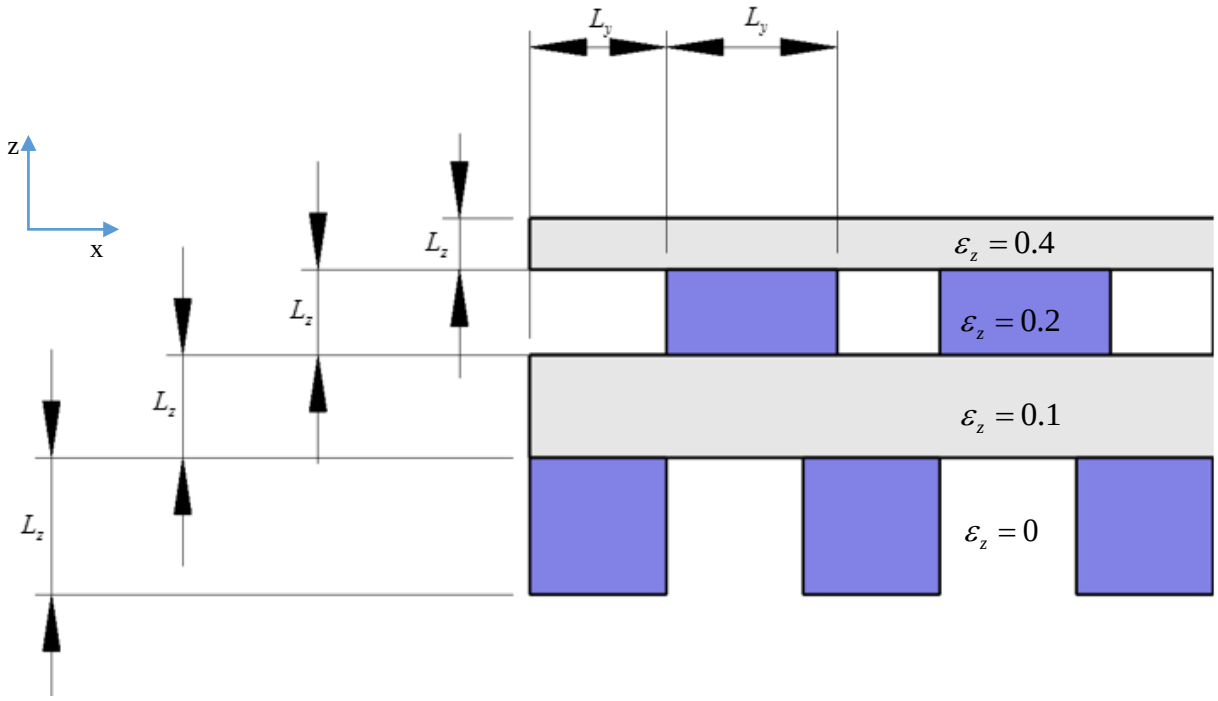


*Figure 4-6. Elevation view of a non-homogeneous element that highlights how the introduced parameter* $L_z$ *and* $L_x / L_y$ *can describe non-homogeneous layers*

# 5 Simulation Geometry

*In this chapter a single representative flow path is developed from the media described in Chapter 4. Preliminary simulations are conducted to observe the symmetry in the fluid flow through the media, which allows for the application of symmetry boundary conditions to reduce the simulation domain to a single representative flow path. The resulting geometrical representation of the domain and the parameters are given as well as the range of numerical values for the parameters that will be investigated in Chapters 9 and 10. Porosity for the un-varied geometry was determined to be 0.5 (Section 5.3.1). The response of these dimensions to an increasing length variation and the resulting impact on porosity was described. Particular attention was given to the cross-sectional area at the interface between two blocks and how this changes with respect to length variation. It was found that the area at the interface is proportional to* $\varepsilon^2$ *whereas the area for the bulk of the block is proportional to* $\varepsilon$ *. Therefore, the ratio of the between the block area and the interface area changes with respect to length variation. The potential implications of this on minor losses due to contraction and expansion along the flow stream were noted (Section 5.3.2).*

## 5.1 Introduction

The following sections describe the geometry used to model local flow through porous media. The flow path through the media is simulated in a representative channel that uses symmetry boundary conditions to reduce the size of the domain and improve computational time. Once the geometry has been reduced to a single representative flow field, the parameters used for the COMSOL simulation outlined in Chapter 7 are presented. These provide reference for parameter discussed in all following chapters. Finally the relationship between geometric parameters such as Porosity and the cross-sectional area of the pore are discussed in regards to how they are affected by a changing length variation, and how it may impact the behaviour of the fluid as it flows through the representative geometry.

## 5.2 Flow Field Symmetry

By showing that the flow through the matrix repeats over regular intervals it is acceptable to isolate the flow field to the single repeating unit, as it can successfully describe the behaviour of the flow at all other locations in the matrix. Figure 5-1 shows the process in isolating the flow field that accurately represents the flow throughout the matrix. A simulation is conducted in accordance with the process outlined in Chapter 7 for the matrix shown in Figure 4-1. The fluid flow streams are then plotted to visually show the fluid behaviour as it moves through the matrix.

The most notable feature is that the flow is separated into a distinct pattern, where a single flow path is mirrored about the planes of symmetry indicated. The elevation shown here is in the *zx*-plane, but an identical pattern can also be seen in the flow pattern if it is viewed from the *zy*-plane. Therefore, the flow field can be separated at the planes of

symmetry to create the single quasi-channel shown on the right hand side of Figure 5-1. By applying symmetry boundary conditions to the faces that lie in plane with the lines of symmetry, the geometry can be successfully reduced. The new quasi-channel geometry forms the basis of the geometry used in all the following simulations.

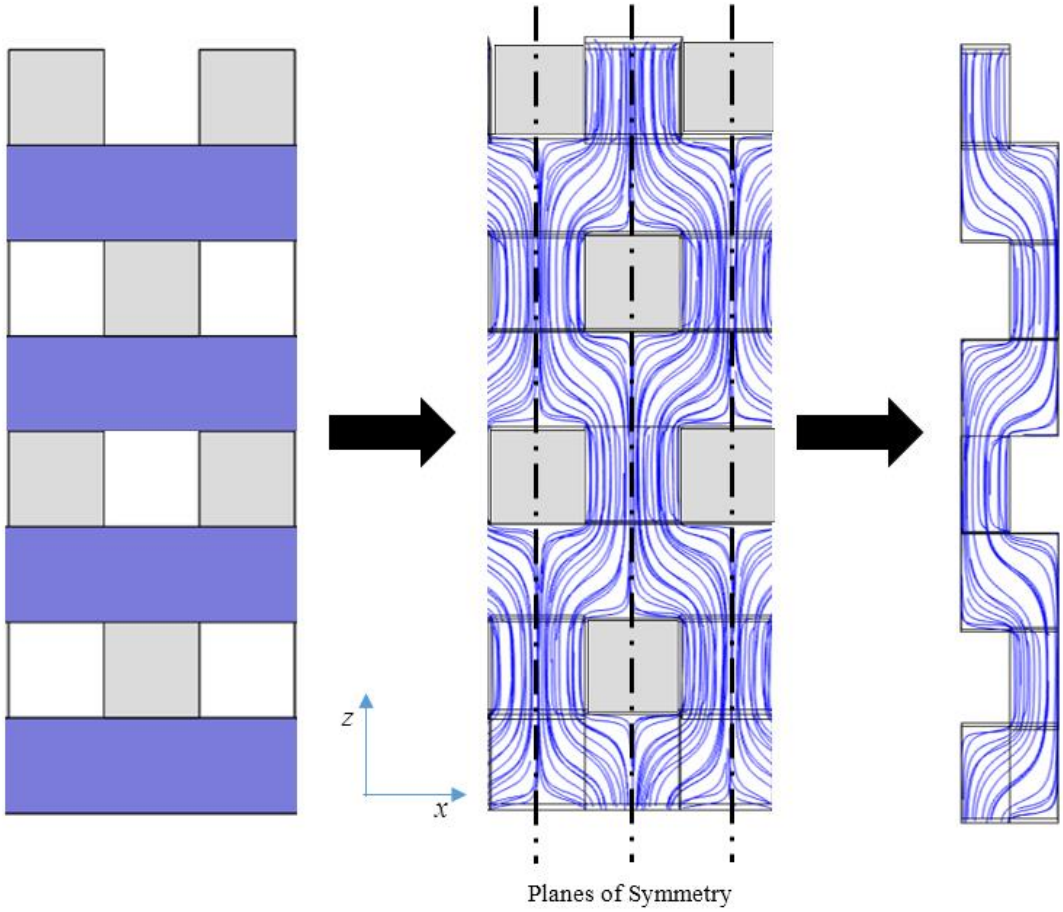


*Figure 5-1. Process showing reduction of geometry from left-to-right. zx-plane of the geometry in Figure 4-3. Simulated flow path through the geometry. The representative flow path that characterises the flow through the media.*

The quasi-channel derived from the matrix is shown from an isometric perspective in Figure 5-2. Fluid flows through the interior volume of the geometry shown. Excluding the inlet and the outlet, the symmetry boundary conditions are located on the outermost of the geometry surfaces and are coloured grey. The surfaces in contact with the solid are solid and have wall boundary conditions. The inlet and outlet are both noted, as well the two elements that make up this particular simulation geometry.

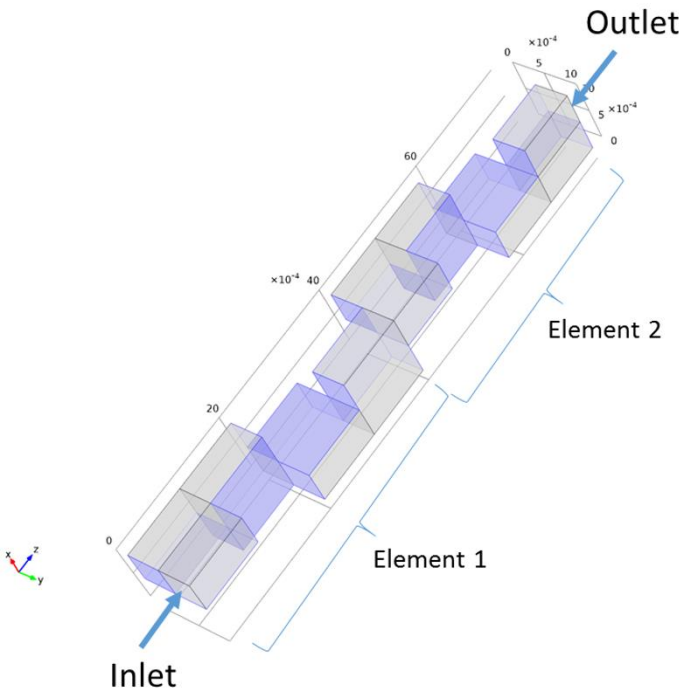


*Figure 5-2. Reduced geometry for use in simulation. The blue surfaces indicate where the flow is bound by walls. The grey surfaces indicate the planes of symmetry used to reduce the geometry.*

Table 5-1 lists the parameters used to describe the geometry. $L_0$ is the length of the pore sides before any length variation occurs. The $L_0$ value is used in the model construction to establish the working pore size for the model. $L_x$, $L_y$ and $L_z$ describe the size of the pore and are functions of the length variation $\varepsilon$ and $L_0$ as shown.

$$\begin{aligned} L_x &= L_y = L_0 \\ L_z &= L_0(1-\varepsilon_z) \end{aligned} \tag{5.1}$$

For this the constant porosity case study (Section 9), $L_x$ and $L_y$ remain independent of $\varepsilon$ as a means to simplify a potential relationship between geometrical parameters and permeability. A single value of area $(A)$ can be used for all varied lengths for a specified $L_0$ .The variable porosity case study (Section 10) considers the effect of $\varepsilon$ on $L_x$ and $L_y$ provides a developed understanding of the relationship between a variable geometry and permeability.

*Table 5-1. Parameters describing the geometry*

| Parameter | Symbol | Value(s) |
|---|---|---|
| Un-deformed Length Scale of fluid path | $L_o$ | $0.2 \le L_o \le 2.0mm$ |
| Length Scale of fluid path (x-direction) | $L_x$ | $0.2 \le L_o \le 2.0mm$ |
| Length Scale of fluid path (y-direction) | $L_y$ | $0.2 \le L_o \le 2.0mm$ |
| Length Scale of fluid path (z-direction) | $L_z$ | $0 < L_z \le 2.0mm$ |
| Variation Ratio | $\varepsilon$ | $0 \le \varepsilon \le 0.5$ |
| Area normal to fluid path | $A$ | $L_x \cdot L_y$ |

The range of values chosen for the length scales and length variations are chosen to maintain the assumptions made in the development of the predictive model. The key factor in determining the range of length scales used is to ensure that the Reynold's number is less than 1 $(\mathrm{Re} < 1)$ for all geometries tested. If Reynold's number is greater than 1 for a particular pore size, the assumption of creeping flow for the fluid model may no longer hold and Darcy's law can no longer be used [16]. Theoretically, the length variation $(\varepsilon)$ can be increased until it asymptotically approaches 1, but preliminary investigation suggests that the permeability deviates from its approximately linear behaviour with respect to length variations above 0.5 (Section 9). This being the case, the upper limit on length variations studied is set at 0.5. A length variation of 0.5 covers a vast majority of applications (Section 12.1), and it is unlikely to find an application that feasibly requires prediction of permeability for length variations greater than 0.5.

A point of note is that for this case study is that the porosity is constant no matter the un-varied pore length $(L_0)$ used or the length variation applied. From Dullien [18] porosity can be taken as

$$\phi = \frac{V_{liquid}}{V_{total}} = \frac{V_{liquid}}{V_{solid} + V_{liquid}} \tag{5.2}$$

If $L_x$ and $L_y$ are unaffected by $\varepsilon_z$ then the cross sectional area of the solid and the area normal to the path available to fluid flow will also remain constant and equal since $L_x = L_y = L_0$. Using these definitions (5.2) can be developed to show porosity is constant for all geometries in this case study as shown

$$\begin{gathered} \phi = \frac{V_{liquid}}{V_{solid} + V_{liquid}} = \frac{L_z \cdot A}{L_z \cdot A + L_z \cdot A} = \frac{L_z \cdot A}{L_z (A + A)} \\ \therefore \phi = \frac{A}{2A} = 0.5 \end{gathered} \tag{5.3}$$

Therefore all geometries tested in the case study will maintain a porosity of 0.5 or alternatively, the ratio of solid impermeable to fluid flow compared to volume in the geometry open to fluid flow will remain constant. The development of geometrical parameters for a model with variable porosity is shown in Section 5.3. For that case, the variation ratio is used to alter $L_x$ and $L_y$ for a given $\varepsilon_z$ .

## 5.3 Geometric Model with variation in lateral dimensions

The following section describes the development of the geometry from what was established in Section 5.2 to allow transverse length variation of the fluid path geometry in response to longitudinal length variation parallel to the direction of bulk fluid flow $(\varepsilon_z)$. To express the relation between transverse and longitudinal length variation additional terms are used. The parameters, their definitions as well subscripts used in developing the geometry are listed in Table 5-2

### 5.3.1 Parameters and cross-sectional area

*Table 5-2. Table of parameters and subscripts used to develop a geometry with variable porosity*

| Parameter | Value | Unit | Description |
|---|---|---|---|
| $L$ | $0.2 \rightarrow 1.0$ | $mm$ | Side length of a block that is open to fluid flow |
| $\varepsilon$ | $0 \rightarrow 0.5$ | - | Ratio of change in block length to the un-varied length |
| $\nu$ | $0 \rightarrow 0.49\dot{9}$ | - | Parameter that operates similarly to the variation ratio |
| $l$ | $0.2 \rightarrow 1.0$ | $mm$ | Side length of a block impervious to fluid flow |
| $\phi$ | $0.375 \rightarrow 0.5$ | - | Ratio of volume open to fluid transport over bulk volume in the geometry |

| Subscript | Description |
|---|---|
| $0$ | Refers to the un-varied state |
| $i$ | Refers to a block of interest in the geometry |
| $i+1$ | Refers to the next block along the direction of bulk fluid transport from the block of interest |
| T | Refers to parameters concerning the interface between two blocks |
| B | Refers to parameters concerning a single block |

Similar to the previous case study where models with constant porosity are considered, the adapted model to allow for variable porosity was also created in COMSOL™. However, some modifications were made to parameter expressions to allow for $L_x$ and $L_y$ to be affected by $\varepsilon$ . As with the model geometry in the constant porosity study, the block size is halved and a symmetry boundary condition is applied to the outer faces of the model. The construction and shape of the model is shown in. However the dimensions of the model in the *xy*-plane are now a function of the length variation $(\varepsilon_z)$. The derivation of this relationship is expressed in Section 5.3.2.

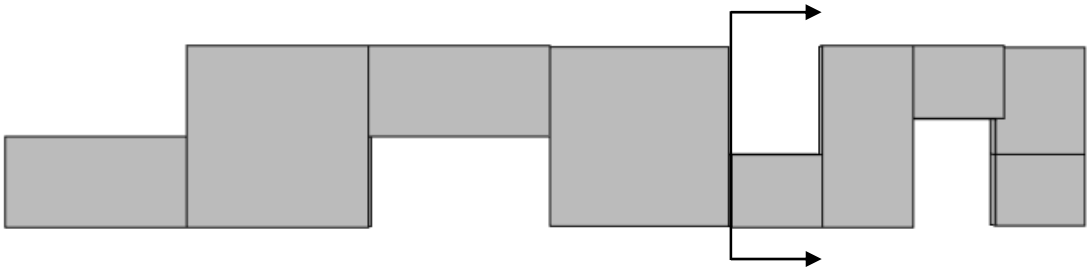


(Figure 5-4b)


*Figure 5-3. Exemplar model used in the variable porosity study. The first element has a length variation ( $\varepsilon_z$ ) of zero. The second element ( $\varepsilon_z$ ) has a length variation of 0.5*

### 5.3.2 Derivation of cross-sectional area with regards to length variation

A model with variable porosity is created by allowing the area normal to fluid flow to change as the length variation in the model is altered. For this study, the variation ratio is used to simulate the behaviour of materials under a compressive length variation. To allow this, three new parameters are created to describe length variation in the *xy*-plane, which are $L_0$ $\varepsilon_x$ and $\varepsilon_y$. The perpendicular length variations $\varepsilon_x$ and $\varepsilon_y$ are related to the longitudinal length variation by (5.4). $L_0$ is the un-varied pore length. In the constant porosity case study, $L_0$ was not required as $L_x$ and $L_y$ did not deviate from the predetermined pore length. Figure 5-4 provides a schematic representation of the geometry that exists at the transition between two blocks where each block is experiencing a different length variation as described.

$$\Delta\varepsilon_{xx} = \Delta\varepsilon_{yy} = -\nu\Delta\varepsilon_{zz} \tag{5.4}$$

If $L_x$ is related to $L_0$ by

$$L_x = L_0 - \Delta L \tag{5.5}$$

And

$$\Delta L = \varepsilon_x L_0 = -\nu\varepsilon_z L_0 \tag{5.6}$$

The area of the block open for fluid transport cane be related to $\varepsilon_z$ by substituting (5.5) into (5.6) and recognising that $L_y = L_0$ for the block.

$$A_B = L_y L_x = \left( \frac{L_0(1-\nu\varepsilon_z)}{2} \right) \tag{5.7}$$

The result in (5.7) can be used to investigate the extent of which the porosity of a model can vary as function of length variation. From Section 3.1.1, Porosity is defined as

$$\phi = \frac{V_{liquid}}{V_{total}} \tag{5.8}$$

Using (5.8) and the expression for a volume of a cube, the relationship between porosity, length variation and poisons ratio for this particular geometry can be found.

$$\begin{gathered} \phi = \frac{dA \cdot L_0}{{L_0}^3} = \frac{{L_0}^2 L_x}{{L_0}^3} = \frac{{L_0}^3(1-\nu\varepsilon_{zz})}{2 \cdot {L_0}^3} \\ \phi = \frac{(1-\nu\varepsilon_{zz})}{2} \end{gathered} \tag{5.9}$$

Another area of interest is the cross-section taken at the interface between two blocks in a geometry (Section 2, Figure 5-3). Figure 5-4a provides an isometric view to highlight the orientation of Block i and Block i+1 relative to each other. Figure 5-4b provides a schematic cross section of the geometry at the interface where white represents solid, blue represents area open to fluid flow (void space). In the un-varied state where $L_x$ and $L_y$ are equal to $L_0$, the cross-sectional area open for fluid transport at the interface is half the cross-sectional area found in the block (5.7). From the conservation of mass, it can be expected that as the area of the geometry contracts and expands along the fluid path that the simulated fluid will accelerate and decelerate.

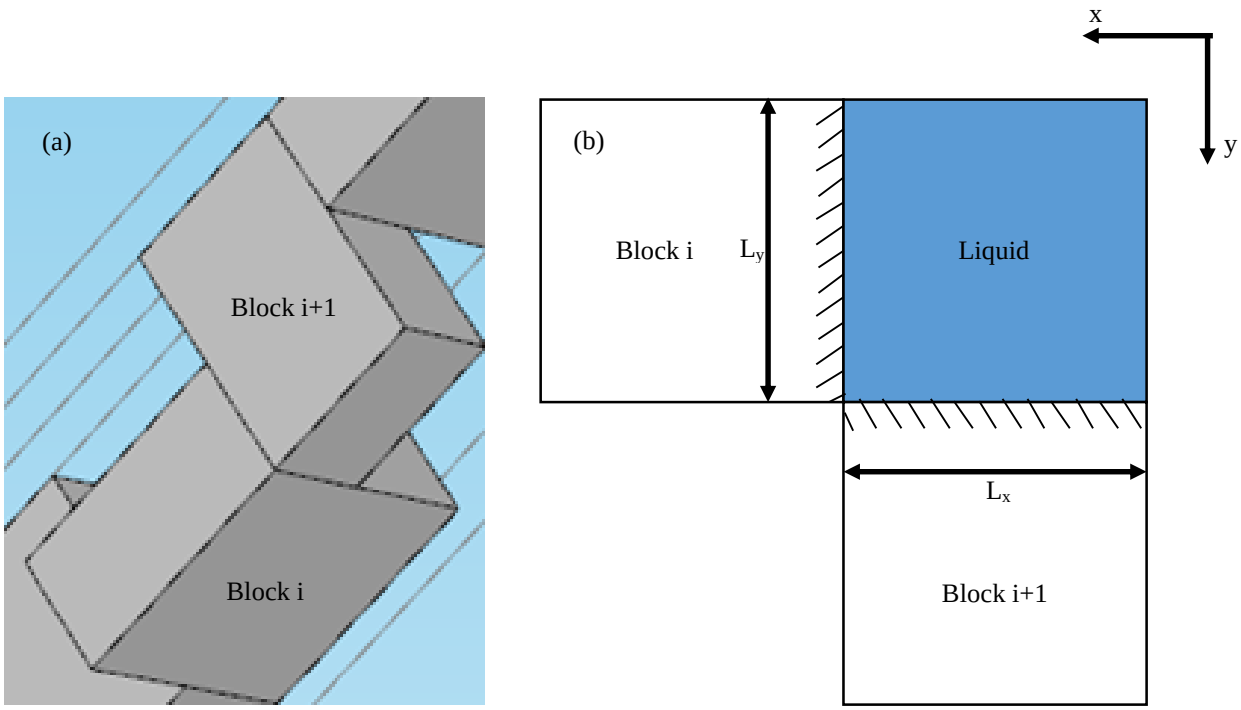


*Figure 5-4a-b.(a) Isometric perspective on the two blocks where the transition in length variation occurs. (b) Schematic cross-section from Figure 5-3 for area normal to fluid flow at the transition between two 'blocks'*

Due to the symmetry boundary condition, the side length of the blocks in the model is half of $L_0$. For the case where Block 1 and Block 2 experience different length variations, $L_x$ and $L_y$ can be expressed by

$$L_x^{i+1} = \frac{L_0 - \Delta L}{2} = \frac{L_0 + \nu\varepsilon_{i+1,z} L_0}{2} = \frac{L_0(1+\nu\varepsilon_{i+1,z})}{2}$$
$$L_y^{i} = \frac{L_0 - \Delta L}{2} = \frac{L_0 + \nu\varepsilon_{i,z} L_0}{2} = \frac{L_0(1+\nu\varepsilon_{i,z})}{2} \quad (5.10)$$

However, the area normal to fluid flow is the geometrical feature of interest. As $L_x$ and $L_y$ for the solid increase due to length variation, the area exposed to fluid flow decreases. In other words $\Delta\varepsilon_x = \Delta\varepsilon_y = \nu\Delta\varepsilon_z$.

# 6 Curve Fitting Methods

*A key goal of the study is to produce empirical relationships from simulation data. When developing these relationships, consideration must be given to the chosen method that allows for rapid and simple development of equations that can accurately predict local pressure and permeability for a given geometry. The basis of the local pressure prediction is the stepwise function developed in Section 6.1. Two methods were considered that can create predictive models from simulation data known as Method of Least Squares (Section 6.2) and Taylor Expansion (Section 6.3). The relationships between geometry and permeability in experimental data were found to be either approximately linear or quadratic in nature, and the two methods have been developed with this in mind.*

## 6.1 Finite Difference Methods

To construct a simplified stepwise function to predict the local pressure in a geometry, a first order, one-dimensional finite difference equation is constructed to provide a means to calculate local pressure drop in a geometry. The local pressure found is for steady-state conditions, so transient effects are discounted. The finite difference method is built on the constraint that

$$\frac{\Delta f}{\Delta z} \approx \frac{df}{dz} \tag{6.1}$$

Where $f$ is an arbitrary function and $\Delta z$ is the step size along the z-axis. For (6.1) to hold, the step size ($\Delta z$) must be sufficiently small to allow prediction of the pressure drop over a block. For this particular application, the finite difference method is used to integrate the block's hindrance to fluid flow over the length of the block. From the integration the pressure drop that drives the fluid through the flow path can be determined. Approximation of derivatives used in the integration is conducted by the use of a backwards looking Taylor series.

$$f(x_{i+1}) = f(x_i) + hf^{(1)}(x_i) + \frac{h^2}{2!} f^{(2)}(x_i) + \frac{h^3}{3!} f^{(3)}(x_i) + \ldots \tag{6.2}$$

Where $h = x_{i+1} - x_i$. For this application $x_{i+1} - x_i$ is taken to be the length of the block used in the geometry (Section 4.2.1). The superscripts indicate the order of the derivative. To maintain a first order derivative, the Taylor series function is truncated after the second term. After rearrangement, the Taylor series then takes the form.

$$f^{(1)}(x_i) = \frac{f(x_i) - f(x_{i-1})}{h} \tag{6.3}$$

Using sigma notation, the approximations of local pressure can be propagated through a geometry. A backwards looking Taylor series can use a known inlet pressure to approximate the local pressure along the length of the geometry. The differential across a block can be approximated by rearranging Darcy's law. A major limitation in using (6.3) is that the step size $(h)$ is constant. Geometries that require a variable step size in response to changes in geometry along the path of fluid flow cannot use (6.3) as a finite difference method. A variable step size is required to find local pressure at desired points when length variation causes the length of the block to change, affecting permeability. In this case, the step size from one pressure value to the next would change, making (6.3) no longer suitable.

## 6.2 Method of Least Squares

Originally developed as a method to determine the orbit of planetary bodies [33], the method of least squares allows the determination of a best-fit line for data. Analysis of the method shows that it is capable of providing a best fit for any linear combination of functions [34] as long as it has the general form shown in (6.4).

$$y = a_1 f_1(x) + \ldots + a_n f_n(x) \tag{6.4}$$

It so happens for the simulation data used in this study, only linear and polynomial functions to the *k*th degree need to be generated using linear regression. This being the case, Equation (6.4) can be expressed as (6.5)

$$y = a_0 + a_1 x + \ldots + a_k x^k \tag{6.5}$$

Given the approximate solution from the RHS compared to the exact LHS solution in (6.5) the residual is stated in (6.6)

$$R^2 = \sum_{i=1}^{n} [y_i - (a_0 + a_1 x + \ldots + a_k x_i^k)]^2 = 0 \tag{6.6}$$

The goal is to have our residual (*R*) reduce to zero, i.e. the approximated solution exactly matches the exact solution. Another way to express this condition is to have R not vary with respect to the coefficients ($a_0, a_1, \ldots, a_k$). This condition is expressed below (6.7)

$$\frac{\partial R}{\partial a_0} = 0, \frac{\partial R}{\partial a_1} = 0, \ldots, \frac{\partial R}{\partial a_k} = 0 \tag{6.7}$$

If the partial derivative of (6.6) for each coefficient is taken, a system of equations is developed (6.8)

$$\begin{aligned}
\frac{\partial(R^2)}{\partial a_0} &= -2\sum_{i=1}^{n}[y-(a_0+a_1x_i+\ldots+a_kx^k)]=0\\
\frac{\partial(R^2)}{\partial a_1} &= -2\sum_{i=1}^{n}[y-(a_0+a_1x_i+\ldots+a_kx^k)]x=0\\
\frac{\partial(R^2)}{\partial a_k} &= -2\sum_{i=1}^{n}[y-(a_0+a_1x_i+\ldots+a_kx^k)]x^k=0
\end{aligned} \tag{6.8}$$

The equations in (6.8) then lead to the algebraic equations shown (6.9).

$$\begin{aligned}
a_0n+a_1\sum_{i=1}^{n}x_i+\ldots+a_k\sum_{i=1}^{n}x_i^k &= \sum_{i=1}^{n}y_i\\
a_0\sum_{i=1}^{n}x_i+a_1\sum_{i=1}^{n}x_i^2+\ldots+a_k\sum_{i=1}^{n}x_i^{k+1} &= \sum_{i=1}^{n}x_iy_i\\
a_0\sum_{i=1}^{n}x_i^k+a_1\sum_{i=1}^{n}x_i^{k+1}+\ldots+a_k\sum_{i=1}^{n}x_i^{2k} &= \sum_{i=1}^{n}x_i^ky_i
\end{aligned} \tag{6.9}$$

Or in matrix form.

$$\begin{bmatrix} n & \sum_{i=1}^{n}x_i & \cdots & \sum_{i=1}^{n}x_i^k \\ \sum_{i=1}^{n}x_i & \sum_{i=1}^{n}x_i^2 & \cdots & \sum_{i=1}^{n}x_i^{k+1} \\ \vdots & \vdots & \ddots & \vdots \\ \sum_{i=1}^{n}x_i^k & \sum_{i=1}^{n}x_i^{k+1} & \cdots & \sum_{i=1}^{n}x_i^{2k} \end{bmatrix}\begin{bmatrix} a_0 \\ a_1 \\ \vdots \\ a_2 \end{bmatrix}=\begin{bmatrix} \sum_{i=1}^{n}y_i \\ \sum_{i=1}^{n}x_iy_i \\ \vdots \\ \sum_{i=1}^{n}x_i^ky_i \end{bmatrix} \tag{6.10}$$

This matrix is a Van der Monde matrix, and given $n$ points $(x_i,y_i)$ and fitting with the coefficients $(a_0,\ldots,a_k)$ gives

$$\begin{bmatrix} y_1 \\ y_2 \\ \vdots \\ y_n \end{bmatrix}=\begin{bmatrix} 1 & x_1 & x_1^2 & \cdots & x_1^k \\ 1 & x_2 & x_2^2 & \cdots & x_2^k \\ \vdots & \vdots & \vdots & \ddots & \vdots \\ 1 & x_n & x_n^2 & \cdots & x_n^k \end{bmatrix}\begin{bmatrix} a_0 \\ a_1 \\ \vdots \\ a_k \end{bmatrix} \tag{6.11}$$

In matrix notation, the notation for a polynomial fit is given by

$$\mathbf{y}=\mathbf{Xa} \tag{6.12}$$

Equation (6.12) can be solved by multiplying both sides by the transpose $X^T$ and then solved numerically to yield the coefficient vector **a**. This provides the coefficients needed to build the predictive model from experimental data.

## 6.3 Taylor Series Approximation

The second method of choice is the use of a multi-variable Taylor series approximation to generate an equation to approximate the behaviour of permeability as a function of the length variation and any change in length variation between blocks in the geometric model. The function is developed by using assumptions and approximations to allow the general Taylor series form to be reduced. The general form of a second-order Taylor polynomial is shown below (6.13)

$$f(x,y) = f(x_0,y_0) + \left.\frac{\partial f}{\partial x}\right|_{x_0,y_0}(x-x_0) + \left.\frac{\partial f}{\partial y}\right|_{x_0,y_0}(y-y_0) + \frac{1}{2!}\left[\left.\frac{\partial^2 f}{\partial x^2}\right|_{x_0,y_0}(x-x_0)^2 + \left.\frac{\partial^2 f}{\partial y^2}\right|_{x_0,y_0}(y-y_0)^2 + 2\left.\frac{\partial^2 f}{\partial x \partial y}\right|_{x_0,y_0}(x-x_0)(y-y_0)\right] + O(x^3,y^3) \quad (6.13)$$

Rewriting (6.13) for the case presented in this thesis regarding the permeability of a complex geometry as a function of the length variation and change in length variation gives (6.14)

$$\Delta K(\varepsilon,\Delta\varepsilon) = \Delta K(\varepsilon_0,\Delta\varepsilon_0) + \left.\frac{\partial \Delta K}{\partial \varepsilon}\right|_{\varepsilon_0,\varepsilon_0}(\varepsilon-\varepsilon_0) + \left.\frac{\partial \Delta K}{\partial \Delta\varepsilon}\right|_{\varepsilon_0,\varepsilon_0}(\Delta\varepsilon-\Delta\varepsilon_0) + \frac{1}{2!}\left[\left.\frac{\partial^2 \Delta K}{\partial \varepsilon^2}\right|_{\varepsilon_0,\varepsilon_0}(\varepsilon-\varepsilon_0)^2 + \left.\frac{\partial^2 \Delta K}{\partial \Delta\varepsilon^2}\right|_{\varepsilon_0,\varepsilon_0}(\Delta\varepsilon-\Delta\varepsilon_0)^2 + 2\left.\frac{\partial^2 \Delta K}{\partial \varepsilon \partial \Delta\varepsilon}\right|_{\varepsilon_0,\varepsilon_0}(\varepsilon-\varepsilon_0)(\Delta\varepsilon-\Delta\varepsilon_0)\right] + O(\varepsilon^3,\Delta\varepsilon^3) \quad (6.14)$$

Where $\Delta K$ is the change in permeability due to a change in length variation, $\varepsilon$ is the current length variation and $\Delta\varepsilon$ is the change in length variation ratio. To reduce(6.14) to (6.15), it is assumed that $\Delta K$ is linearly related to $\varepsilon$ and $\Delta\varepsilon$ so that $\frac{\partial \Delta K}{\partial \varepsilon} = f(\varepsilon), \frac{\partial \Delta K}{\partial \Delta\varepsilon} = f(\Delta\varepsilon)$ and $\frac{\partial^2 \Delta K}{\partial \varepsilon^2} = 0, \frac{\partial^2 \Delta K}{\partial \Delta\varepsilon^2} = 0$. These assumptions are justified in Section 9.2. $\varepsilon_0$ and $\Delta\varepsilon_0$ are also taken to be $\varepsilon_0 = 0$ and $\Delta\varepsilon_0 = 0$ . The Taylor series approximation operates around these values.

$$\Delta K(\varepsilon,\Delta\varepsilon) = \Delta K(0,0) + \left.\frac{\partial \Delta K}{\partial \varepsilon}\right|_{0,0}(\varepsilon) + \left.\frac{\partial \Delta K}{\partial \Delta\varepsilon}\right|_{0,0}(\Delta\varepsilon) + \left.\frac{\partial^2 \Delta K}{\partial \varepsilon \partial \Delta\varepsilon}\right|_{0,0}(\varepsilon)(\Delta\varepsilon) + O(\varepsilon^3,\Delta\varepsilon^3) \quad (6.15)$$

Assuming linear gradients, the differential terms in (6.15) can be approximated by taking simulation data for permeability given several different combinations of length variation and length variation change. The values are chosen as they represent the specified range of applicability for the model.

$$\begin{aligned}&\Delta K(\varepsilon=0,\Delta\varepsilon=0)\\&\Delta K(\varepsilon=0,\Delta\varepsilon=-0.5)\\&\Delta K(\varepsilon=0.5,\Delta\varepsilon=0)\\&\Delta K(\varepsilon=0.5,\Delta\varepsilon=0.5)\end{aligned} \tag{6.16}$$

$\Delta K$ is defined in (6.17) where $K_{SL}$ is the simulated local permeability for the geometry.

$$\Delta K = K_L^S(\varepsilon,\Delta\varepsilon) - K_L^S(\varepsilon,\Delta\varepsilon=0) \tag{6.17}$$

Using the values from (6.16) the differential terms can be approximated as shown in (6.18)

$$\begin{aligned}\left.\frac{\partial\Delta K}{\partial\varepsilon}\right|_{0,0} &\approx \frac{\Delta K(\varepsilon=0,\Delta\varepsilon=0)-\Delta K(\varepsilon=0.5,\Delta\varepsilon=0)}{(\varepsilon=0)-(\varepsilon=0.5)}\\ \left.\frac{\partial\Delta K}{\partial\Delta\varepsilon}\right|_{0,0} &\approx \frac{\Delta K(\varepsilon=0,\Delta\varepsilon=0)-\Delta K(\varepsilon=0,\Delta\varepsilon=0.5)}{(\Delta\varepsilon=0)-(\Delta\varepsilon=0.5)}\\ \left.\frac{\partial^2\Delta K}{\partial\varepsilon\partial\Delta\varepsilon}\right|_{0,0} &= \frac{\partial}{\partial\varepsilon}\left(\frac{\partial\Delta K}{\partial\Delta\varepsilon}\right) \approx \frac{\left.\left(\frac{\partial\Delta K}{\partial\Delta\varepsilon}\right)\right|_{\varepsilon=0,\Delta\varepsilon=0} - \left.\left(\frac{\partial\Delta K}{\partial\Delta\varepsilon}\right)\right|_{\varepsilon=0.5,\Delta\varepsilon=0}}{(\varepsilon=0)-(\varepsilon=0.5)}\end{aligned} \tag{6.18}$$

where

$$\begin{aligned}\left.\left(\frac{\partial\Delta K}{\partial\Delta\varepsilon}\right)\right|_{\varepsilon=0,\Delta\varepsilon=0} &\approx \frac{\Delta K(\varepsilon=0,\Delta\varepsilon=0)-\Delta K(\varepsilon=0,\Delta\varepsilon=-0.5)}{(\Delta\varepsilon=0)-(\Delta\varepsilon=-0.5)}\\ \left.\left(\frac{\partial\Delta K}{\partial\Delta\varepsilon}\right)\right|_{\varepsilon=0.5,\Delta\varepsilon=0} &\approx \frac{\Delta K(\varepsilon=0.5,\Delta\varepsilon=0)-\Delta K(\varepsilon=0.5,\Delta\varepsilon=0.5)}{(\Delta\varepsilon=0)-(\Delta\varepsilon=0.5)}\end{aligned}$$

The Taylor series approximation can now be represented as a function that relates the two variables to permeability. Once the function has been determined for a particular geometry, it can be used to predict the change in permeability due to a change in length variation within the geometry.

$$\Delta K(\varepsilon,\Delta\varepsilon) = C_1\varepsilon + C_2\Delta\varepsilon + C_3\Delta\varepsilon\cdot\varepsilon \tag{6.19}$$

The Taylor series method only requires two additional simulations beyond what is required to determine the relationship between $K$ and ε (Sections 9-10). There is also the additional variation on the method where the simulated global permeability $\left(K_G^S\right)$ is used instead of the simulated local permeability $\left(K_L^S\right)$ to determine $\Delta K$ in (6.17).

# 7 Method

*The following section provides a description of the method used to setup the COMSOL model for simulations and develop the data to produce meaningful results. The three steps of Pre-processing (Section 7.27.6) solving (Sections 7.77.9), and post-processing (Section 7.10) was described. Some points of note from the method is that an unstructured mesh is used to provide a numerical solution (Section 7.6) and that Section 7.9 describes the locations in the simulation that the raw data was extracted from to calculate simulated values for permeability.*

## 7.1 Solution Process

Solving a fluid flow problem using computation fluid dynamics (CFD) comprises of three main steps which are referred to as:

- Pre-Processing
- Solving
- Post-Processing

The Pre-processing stage allows for initialisation and set-up of solution parameters as well as the specification of the mesh, boundary conditions, initial conditions and desired governing numerical equations that are used to solve the desired problem. These topics as they relate to this thesis are discussed in Sections 7.27.6. Once the initialisation has been completed, the iterative solver uses the initial conditions and boundary conditions to iteratively solve the flow study. Once the solution has converged (Section 7.8), the flow characteristics are output. The volumetric flow rate of the fluid and the local pressure of the fluid are the flow characteristics which are of interest here. Once the solution has converged, post-processing is conducted. For this study, post-processing consists of using the output data to calculate simulated values for permeability, volumetric flow rate and local pressure. The data presented in Sections 9 and 10 is post-processed in Excel and then exported to MATLAB to construct figures.

## 7.2 Problem formulation

The simulation was conducted on COMSOL™ 4.3 using an Intel® Quad Core™ i7-2600 CPU @ 3.40 GHz. The CPU uses 32 GB of RAM. The post processing of data was conducted using MATLAB 2013a and EXCEL 2013.The calculation methodology used is based on fundamental CFD equations that model fluid flow using COMSOL. These CFD equations are discretized by finite element methods and converted into a set of non-linear algebraic equations. The algebraic equations are then linearised and solved algebraically.

The COMSOL™ model used Creeping Flow (also known as Stokes Flow) which makes the assumption that the flow is completely independent of inertial effects and ignores inertial contributions to the solution. The use of the creeping flow was validated via comparison to results produced by the COMSOL™ laminar flow model. In the simulation, the equation was stationary and neglected transient effects. Fluid properties were based on selected parameters to encourage low Reynolds numbers, and are shown in Table 7-1. These fluid and geometric properties are used in all simulations unless otherwise specified.

*Table 7-1. Fluid properties for flow through studied geometries*

| Controlled Parameter | Symbol | Value | Unit |
|---|---|---|---|
| Dynamic Viscosity | $\mu$ | 0.1 | $kg \cdot m^{-1} \cdot s^{-1}$ |
| Density | $\rho$ | 1000 | $kg \cdot m^{-3}$ |
| Pressure Drop | $\Delta P$ | 1000 | $Pa$ |
| Variation Ratio | $\nu$ | 0.4 | - |

The fluid properties listed are approximately similar to the fluid properties for a water-glycerol mixture. The pressure drop was maintained at 1000 Pa across all studies conducted here.

## 7.3 Domain

The domain of the study is based on the geometry developed in Section 4, with the final geometry used described in Chapter 5. Therefore the domain for simulations conducted using COMSOL™ is a 3 dimensional domain. A 3D domain is used to provide the most accurate solution possible, but requires more computational resources that a simulation conducted using a two dimensional domain. However the geometry presented here does not reduce well to a two dimensional domain as the geometry varies along in the x, y and z axes.

## 7.4 Initial Conditions

The model was initialised with a linear pressure gradient along the z-axis as a means to reduce the computational time required for the numerical solver to converge by approximating the final solution. To construct the initial conditions, the following equation was provided to COMSOL™.

$$P(z) = P_{inlet} - \frac{\Delta P}{L_t} \cdot z \tag{7.1}$$

Where $P(z)$ is the local pressure in the geometry as a function of the distance along the z-axis, $P_{inlet}$ is the specified pressure at the inlet, in this case 1000 Pa, $\Delta P$ is the total pressure drop across the geometry, $L_t$ is the total length of the geometry along the z-axis, and z is the location on the z-axis.

## 7.5 Boundary Conditions

As part of the model and geometry initialisation, boundary conditions are required for the solver to generate a solution. They also assist in developing flow field behaviour as a means to represent the larger system with the reduced simulation model. The simulation geometry is shown in Figure 7-1.

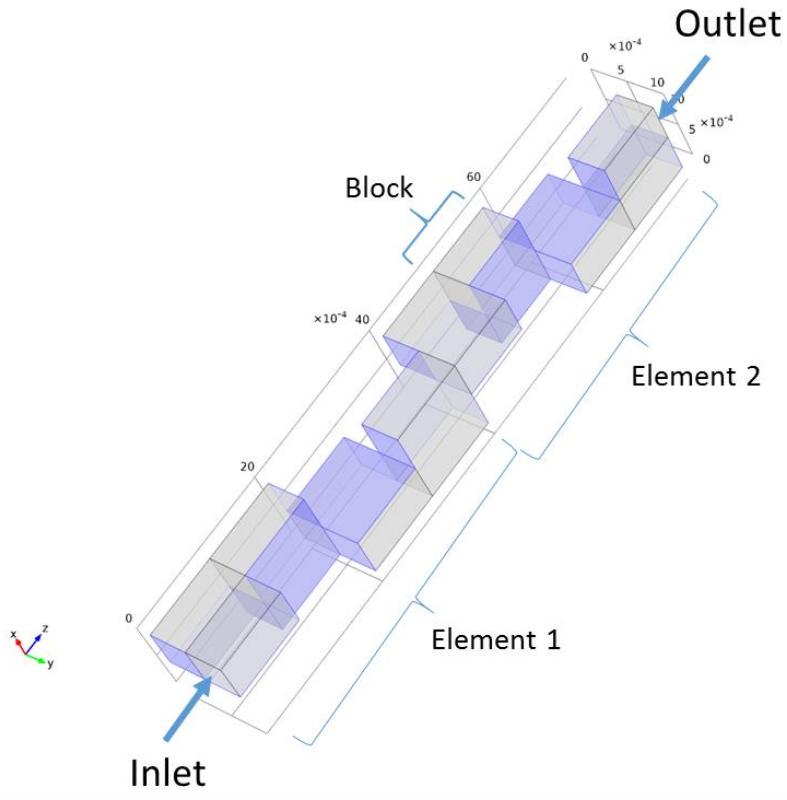


*Figure 7-1. Simulation geometry with inlet and outlet boundary conditions labelled, surfaces with symmetry boundary conditions in white and surfaces with wall boundary conditions in blue*

Each boundary conditions is described in Sections 7.5.1-7.5.3 below. The description includes their mathematical representation and the process with using them in COMSOL.

### 7.5.1 Wall Boundary Condition

The wall boundary condition was used on the inwards facing surfaces of the geometry as a means to represent the contact area between the fluid and solid phase. Previous literature states that at this scale fluid interaction with solid

surfaces can still be predicted by classical Navier-Stokes equations with along with a no-slip boundary condition [25]. Therefore, a no-slip boundary condition was used for geometries here and can be represented by $\mathbf{V} = 0$ i.e. there is no fluid motion at the wall.

### 7.5.2 Symmetry Boundary Condition

The symmetry boundary condition is applied to the outwards facings surfaces in the geometry. In this case the boundary condition does not allow fluid penetration through the surface and shear stresses vanish at the surface. It has effect of effectively mirroring the flow field along the surface which acts as the plane of symmetry. It is useful here as a boundary condition as it allows for reduction of the domain, improving solution time while not impacting flow behaviour. It is composed of a Dirichlet condition (7.2) and a Neumann condition (7.3)

$$\mathbf{V} \cdot \mathbf{n} = 0 \tag{7.2}$$

where $\mathbf{V}$ is the velocity vector and $\mathbf{n}$ is the normal.

$$(-P\mathbf{I} + \mu(\nabla\mathbf{V} + (\nabla\mathbf{V})^{\mathrm{T}}))\mathbf{n} = 0 \tag{7.3}$$

where $P$ is pressure, $\mathbf{I}$ is the pressure vector, $\mathbf{V}$ is the velocity vector and $\mathbf{n}$ is the normal.

### 7.5.3 Inlet/Outlet

The inlet boundary condition specifies the surface that fluid enters the domain from. The outlet boundary condition specifies where it leaves the domain. For this study, it is important to control the pressure drop across the geometry to maintain flow in the Darcy regime and be able to easily determine how permeability relates to a pressure drop. This being the case, the inlet and outlet boundary conditions are used such that a constant pressure drop $(\Delta P)$ of 1000 Pa is maintained across the geometry no matter the length of the geometry. The pressure drop is initialised by setting up the inlet to have a local pressure of 1000 Pa and the outlet pressure to be 0 Pa. The inlet is set up in the geometry by specifying a pressure and setting viscous stress equal to zero. This can be mathematically represented by applying the following equations to the inlet surface specified in Figure 7-1.

$$P = P_{inlet} = 1000Pa \tag{7.4}$$

$$\left[\mu(\nabla\mathbf{V} + (\nabla\mathbf{V})^{T})\right]\mathbf{n} = 0 \tag{7.5}$$

Here $P$ is the pressure at the surface and $P_{inlet}$ is the predetermined inlet pressure of 1000 Pa. To initialise the outlet boundary condition the equations (7.4) and (7.5) are used again except this time $P = P_{outlet} = 0Pa$. The outlet boundary condition is applied to the surface specified in Figure 7-1.

## 7.6 Mesh Generation

To solve the flow physics in response to the conditions specified requires discretizing the domain into smaller, non-overlapping subdomains. This process is known as 'mesh generation'. Each of the subdomains is referred to as an 'element'. During mesh generation, care must be taken that the elements are well-formed and that no gaps are present between the elements so that the discrete solutions for each element can be stitched together to provide an overall representation of the simulated flow through the domain.

Two main options for mesh generation exist with the use of COMSOL, namely 'structured' and 'unstructured meshes'. A combination of the two can also be used depending on the requirements of the geometry. The both have associated advantages and disadvantages. Here an unstructured mesh was used in an effort to represent the fluid flow around the interior corners accurately. The full list of the advantages and disadvantages of each mesh category is listed in Table 7-2. Based on the simple-set up, and the need to accurately model the constantly changing flow field, unstructured meshes were used in this study. It was thought that any reduction in computation time that a structured mesh provides would be outweighed by the amount of time required to construct it for the many geometrical permutations tested in Sections 9 and 10.

*Table 7-2. Advantages and disadvantages of structured and unstructured meshes*

| | Advantage | Disadvantage |
|---|---|---|
| Structured Mesh | Computationally Efficient<br>Use less RAM | Difficult to set-up |
| Unstructured Mesh | Simple set-up<br>Better flexibility for complex geometries<br>More accurate results | Lack of user control<br>Require more RAM |

With the desired mesh chosen, continued work needs to be completed into determining the ideal mesh for the domain. This includes investigation into the optimum element size that balances an acceptable level of accuracy with reasonable solution times. To this end, a mesh refinement study is conducted, the full details of which are outlined in Section 8. The study seeks to prove that the solution converges, and also determines what the optimum mesh element size is that balances solution time and solution accuracy. How convergence is tested, and the requirements for convergence is discussed in Section 7.8.

For a geometry, the mesh generation algorithms in COMSOL allow for several different kinds of corner settings. Corner settings allow a COMSOL user set various corner treatments which are different methods of wrapping mesh elements around sharp-edged corners in a way that represents the geometry as accurately as possible. The treatments include:

- Trimming
- Splitting
- None

During the pre-processing for this study, trimming was set as the chosen option to trim the boundary layer mesh at the 90° corners. Splitting was unable to cope with the corners introduced in the developed geometry, so trimming was used instead.

## 7.7 Parametric Studies

To streamline the output of raw data, and reduce the initialisation time, the simulations were often set up as a system of parametric studies, where a single parameter such as the length variation $(\varepsilon)$ or the pore length $(L_0)$ is altered for a given geometry while all other parameters are held constant. A parametric study was initialised in COMSOL by initialising a row vector containing a range of values for a specified parameter as shown in (7.6)

$$\bar{\varepsilon} = (0, 0.1, 0.2, 0.3, 0.4, 0.5) \tag{7.6}$$

The COMSOL model now solves the geometry six times, which the length variation changing each time, until the solution for each value specified has been determined. The solution data for each length variation is stored and then exported as a table to be input into Excel for post-processing.

## 7.8 Convergence

To verify that COMSOL was producing accurate and converged solutions for the given inputs, a series of convergence studies were chosen that investigate the behaviour of the outputted solution in response to parameters controlling mesh size. The accuracy for the use of the creeping flow model compared to the laminar flow model was compared as well as a simple validation case where the local pressure values could be calculated analytically. If the errors and discrepancies between cases are at an acceptable level, it can be said that the solution is converged. Due to the nature of this study and the end goal of creating a predictive model it is very important that the simulations are accurate as possible to generate a model that does accurately represent the flow behaviour. Therefore, an entire Chapter 8 is devoted to the investigation of convergence.

## 7.9 Raw Data Extraction

Once a simulation had been initialised and the solver converged to a solution, data needed to be extracted from the model to understand the flow through geometry. For this study, the local pressure and the volumetric flow rate was extract from the solved flow field at specified points along the geometry for each model. An example model is presented in Figure 7-2. Here a colour gradient is used to illustrate the pressure drop along the model in the direction of bulk fluid transport.

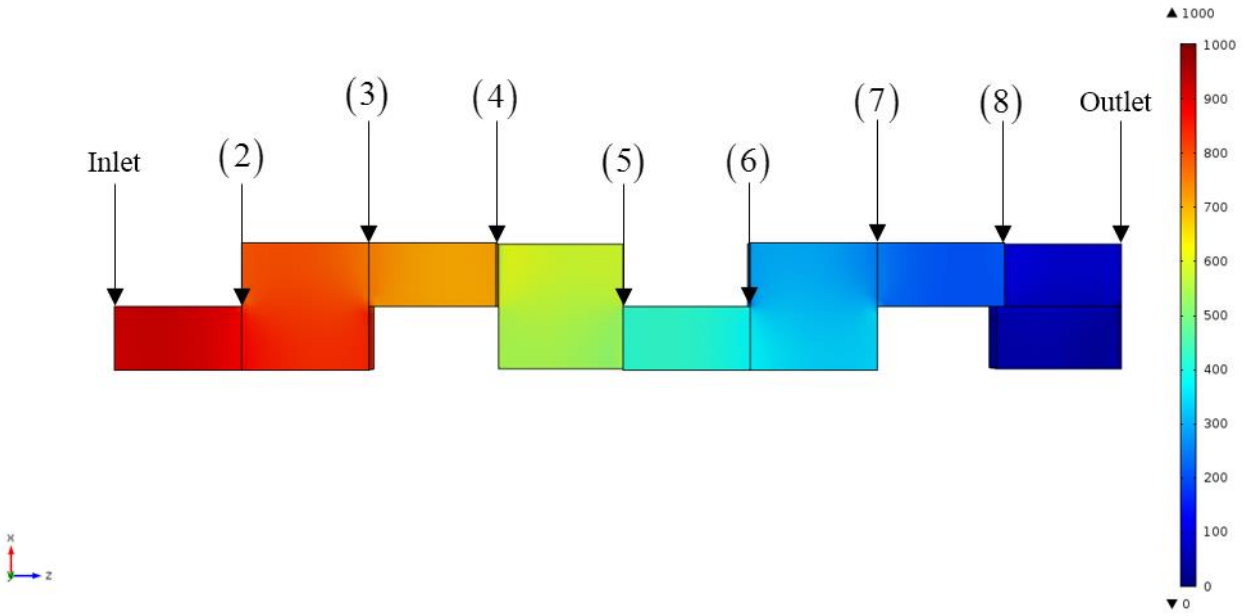


*Figure 7-2. Geometric Model depicting pressure drop across the length in Pascals. Arrows are used to identify the interfaces where local pressure and flow rate data is extracted.*

The flow data in all simulations was extracted from measurements at the interface between the blocks in the geometry. Additional values of flow data was also found for the outlet and inlet of the geometry. The inlet and outlet are labelled, and the interior interfaces are labelled in ascending order in the positive direction along the z axis. The pressure data presented in Sections 9 and 10 as well as Appendices A and B is taken from one of the interfaces. The subscript on the pressure symbol denotes which interface the pressure value was measured at. The volumetric flow rate was always measured at the most central interface in the geometry, dependent on how many elements are present.

The pressure value was measured by taking a 'surface average' value for pressure across the interface. Firstly, a 'derived value' node was set up in COMSOL™, and then the interface was manually selected and placed into the relevant field on the GUI. The expression was set to 'p' which is how COMSOL™ denotes pressure in a flow field. Finally the function was evaluated and placed in a table that contained the average surface pressures from other interfaces in the same geometry. This was then exported to Excel™ for further processing. The volumetric flow rate was determined in a similar manner except that a 'surface integration' was conducted across the chosen interface

instead of a ‘surface average’ function. For the volumetric flow rate, the expression for integration was set as ‘w’, which is how COMSOL™ denotes z-component of the velocity direction (the direction of bulk fluid transport for this geometry). ‘w’ is then integrated over the surface area to provide a simulated value of volumetric flow rate.

## 7.10 Post-processing

Once the solutions had been generated using COMSOLs solver, the data is saved as a .txt file and logged in file storage with the input conditions, geometry length variation and any other relevant information noted. The stored data is then exported to Microsoft Excel for data manipulation, curve fitting and visualisation. Excel was chosen as it allows for easily manipulation of large amounts of segmented data that is input in multiple tables. The data and relationships can be visualised easily and allowed for the curve fitting models to be quickly altered to determine what generates the best fit for many different simulations. Finally, the data to be used to generate figures is also exported to MATLAB which is used to plot the data shown in this thesis.

When data is exported to Excel, it is placed into a table containing raw data and the relevant fluid and geometrical properties. The data is processed to determine the local and global permeability of the geometry for a given controlling parameter such as the length variation $(\varepsilon)$ or pore size $(L_0)$. The processed data is then plotted against the desired controlling variables. Next, the method of least squares as discussed in section 6 is used to create a model that relates that permeability values to the controlling parameters. From the resulting model, inferences can be made about how the permeability changes as a function of the controlling variable. The process is then repeated for many different geometries to establish whether the model is applicable to different geometries and its behaviour under different conditions. Finally, the key figures exhibiting the trends discovered are shown as exemplars in Section 9 and 10. Additional plots, case studies as well as some of the raw and processed data can be found in in Appendices A and B.

# 8 Refinement Studies

*Several refinement studies were conducted to confirm convergence for the model and to determine that the flow operates within the Darcy regime. One refinement study was conducted under creeping flow physics (Section 8.1.1) and the other was conducted under Laminar flow physics (Section 8.1.2). Both fluid physics were shown to provide solutions that converged as the mesh is refined. They also both experienced identical convergence behaviour suggesting that the convergence is independent of flow physics and that inertial effects are insignificant for the cases studied here. Crucially this confirms that the flow is within the Darcy regime and the models developed in this thesis are valid. It was also noted that there are apparent entrance and exit effects near the inlet and outlet of the geometry that are independent of the flow physics used.*

## 8.1 Model Convergence

To check the validity of the model, convergence studies for both creeping and laminar flow physics are conducted. The geometry is a 2 element construction similar to the one found in Figure 7-2. The length variation $(\varepsilon)$ is set to zero and the interfaces are equally spaced along the total length of the geometry. The fluid properties and flow conditions, boundary conditions and initial conditions are all identical to what is described in Section 7. The refinement studies were conducted by reducing the element size and increasing the number of elements in the matrix. The increase in elements for the specified domain increased the Degrees of Freedom that required solving to generate the solution. For the refinement study, the Degrees of Freedom solved are presented alongside the average pressure across each interface in the geometry calculated for a given mesh element size. A large number of solved Degrees of Freedom indicates a more refined mesh. The mesh element size was controlled by altering COMSOLs pre-set mesh parameters. Each one describe the quality of the mesh used to provide the numerical solution to the domain and are denoted as follows along with a shorthand form.

- Extremely Coarse $(ExC)$
- Extra Coarse $(EC)$
- Coarser $(Cr)$
- Coarse $(C)$
- Normal $(N)$
- Fine $(F)$

COMSOL™s pre-set parameters were used as they are already optimized for fluid physics and are likely to provide a suitable mesh that can adequately converge for any given problem in this study. Unlike some other studies, the Reynolds number for the flow here is to be maintained at very low values $(\mathrm{Re} < 1)$ . This being the case, the flow is expected to be very laminar and well behaved and complications such as turbulence or other forms of flow separation are not expected to make a significant impact. Therefore, it is unlikely that more attention needs to be made to the mesh generation parameters to suit the specific case here, as the flow studied here is benign.

The criteria for convergence is that the difference between successive iterations does not exceed 0.5 Pa. An absolute value for convergence is used over a relative value as it is independent of the pressure at the interface. This is especially important for interfaces near the outlet as the pressures here can be at or near zero. This being the case a small change in interface pressure as the mesh refines could be overrepresented when a 0.5 Pa criteria for a near zero interface pressure creates a very large relative error. In addition, for the simulations conducted here, the pressure values as determined by the numerical solver are compared to simplified case where it is expected that there is constant pressure drop between each interface due to the homogeneous geometry.

### 8.1.1 Creeping Flow

The first refinement study conducted was conducted using Creeping Flow physics, where inertial effects are ignored. Table 8-1 displays the results of the refinement study. The average pressure across each interface is provided from the numerical solution as a result of the number of solved Degrees of Freedom. The inlet and outlet are labelled as such and the interior interfaces are labelled in accordance with Figure 7-2. The average pressure across each interface is provided six times, one for each step in the refinement study.

*Table 8-1.A refinement study measuring local pressure at interfaces in a 2 element geometry with creeping flow physics*

| Mesh Description | Degrees of Freedom | Interface (Pa) | | | | | | | | |
|---|---|---|---|---|---|---|---|---|---|---|
| | | Inlet | (2) | (3) | (4) | (5) | (6) | (7) | (8) | Outlet |
| Extremely Coarse | 3524 | 1000 | 880.55 | 747.81 | 615.15 | 494.50 | 371.59 | 246.35 | 119.96 | 0 |
| Extra Coarse | 8444 | 1000 | 876.76 | 751.59 | 625.40 | 500.72 | 373.73 | 251.48 | 122.20 | 0 |
| Coarser | 23788 | 1000 | 875.76 | 750.40 | 625.59 | 499.26 | 372.51 | 249.07 | 123.05 | 0 |
| Coarse | 46892 | 1000 | 876.58 | 750.85 | 625.43 | 499.98 | 374.17 | 250.48 | 123.90 | 0 |
| Normal | 139008 | 1000 | 876.44 | 751.11 | 626.39 | 500.08 | 374.29 | 249.18 | 123.42 | 0 |
| Fine | 278832 | 1000 | 876.33 | 750.78 | 625.97 | 499.91 | 373.99 | 249.26 | 123.41 | 0 |

The data in Table 8-1 provides several conclusions about the convergence of the model. Firstly, the pressure values converge and reduce within the specified requirements for convergence (0.5 Pa between iterations). Additionally, as expected, the inlet and the outlet are shown to maintain constant values no matter the mesh quality as these are pre-

defined as part of the boundary conditions in Section 7.5. The solution solved using a 'fine' mesh provides numerical solutions that correspond to the expected behaviour of approximately equal pressure drop between interfaces along the total length of the geometry. The required change in direction for the flow vector as the fluid moves through geometry did not appear to impact the results in any significant way. This behaviour is expected as a result of the research conducted in Section 3.3.1 which suggests at low Re, pressure loss around corners is expected to be negligible.

There appears to be a deviation for the converged value from the expected values of 875 Pa for interface (2) and 125 Pa for interface (8). It is likely that the error is a result of entrance and exit effects as discussed in Section 3.3.4. However the error is small enough (within 2 Pa) that this will be ignored.

To confirm the convergence of the interface pressure, the difference between solutions as the mesh is increasingly refined was taken. The results are shown in Table 8-2. Across all the interfaces, the difference in solutions are shown to become increasingly insignificant as the mesh is refined. A point of the note is that the difference in solutions as the mesh is refined oscillates between positive and negative values. However the absolute value for the difference in solution still decreases, so this is not thought to be a major issue.

*Table 8-2. Difference between the solutions for average pressure at each interface as the mesh is refined*

| Difference in Solution | Interface (Pa) | | | | | | | | |
|---|---|---|---|---|---|---|---|---|---|
| | Inlet | (2) | (3) | (4) | (5) | (6) | (7) | (8) | Outlet |
| $ExC \rightarrow EC$ | 0.00 | -3.79 | 3.78 | 10.25 | 6.22 | 2.14 | 5.13 | 2.24 | 0.00 |
| $EC \rightarrow Cr$ | 0.00 | -1.00 | -1.19 | 0.19 | -1.46 | -1.22 | -2.42 | 0.85 | 0.00 |
| $Cr \rightarrow C$ | 0.00 | 0.82 | 0.46 | -0.16 | 0.72 | 1.65 | 1.42 | 0.85 | 0.00 |
| $C \rightarrow N$ | 0.00 | -0.14 | 0.25 | 0.96 | 0.10 | 0.12 | -1.30 | -0.48 | 0.00 |
| $N \rightarrow F$ | 0.00 | -0.11 | -0.33 | -0.42 | -0.16 | -0.30 | 0.08 | -0.01 | 0.00 |

Based on the data presented, the conclusion can be made that the numerical solution converges with creeping flow physics used. Therefore, the constant porosity case study will use creeping flow to model the fluid flow through the geometry as it does not have to deal with expansions for contracts in the cross-sectional area and maintains a faster computation time to solve for a given geometry compared to laminar flow.

### 8.1.2 Laminar Flow

Another refinement study is conducted for laminar flow as a means to set a benchmark for creeping flow in terms of accuracy and reliability. In Section 8.2 the two are directly compared to determine whether inertial effects can be safely neglected. Table 8-3. A refinement study measuring local pressure at interfaces in a 2 element geometry with laminar flow physics displays the results of the refinement study. The average pressure across each interface is provided from the numerical solution as a result of the number of solved Degrees of Freedom. The inlet and outlet are

labelled as such and the interior interfaces are labelled in accordance with Figure 7-2. The average pressure across each interface is provided six times, one for each step in the refinement study.

*Table 8-3. A refinement study measuring local pressure at interfaces in a 2 element geometry with laminar flow physics*

| Mesh Description | Degrees of Freedom | Interface (Pa) | | | | | | | | |
|---|---|---|---|---|---|---|---|---|---|---|
| | | Inlet | (2) | (3) | (4) | (5) | (6) | (7) | (8) | Outlet |
| Extremely Coarse | 3524 | 1000 | 880.38 | 747.62 | 615.01 | 494.37 | 371.49 | 246.21 | 119.80 | 0 |
| Extra Coarse | 8444 | 1000 | 876.64 | 751.42 | 625.25 | 500.57 | 373.57 | 251.31 | 122.04 | 0 |
| Coarser | 23788 | 1000 | 875.63 | 750.28 | 625.47 | 499.13 | 372.40 | 248.96 | 122.94 | 0 |
| Coarse | 46892 | 1000 | 876.48 | 750.75 | 625.32 | 499.88 | 374.07 | 250.38 | 123.80 | 0 |
| Normal | 139008 | 1000 | 876.34 | 751.00 | 626.28 | 499.97 | 374.19 | 249.07 | 123.31 | 0 |
| Fine | 278832 | 1000 | 876.23 | 750.67 | 625.86 | 499.80 | 373.88 | 249.15 | 123.31 | 0 |

The convergence behaviour is identical to the creeping flow convergence behaviour exhibited in Table 8-1. Again a clear convergence behaviour is apparent with all the values reaching the criteria for convergence ( $< 0.5Pa$ between iterations) between the 'normal' and 'fine' mesh qualities. The Inlet and Outlet interfaces experience no change in their pressures as expected. In agreement with the creeping flow physics, Interface (2) and Interface (8) deviate slightly from the expected average pressure values when calculated using laminar flow physics. Therefore it can be concluded that the discrepancy between expected and simulated values is indeed a result of fluid flow phenomena namely entrance/exit effects over a limitation of using creeping flow physics. The difference in solutions for each iteration in the refinement study is again presented for the laminar flow model in Table 8-4.

*Table 8-4. Difference between the values of average pressure at each interface as the mesh is refined*

| Difference in Solution | Interface (Pa) | | | | | | | | |
|---|---|---|---|---|---|---|---|---|---|
| | Inlet | (2) | (3) | (4) | (5) | (6) | (7) | (8) | Outlet |
| $ExC \rightarrow EC$ | 0.00 | -3.74 | 3.80 | 10.24 | 6.20 | 2.08 | 5.10 | 2.24 | 0.00 |
| $EC \rightarrow Cr$ | 0.00 | -1.01 | -1.14 | 0.22 | -1.44 | -1.18 | -2.35 | 0.90 | 0.00 |
| $Cr \rightarrow C$ | 0.00 | 0.86 | 0.48 | -0.15 | 0.75 | 1.67 | 1.42 | 0.86 | 0.00 |
| $C \rightarrow N$ | 0.00 | -0.15 | 0.25 | 0.96 | 0.09 | 0.11 | -1.30 | -0.49 | 0.00 |
| $N \rightarrow F$ | 0.00 | -0.11 | -0.33 | -0.42 | -0.17 | -0.30 | 0.08 | -0.01 | 0.00 |

The convergence shown here is almost identical to the convergence shown in Table 8-2. That the convergence is identical provides reassurance about the ability of creeping flow to model the flow field and that the convergence is not dependent on the fluid flow physics used in the model. Therefore, only the solution using the most refined mesh needs comparison in Section 8.2

## 8.2 Negligible Inertial Effects

Of crucial importance to the success of the predictive model is to ensure that the fluid simulations used to generate the empirical data is operating within the criteria for a Darcy flow regime. Without the confirmation that the fluid flow

through the geometry can be defined as Darcy's law, pressure drop cannot be defined as linearly related to permeability and the functions developed in Sections 9 and 10 break down.

The major criteria for Darcy's law is that the inertial effects acting on the fluid flow can be regarded as insignificant. The flow through the geometry is tested for this criteria by comparing the solutions found using laminar flow physics (which takes inertial effects into account) and creeping flow physics (which does not take inertial effects into account). If the two flow physics provide answers similar enough to each other within a specified tolerance (here 1% is used) then the conclusion can be drawn that inertial effects are negligible and the fluid is acting within the Darcy regime. Table 8-5 outlines the comparison between the average interface pressures found using a very refined mesh. The absolute difference is taken by subtracting the two values

$$P_{\text{Laminar}} - P_{\text{creeping}} \tag{8.1}$$

and the relative difference is found by

$$\frac{P_{\text{Laminar}} - P_{\text{creeping}}}{P_{\text{Laminar}}} \times 100\% \tag{8.2}$$

*Table 8-5. Comparative study between laminar and creeping flow physics*

| Interface | Laminar (Pa) | Creeping (Pa) | Absolute Difference (Pa) | Relative Difference |
|---|---|---|---|---|
| Inlet | 1000.00 | 1000.00 | 0.00 | 0.000% |
| (2) | 876.23 | 876.33 | -0.11 | -0.012% |
| (3) | 750.67 | 750.78 | -0.11 | -0.015% |
| (4) | 625.86 | 625.97 | -0.11 | -0.017% |
| (5) | 499.80 | 499.91 | -0.11 | -0.022% |
| (6) | 373.88 | 373.99 | -0.11 | -0.029% |
| (7) | 249.15 | 249.26 | -0.11 | -0.043% |
| (8) | 123.31 | 123.41 | -0.10 | -0.083% |
| Outlet | 0.00 | 0.00 | 0.00 | 0.000% |

From the relative and absolute differences, it is very clear that the pressure values are almost identical between the two flow physics with only a systematic 0.11 Pa error. While the relative error increases at lower pressure values the highest value for relative error (-0.083%) is far below the 1% limit on permissible relative error. Therefore, it can be concluded that inertial effects are insignificant and that the flow operates within the Darcy regime. The whole study was conducted on a geometry with $L_0 = 1.0mm$ which is the maximum unvaried pore length used in this study. As such, the result found here will apply to all other pore sizes used, as they are shown to have a lower Reynolds number than the $1.0mm$ pore length placing them within the Darcy regime as well.

# 9 Constant Porosity Case Study

*Previous literature had shown that the permeability of a pore was proportional to the length scale of the pore squared* $\left(K \propto L_0^{\,2}\right)$. *The dependency was shown to be applicable here as well, with simulations of this geometry showing that there is a strong correlation of the form* $K_0 = C_0 L_0^{\,2}$ *where* $C_0 = 0.0396$. *Case Study One: The permeability dependence of length variation was also investigated and it was found that a linear approximation accurately described the permeability within 2.5%. The empirical model uses* $C_0$ *as a constant and introduces a linear term denoted* $C_\varepsilon$. *The linear term* $C_\varepsilon$ *was also shown to be proportional to* $L_0^{\,2}$, *giving the predictive equation the form* $K = (C_0 - C_\varepsilon \cdot \varepsilon) L_0^{\,2}$. *A compartmental model was developed that used the resistance of individual blocks to build a summation sequence that can be used to empirically determine the flow rate and local pressure in the geometry based on the empirically determined values of permeability and geometric parameters. Stepwise functions were developed and used to predict local pressure. Flow rate was predicted with a maximum error of 0.4% and local pressure was predicted with a maximum error of 2 Pa for a total pressure drop of 1000 Pa. Predictions made were accurate for geometries where block experienced different length variations.*

## 9.1 Permeability of unvaried geometry

The permeability of unvaried geometry can be related to the pore size. In Equation (9.1), the '0' subscript refers to the unvaried geometry and $L_0$ is the pore size (taken as equal to the hydraulic diameter).

$$K_0 = C_0 L_0^{\,2} \tag{9.1}$$

Figure 9-1 below is the result of numerical simulations in COMSOL based on the model geometry in Figure 9-1. A Parametric study is conducted where the Pore Size $(L_0)$ is varied between 0.25 mm and 1.25 mm. Permeability is then derived through the use of Darcy's law. The data is plotted and a quadratic trend line is fitted to the data. The equation of the trend line is displayed in Figure 9-1 and is shown to fit very well to the simulation data.

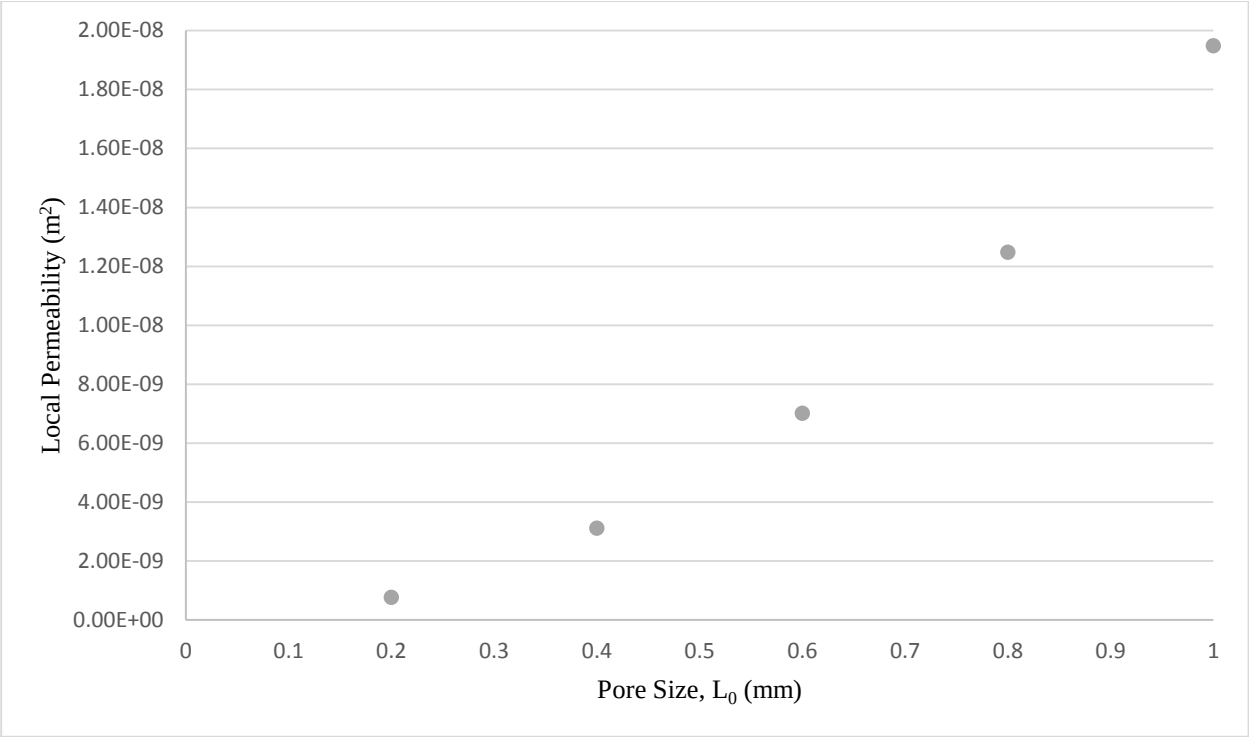


*Figure 9-1. The empirical relationship between pore size and simulated permeability for the studied geometry*

The coefficient for the linear term and the constant in the equation describing the trend line are both are several orders of magnitudes than the quadratic coefficient. Removal of the linear and constants terms produce a maximum error of less than 1%, and are therefore regarded as negligible. The result of the simulation is proof that the permeability is directly proportional to the square of the pore size. For this geometry, $C_0$ is found to be $0.0396$.

## 9.2 Permeability as a function of length variation

The square pores in the un-varied state have a square-shaped cross sectional area. This provides several simplifications to the study. Firstly, the length-scale ($L_x$) is equivalent to the pore size ($d$). Secondly, the porosity of the media ($\phi$) remains constant as the media varies in the z-direction. It is assumed that the length variation in the z-direction will represent the majority of the length variation that occurs in the media. The major reason for this is that the length variation of solid penetrated by a fluid mainly occurs in the direction of flow. Local length variation of a solid is dependent on local pressure and stress propagated through the impermeable solid. The length variation of the solid is expressed as the length variation ($\varepsilon$) which is dependent on length variation in the z-direction as shown in Equation (9.2). The varied block length is related to the original block length. For this definition, the length variation is equal to 0 in an un-varied state and equal to 1 at the point where the media is varied so strongly that the pores in the media disappear and the media becomes impermeable.

$$\varepsilon = 1 - \frac{L_z}{L_0} \tag{9.2}$$

To examine how the length variation relates to permeability a parametric study was conducted where the length variation was varied for a specific geometry and the flow parameters. The length scales were altered between each parametric study as shown in Table 9-3. Figure 9-2 provides an example of the behaviour observed for a $L_0$ equal to 1.0 mm. The graph demonstrates how permeability decreases as the length variation is increased from 0 to 0.9. From $\varepsilon < 0.6$ the relationship between permeability and the length variation can be approximated as the linear function seen in Figure 9-2. The constant in the linear function is equivalent to the permeability for the un-varied geometry from Figure 9-1. For $\varepsilon > 0.6$ the relationship between permeability and the length variation can be approximated by the quadratic function shown in the graph.

To generate the graph shown in Figure 9-2, raw velocity and pressure data is taken from COMSOL and formatted into tables for data presentation where each row provides local pressure data within the geometry for a given length variation. The data is then processed to determine the permeability for a given geometry. An exemplary set of raw data used to generate Figure 9-2 is provided in Table 9-1. The processed data is shown in Table 9-2. The rest of the data used to develop the models for the constant porosity case can be found in Appendix A.

*Table 9-1. Raw Data for a 2 element geometry with* $L_0 = 0.8mm$

| | Pressure $(Pa)$ | | | | | | | | | Volumetric flow rate, z component |
|---|---|---|---|---|---|---|---|---|---|---|
| $\varepsilon_z$ | $P_{inlet}$ | $P_2$ | $P_3$ | $P_4$ | $P_5$ | $P_6$ | $P_7$ | $P_8$ | $P_{outlet}$ | $Q\ (m^3 s^{-1})$ |
| 0 | 1000 | 875.9 | 749.4 | 624.8 | 500.0 | 375.3 | 250.2 | 124.0 | 0 | 6.23E-09 |
| 0.1 | 1000 | 875.6 | 749.3 | 624.4 | 499.9 | 375.2 | 250.2 | 124.1 | 0 | 6.06E-09 |
| 0.2 | 1000 | 875.6 | 749.2 | 624.6 | 499.8 | 374.9 | 250.5 | 123.7 | 0 | 5.75E-09 |
| 0.3 | 1000 | 875.7 | 749.3 | 624.6 | 500.2 | 375.6 | 250.8 | 124.2 | 0 | 5.26E-09 |
| 0.4 | 1000 | 875.7 | 749.4 | 624.2 | 499.8 | 375.2 | 250.7 | 123.7 | 0 | 4.58E-09 |
| 0.5 | 1000 | 877.2 | 749.8 | 624.4 | 499.9 | 375.4 | 250.5 | 123.2 | 0 | 3.69E-09 |

The average local pressure across each block-to-block interface in the geometry is given for each length variation. The volumetric flow rate is also given, which is found by integrating the simulated velocity of the flow field in the z direction across the interfacial area. The process for extracting this data from COMSOL is discussed in Section 7.7. Once the raw data is extracted, it is processed to create a plot of permeability against length variation. Here the local permeability is calculated by using the pressure values $P_5$ and $P_6$ as they are the furthest from the inlet and the outlet and they're least likely to be impacted by entrance effects (Section 3.3.4).

*Table 9-2. Processed Data for a 2 element geometry with* $L_0 = 0.8mm$

| Def. Ratio | Pressure | | Volumetric flow rate, z component | Block Length | Local Permeability | Area | Reynolds No. |
|---|---|---|---|---|---|---|---|
| $\varepsilon_z$ (-) | $P_5\ (Pa)$ | $P_6\ (Pa)$ | $Q\ (m^3 s^{-1})$ | $L_z\ (m)$ | $K_L^S\ (m^2)$ | $A\ (m^2)$ | Re (-) |
| 0 | 500.0 | 375.3 | 6.23E-09 | 0.80 | 1.25E-08 | 3.2E-07 | 0.16 |
| 0.1 | 499.8 | 375.1 | 6.06E-09 | 0.72 | 1.09E-08 | 3.2E-07 | 0.14 |
| 0.2 | 499.8 | 374.9 | 5.75E-09 | 0.64 | 9.20E-09 | 3.2E-07 | 0.11 |
| 0.3 | 500.2 | 375.6 | 5.26E-09 | 0.56 | 7.39E-09 | 3.2E-07 | 0.09 |
| 0.4 | 499.8 | 375.2 | 4.58E-09 | 0.48 | 5.51E-09 | 3.2E-07 | 0.07 |
| 0.5 | 499.9 | 375.4 | 3.69E-09 | 0.40 | 3.70E-09 | 3.2E-07 | 0.05 |

The block length is calculated based on the specified length variation $(\varepsilon)$ and the unvaried length of the block $(L_0)$ as shown.

$$L_z = L_0(1-\varepsilon_z) \tag{9.3}$$

The area $(A)$ is calculated by multiplying $L_x$ and $L_y$ together which are constant for this constant porosity case study. The local permeability is calculated as shown below. The value for viscosity $(\mu)$ is taken from Table 7-1.

$$K_L^S = \frac{\mu \cdot Q}{A \cdot \frac{P_5 - P_6}{L_z}} \tag{9.4}$$

Reynolds number was also calculated as an additional indication that the flow is in the Darcy regime. The fluid density $(\rho)$ is also taken from Table 7-1. The value of Reynolds number was calculated using an equation analogous to Equation (3.4) from Section 3.1.3 using volumetric flow rate and Area instead of velocity.

$$\mathrm{Re} = \frac{\rho Q L_0}{\mu A} \tag{9.5}$$

The characteristic length scale is defined as $L_0$. As seen in Table 9-2, the Reynolds number for each simulation is below 1, which is defined as the critical Reynolds number for flow to be in the Darcy regime. Therefore, Darcy flow is confirmed for this geometry. A summary of the maximum Re values for each unvaried pore length $(L_0)$ tested is shown in Table 9-3.

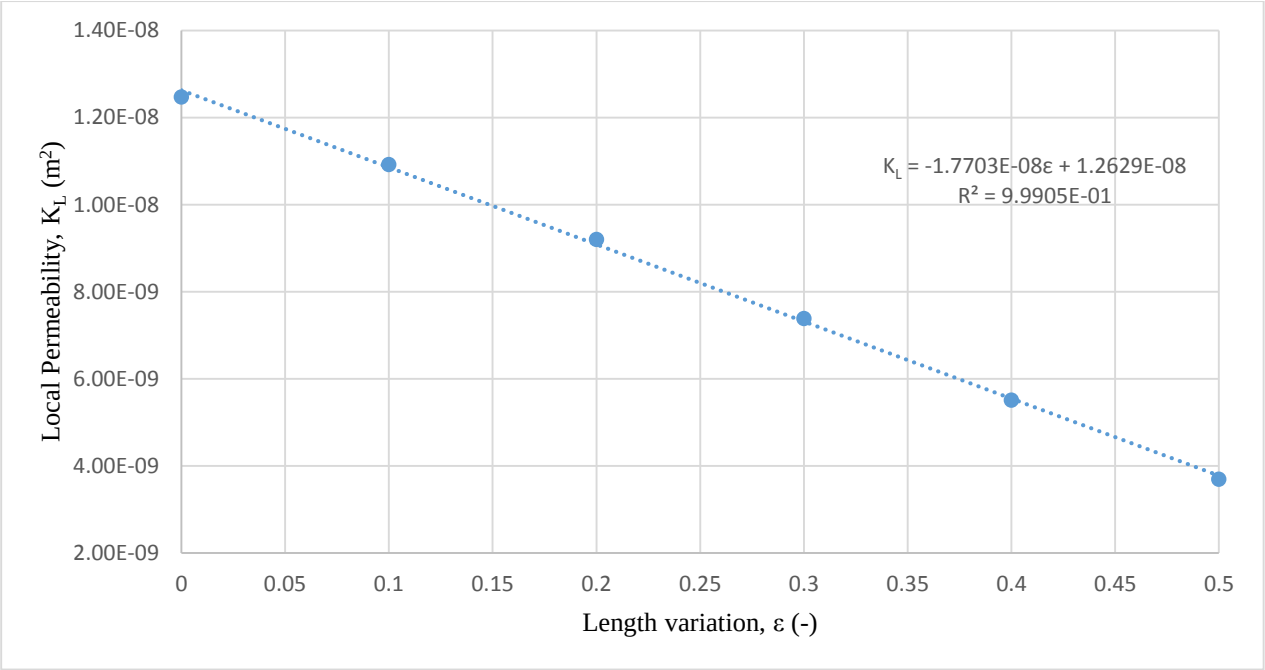


*Figure 9-2. The empirical relationship between length variation and simulated permeability for the studied geometry*

The linear approximation can take the form of the general correlation in Equation (9.6).

$$K_L^S(\varepsilon) = K_{L,0} - C_1 \cdot \varepsilon \tag{9.6}$$

Similar parametric studies for different pore sizes indicate that $C_1 \propto L_0^2$ . The results of the parametric studies are displayed in Table 9-3. Dividing $C_1$ by $L_0^2$ yields $C_\varepsilon$, which is approximately constant for all pore sizes tested.

$$C_1 = C_\varepsilon \cdot L_0^{\,2} \tag{9.7}$$

Using this relationship, it is now possible to express permeability as a function of the length variation, pore size and the geometrical constants ($C_0$ from (9.1) and $C_\varepsilon$). The Reynolds Number calculated for the fluid flow for each pore size is also shown in Table 9-3. Due to the use of creeping flow, the requirement of Re < 1 must be fulfilled for the creeping flow model to be valid, otherwise the assumption of negligible inertial effects may not hold. In this case, the geometries with a pore size greater than 1 mm have Re > 1. For these geometries, the assumption of creeping flow did not hold (Table 9-3), and were discounted from subsequent analysis.

*Table 9-3. Emperical constants found from simulation and used to build the permeability function*

| $L_0\ (mm)$ | $C_1\ (m^2)$ | $C_\varepsilon$ (-) | Reynolds Number(-) |
|---|---|---|---|
| 0.2 | 1.10E-09 | 7.89E-10 | 0.01 |
| 0.4 | 4.42E-09 | 3.16E-09 | 0.04 |
| 0.6 | 9.96E-09 | 7.11E-09 | 0.88 |
| 0.8 | 1.77E-08 | 1.26E-08 | 0.16 |
| 1.0 | 2.77E-08 | 1.97E-08 | 0.24 |

Substituting Equations (9.1) and (9.7) into Equation (9.6) yields a function for permeability. The permeability function (9.8) can be used to predict local pressure and flow rate in porous media.

$$K_L^P(\varepsilon) = (C_0 - C_\varepsilon \cdot \varepsilon) L_0^2 \tag{9.8}$$

Now the permeability of a variable geometry can be estimated for $\varepsilon < 0.5$ and differing pore sizes. The model has only been tested for geometries with constant porosity as defined. Future work should develop the prediction model for geometries where the porosity changes as the geometry varies and assess the capability of (9.8) to predict permeability in such cases.

For this study the bulk fluid flow is in the positive z-direction. It is assumed that any length variation of the porous media occurs in the direction of bulk fluid flow, as any length variation perpendicular to fluid flow is constrained by incompressible fluid flowing through the media. Hence, the following numerical simulations the solid only varies in the z-direction. Numerical simulations are conducted, where we can calculate local permeability $\left(K_L^S\right)$ and global permeability $\left(K_G^S\right)$ by rearranging Darcy's law to form Equation (9.9).

$$K_s = \frac{\mu \cdot u}{\frac{\Delta P}{\Delta L}} \tag{9.9}$$

Using Equation (9.8) to predict local permeability can allow $K_l$ to be a parameter that represents the ability of a defined section of a porous medium to conduct fluid flow. Based on this application, resistor network theory can be applied to flow in porous media.

$$Q_G^P = \frac{\Delta p}{\mu} \frac{1}{R} \text{ where R is defined by: } R = \frac{\Delta L}{K_L^P \cdot A} \tag{9.10}$$

In addition, $Q$ is the volume flow rate, $\Delta P$ is the pressure gradient across the section and $A$ is the wetted area. The resistor theory can account for changes in parameters along the fluid path through the porous media. This is achieved

by the discretization of the medium into resistors. The flow rate through multiple resistors is found through equation (9.11).

$$Q_G^P = \frac{\Delta p}{\mu} \frac{1}{\sum R_i} \tag{9.11}$$

Rearranging Equation (9.11) yields Equation (9.12). If the initial pressure at the inlet ($P_0$) is known, Equation (9.12) can be converted to a stepwise equation that can predict local pressure at discrete points in the direction of fluid flow (Equation (9.13)).

$$\Delta p = Q_G^P \cdot \mu \cdot \sum \frac{L_i}{K_i \cdot A_i} \tag{9.12}$$

$$p_i = p_{i-1} - Q_G^P \cdot \mu \cdot \sum_{i=1}^{n} \frac{L_i}{K_i \cdot A_i} \tag{9.13}$$

The resistor approach allows for the estimation of flow rate and local pressure without the requirement to numerically solve complex equations such as the Navier-Stokes equations. Another benefit is the use of geometric values as well as fluid viscosity and pressure gradient as the input parameters. These can be easily measured and controlled in experimental application. Results predicted by the resistor method is compared to benchmark simulation data.

## 9.3 Evaluation of the Permeability Function

The ability of (9.13) to predict local pressure was tested by simulating fluid flow in the geometry at the locations in Figure 9-4 where values for local pressure are also found. The simulated values were compared to the predicted local permeability within a geometry where each element has a different length variation. The resulting values for a four element geometry are plotted in Figure 9-3 where z-position is the location of the local value measured along the z-axis of the geometry (the direction of fluid flow).

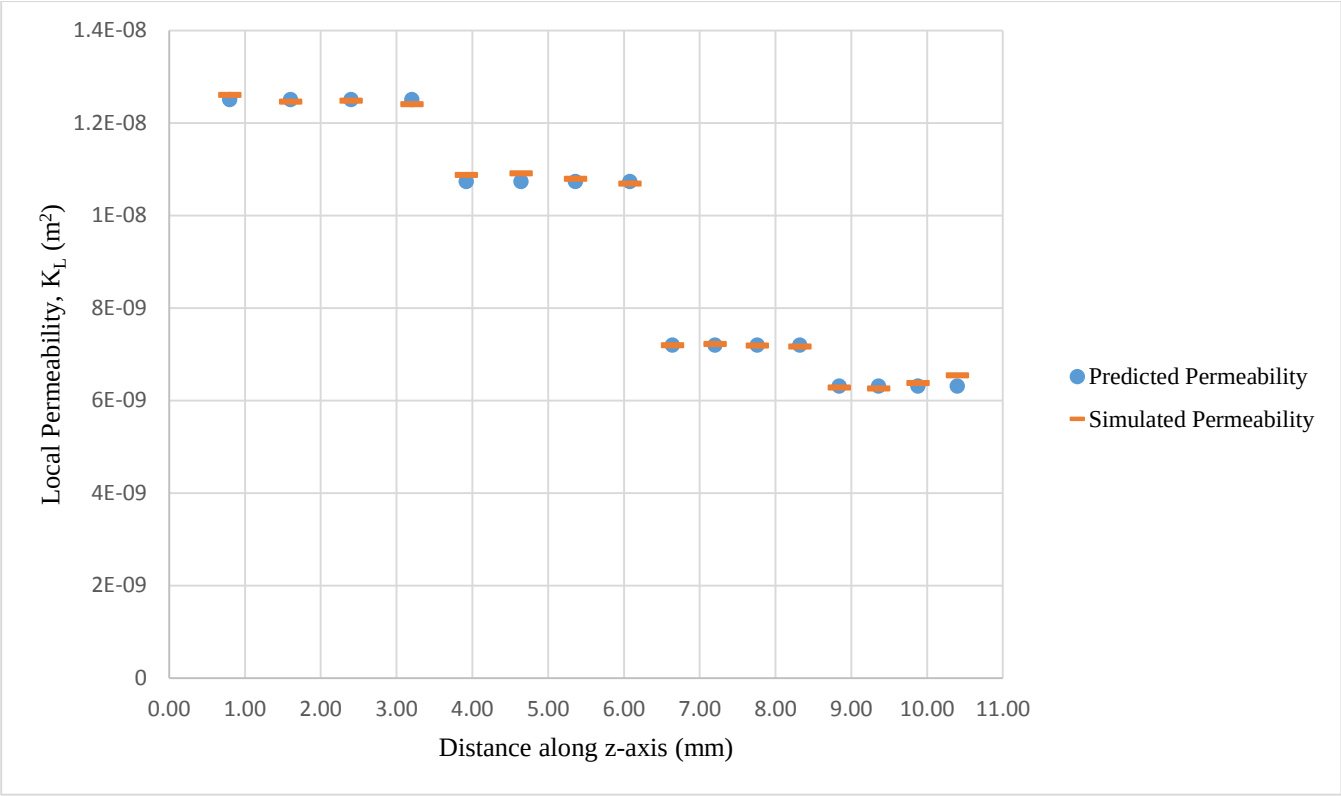


*Figure 9-3. Comparison between simulated and predicted permeability along the z-axis of a 4 element geometry*

Figure 9-3 shows that (9.9) makes accurate predictions of local permeability. Comparisons between predicted and simulated permeability for a range of length variations less than 0.5 and pore sizes were conducted, and the maximum error was found to be 2.5%. It was also noted that blocks which have the same length variation for a given pore size have an equal permeability. In the case of a uniformly varied porous media, it is reasonable to assume that the local permeability is equivalent to the global permeability for this particular geometry. In summary, (9.9) can be used to make an accurate empirical prediction while only requiring geometry related parameters to make the prediction for $\varepsilon < 0.5$. For $\varepsilon > 0.5$, the permeability is no longer linearly proportional to the length variation. With K shown to be empirically predictable, sections 1.4 and 1.5 investigates the use of (9.11) and (9.13) to predict flow rate and local pressure in uniformly varied porous media.

## 9.4 Prediction of Flow Rate

To evaluate the ability of the permeability function to predict flow parameter in porous media, simulations were run for different length variations within the linear region in Figure 9-2. The length variation is varied to assess the ability of the empirical prediction throughout the intended range of varied geometries. The flow rate is used as the parameter to compare predicted and simulated values as it is a variable used in the prediction of local pressure using the piecewise function (9.13).

*Table 9-4. Comparison between predicted and simulated flow rates through a geometry with different length variations*

| | Flow Rate, $Q$ $(m^3)$ | | |
|---|---|---|---|
| Length variation, $\varepsilon$ (-) | Simulated | Predicted | Error |
| 0 | 6.23E-09 | 6.24E-09 | -0.22% |
| 0.1 | 6.06E-09 | 6.07E-09 | -0.25% |
| 0.3 | 5.26E-09 | 5.28E-09 | -0.30% |
| 0.5 | 5.26E-09 | 3.70E-09 | -0.40% |

The results of the simulation show that the prediction of the flow rate is accurate to within 0.5% of the simulated value for the range of length variation within the scope of the thesis. However this error varies depending on the length variation. This is likely due to the linear approximation for the relationship between permeability and length variation at greater length variations. However, the error created is low enough to be deemed negligible.

## 9.5 Prediction of local pressure

With the flow rate predicted, it is now possible to use (9.13) to predict local pressure in each block within the studied geometry. The local pressure is predicted for selected locations within the geometry. The locations used are shown in Figure 9-4. The inlet pressure is used as the initial value $\left(P_0\right)$ and then the stepwise function is advanced using the predicted flow rate and local permeability. The step length $\left(\Delta L\right)$ is taken as the length of the block.

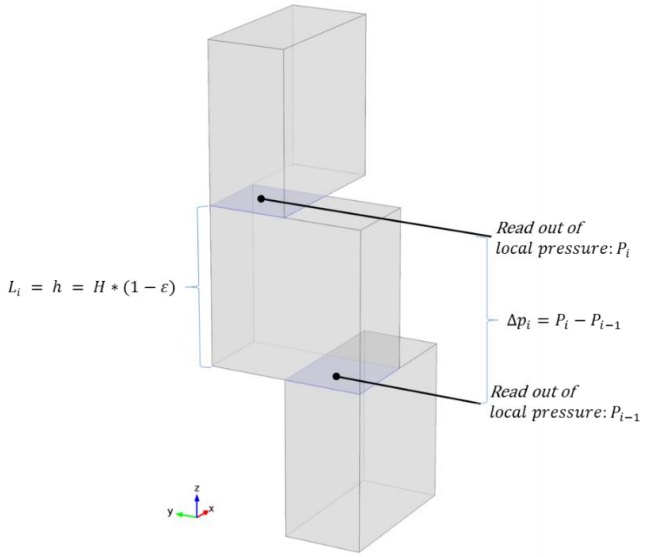


*Figure 9-4. Use of block and interior boundaries to determine simulated values of local pressure and bulk fluid velocity*

The results of the simulation in Figure 9-3 were input into (9.11) and (9.13) to predict values of local pressure for each block in the geometry. The predicted pressure was compared to simulated pressure values for that provided by COMSOL. The results are plotted in Figure 9-5. Very good agreement is found between the predicted and simulated pressure and the error does not exceed 2 Pa. The main source of error is due to the periodic change in the bulk fluid velocity direction. This is not taken into account during prediction of flow rate, so the simulated pressure has a sinusoidal component while the predicted pressure is purely linear and does not predict the small-scale variance.

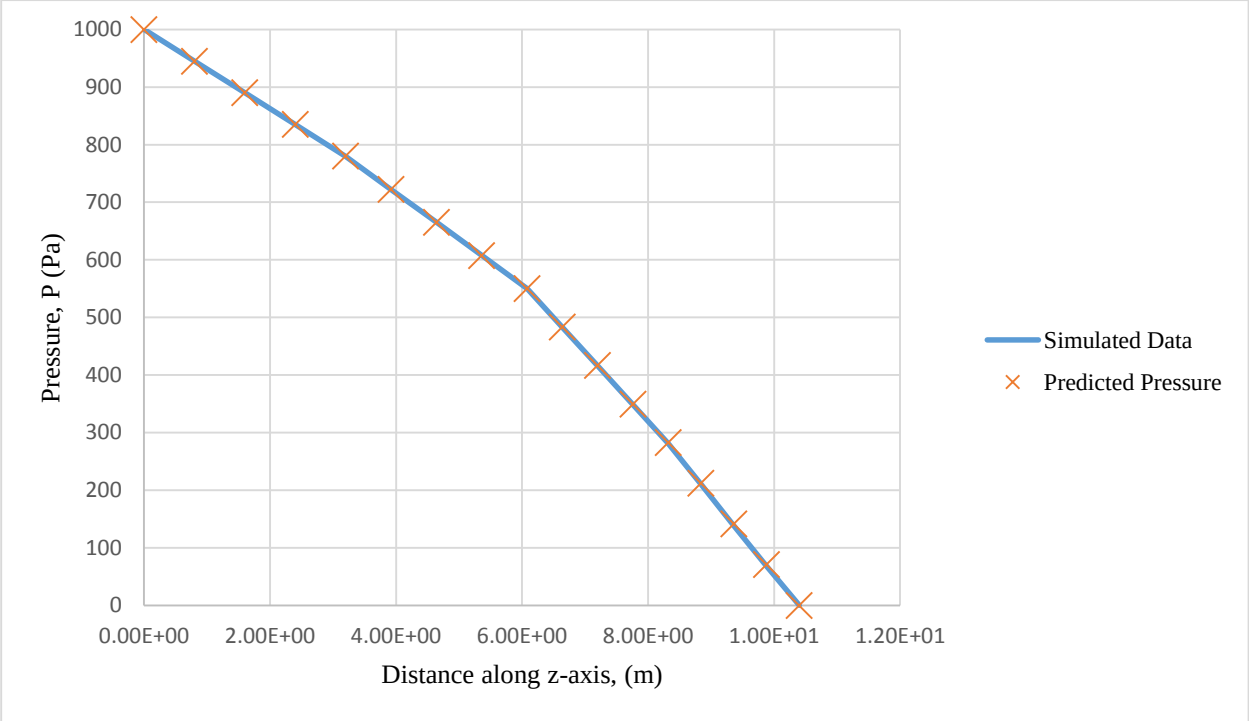


*Figure 9-5.Comparison between predicted and simulated local pressure along the z-axis of a 4 element geometry*

# 10 Variable Porosity Case Study

*For this case, the proportionality* $K_0 \propto L_0^2$ *was found to remain, but the relationship between* $K$ *and* $\varepsilon$ *could no longer be approximated with a linear function as was the case in Section 9. A new parameter was introduced to describe the influence the variable porosity had on the block of interest, and was defined as* $\Delta\varepsilon$ *which was a function of the length variations for the neighbouring blocks and the block of interest and is related to the length variation of each block by* $\Delta\varepsilon = 2\varepsilon_i - \varepsilon_{i+1} - \varepsilon_{i-1}$. *The parameter* $\Delta K$ *was also introduce to denote the difference in permeability between a block affected by non-homogenous porosity and the permeability of a block that is not influenced by porosity. The modified permeability prediction model now has the form* $K_T = \left(a_2\varepsilon^2 - a_1\varepsilon + a_0 + \Delta\varepsilon(\mathrm{b}_1 \cdot \varepsilon \cdot + b_0)\right) L_0^2$. *Substituting all the constants into the modified model, the resulting function for this Cartesian geometry has the form* $K_T = \left(0.0223 \cdot \varepsilon^2 - 0.0430 \cdot \varepsilon + 0.0195 + \Delta\varepsilon(-0.0118 \cdot \varepsilon \cdot + 0.00682)\right) L_0^2$. *Additional case studies and length variation patterns were used to test the limits of this model and determine the accuracy at the maximum values for* $\varepsilon$ *and* $\Delta\varepsilon$. *It was found that blocks with* $\varepsilon = 0.5$ *and* $\Delta\varepsilon = 1.0$ *exhibited the greatest error with 7.17% error in permeability prediction. This error was shown to decrease for smaller values of* $\Delta\varepsilon$ *and created significant improvement in permeability prediction for geometries with non-homogeneous length variation over the standard permeability prediction equation. There is also a noticeable discrepancy between the simulated local permeability values at the inlet and outlet compared to the bulk of the modelled geometry in Figure 10-4 and Figure 10-5. This is in line with the expectation from the literature review in Section 3.3.4 that developing flow and other entrance effects may cause a difference in the measured permeability.*

## 10.1 Prediction of permeability for geometries with variable porosity under length variation

The next step is to increase the complexity of the empirical prediction model to allow the method to broaden its applicability beyond the constant porosity case investigated in Section 9. By finding the simulated permeabilities for the updated geometry developed in Section 5.3, a new model can be constructed in a similar manner to the permeability prediction model developed in Section 9. The model can be used to predict local pressure in the geometry developed in Section 4.2. An initial parametric study was conducted for each of the following pore sizes: 0.2, 0.4, 0.6, 0.8 and 1.0 mm. The length variation ( $\varepsilon$ ) experienced by the geometry was increased from 0 to 0.5 in steps of 0.1 for each parametric sweep. Each parametric study was conducted for a 2 element geometry as depicted in Figure 10-1. The flow through the geometry was given the properties listed in Table 7-1. The properties were chosen to assist the

development of low Re flow was obtained for all cases. The chosen viscosity and density are broadly similar to properties found for a glycerol-water mixture. The pressure drop acts from the inlet to the outlet of the total geometry, and remains constant while the total length of the geometry changes, either through length variation or by the addition of elements. The variation ratio is used as a tool to control how much $L_x$ and $L_y$ are affected by $\varepsilon_z$. The development of $\nu$ is conducted in Section 4.2.3.

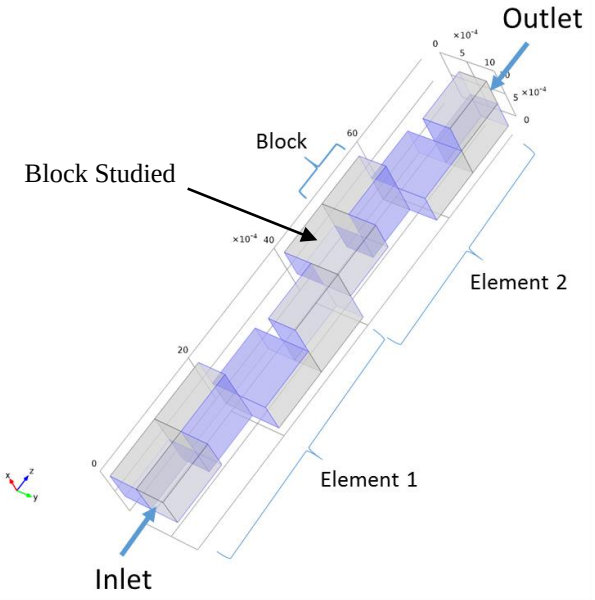


*Figure 10-1. Example of COMSOL™ geometry used to conduct simulations*

The raw data for one of the parametric studies where the unvaried pore length $(L_0)$ was 0.8 mm is shown in Table 10-1. Table 10-2 displays processed data. The raw data obtained is the local flow and geometric data for the block indicated in Figure 10-1 for each length variation applied to the geometry. The inlet pressure was found by taking a surface average across the inlet area into the block. The outlet pressure was found by taking a surface average across the outlet of the block. The block length is determined in the initial set-up of the geometry. The area is found using $L_0$, $\varepsilon$ and the equations developed in Section 5.3.1. The flow rate is extracted from the COMSOL™ data by integrating the simulated velocity profile across the block's cross-sectional area. This particular method to determine flow rate is the same as Equation (10.1)

$$Q = \int_s (\mathbf{V} \cdot \mathbf{n}) dA \tag{10.1}$$

*Table 10-1. Raw data for a 2 element geometry with* $L_0 = 0.8mm$

| | Pressure $(Pa)$ | | | | | | | | | Volumetric flow rate, z component |
|---|---|---|---|---|---|---|---|---|---|---|
| $\varepsilon_z$ | $P_{inlet}$ | $P_2$ | $P_3$ | $P_4$ | $P_5$ | $P_6$ | $P_7$ | $P_8$ | $P_{outlet}$ | $Q\ (m^3 s^{-1})$ |
| 0 | 1000 | 875.9 | 749.4 | 624.8 | 500.0 | 375.3 | 250.2 | 124.0 | 0.0 | 6.23E-09 |
| 0.1 | 1000 | 875.2 | 749.1 | 624.4 | 499.8 | 375.2 | 250.5 | 124.5 | 0.0 | 5.26E-09 |
| 0.2 | 1000 | 875.5 | 749.0 | 624.4 | 499.8 | 374.9 | 250.4 | 124.2 | 0.0 | 4.34E-09 |
| 0.3 | 1000 | 875.5 | 749.3 | 624.6 | 499.9 | 375.6 | 250.5 | 124.1 | 0.0 | 3.45E-09 |
| 0.4 | 1000 | 875.0 | 748.6 | 624.0 | 499.7 | 375.5 | 250.6 | 124.1 | 0.0 | 2.61E-09 |
| 0.5 | 1000 | 875.3 | 749.1 | 624.2 | 500.4 | 376.2 | 250.8 | 124.6 | 0.0 | 1.83E-09 |

The permeability is calculated using Darcy's law using Equation (10.2). The simulated values of pressure and geometry are used in the determination of local permeability. The simulated values of local permeability are denoted using the subscript S, L.

$$K_L^S = \frac{\mu \cdot Q}{A \cdot \frac{\Delta P}{\Delta L}} = \frac{\mu \cdot Q_s}{A \cdot \frac{(P_5 - P_6)}{L_z}} \tag{10.2}$$

*Table 10-2. Sample raw data for the 5th block from the inlet for a 2 element geometry where* $L_0 = 0.8mm$

| EPS $\varepsilon(-)$ | Block Inlet Pressure $P_5$(Pa) | Block Outlet Pressure $P_6$(Pa) | Block length $L_z(mm)$ | Area, $A(m^2)$ | Flow Rate $Q_s(m^3 s^{-1})$ | Permeability $K_{S,L}\ (m^2)$ | Reynolds No. Re $(-)$ |
|---|---|---|---|---|---|---|---|
| 0 | 499.99 | 375.26 | 0.80 | 3.20E-07 | 6.23E-09 | 1.25E-08 | 0.16 |
| 0.1 | 499.83 | 375.21 | 0.72 | 3.07E-07 | 5.26E-09 | 9.90E-09 | 0.12 |
| 0.2 | 499.80 | 374.90 | 0.64 | 2.94E-07 | 4.34E-09 | 7.56E-09 | 0.094 |
| 0.3 | 499.86 | 375.58 | 0.56 | 2.82E-07 | 3.45E-09 | 5.52E-09 | 0.069 |
| 0.4 | 499.68 | 375.46 | 0.48 | 2.69E-07 | 2.61E-09 | 3.75E-09 | 0.047 |
| 0.5 | 500.36 | 376.21 | 0.40 | 2.56E-07 | 1.83E-09 | 2.30E-09 | 0.029 |

The area is calculated based on Equation (5.7) in Section 5.3.1 which now moves beyond the simple calculation made in the constant porosity case to include the effects of length variation and poisons ratio into the cross sectional area of the block. The calculated permeability $\left(K_L^S\right)$ is plotted against the length variation $(\varepsilon)$ in Figure 10-2 for the data in Table 10-2. Length variation is on the x-axis, and permeability $\left(K_L^S\right)$ is on the y axis. Using the method of least squares discussed in Chapter 6, a quadratic curve fit is applied to the data to generate the equation shown in Figure 10-2. The permeability is plotted against length variation for all the un-varied pore sizes specified (0.2, 0.4, 0.6, 0.8, 1.0 mm) and quadratic curve fits are found. Each curve fit has a constant in front of the quadratic term $\left(A_2\right)$, a constant

in front of the linear term $(A_1)$ and a y-intercept $(A_0)$. Therefore the general form of the quadratic fit can be described as shown in Equation (10.3)

$$K_L^S(\varepsilon) \approx A_2\varepsilon^2 - A_1\varepsilon + A_0 \tag{10.3}$$

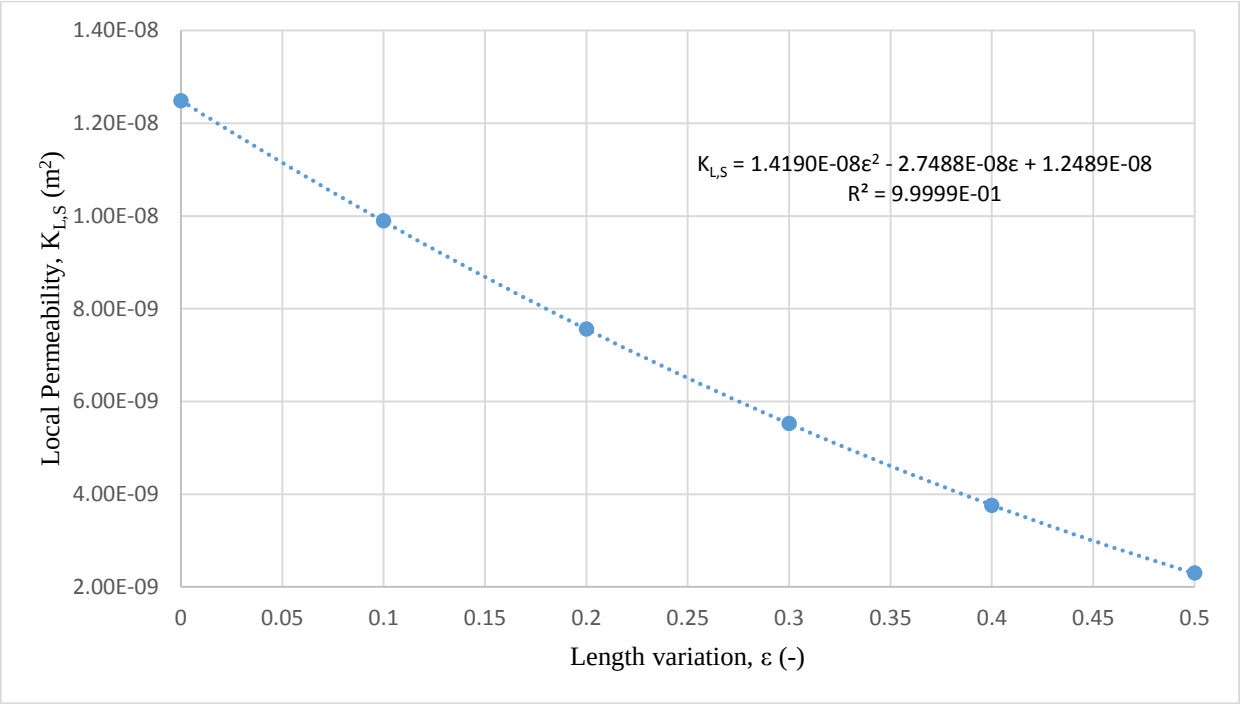


*Figure 10-2. Local Permeability for a 'block' within a 2 element geometry where $L_0$=0.8mm and variable porosity*

The coefficients used in Equation (10.3) to relate simulated permeability to length variation for each pore length are found in Table 10-3. $(A_2)$, $(A_1)$ and $(A_0)$ are then normalised by dividing each coefficient by $L_0^2$. The resulting values are displayed on the right hand side of Table 10-3. The maximum Reynolds number calculated in the parametric study for each un-varied pore length is also shown. Since each Reynolds number is less than 1, the creeping flow assumption remains valid, and calculating permeability using Darcy's law is valid.

*Table 10-3. Coefficients for the polynomial relationship between local permeability and length variation for given pore sizes. The normalised coefficients are also shown.*

| Pore Length, $L_0$ (mm) | $A_2$ ($m^2$) | $A_1$ ($m^2$) | $A_0$ ($m^2$) | $\frac{A_2}{L_0^2}$ (-) | $\frac{A_1}{L_0^2}$ (-) | $\frac{A_0}{L_0^2}$ (-) | Reynolds, Re (-) |
|---|---|---|---|---|---|---|---|
| 0.2 | 8.76E-10 | 1.71E-09 | 7.80E-10 | 0.0219 | 0.0428 | 0.0195 | 0.00973 |
| 0.4 | 3.54E-09 | 6.87E-09 | 3.12E-09 | 0.0221 | 0.0429 | 0.0195 | 0.0389 |
| 0.6 | 8.03E-09 | 1.55E-08 | 7.03E-09 | 0.0223 | 0.0430 | 0.0195 | 0.0875 |
| 0.8 | 1.42E-08 | 2.75E-08 | 1.25E-08 | 0.0222 | 0.0430 | 0.0195 | 0.156 |
| 1.0 | 2.23E-08 | 4.30E-08 | 1.95E-08 | 0.0223 | 0.0430 | 0.0195 | 0.243 |

To determine the relationship between $(A_2)$, $(A_1)$ and $(A_0)$ and $L_0^2$, each coefficient is plotted against $L_0^2$, and the method of least squares is used again to obtain a linear fit as shown in Figure 10-3. All the coefficients are shown have an almost perfectly linear relationship with respect to $L_0^2$. The y-intercept values are on the order of $10^{-4}$ lower than the linear coefficients in Figure 10-3.

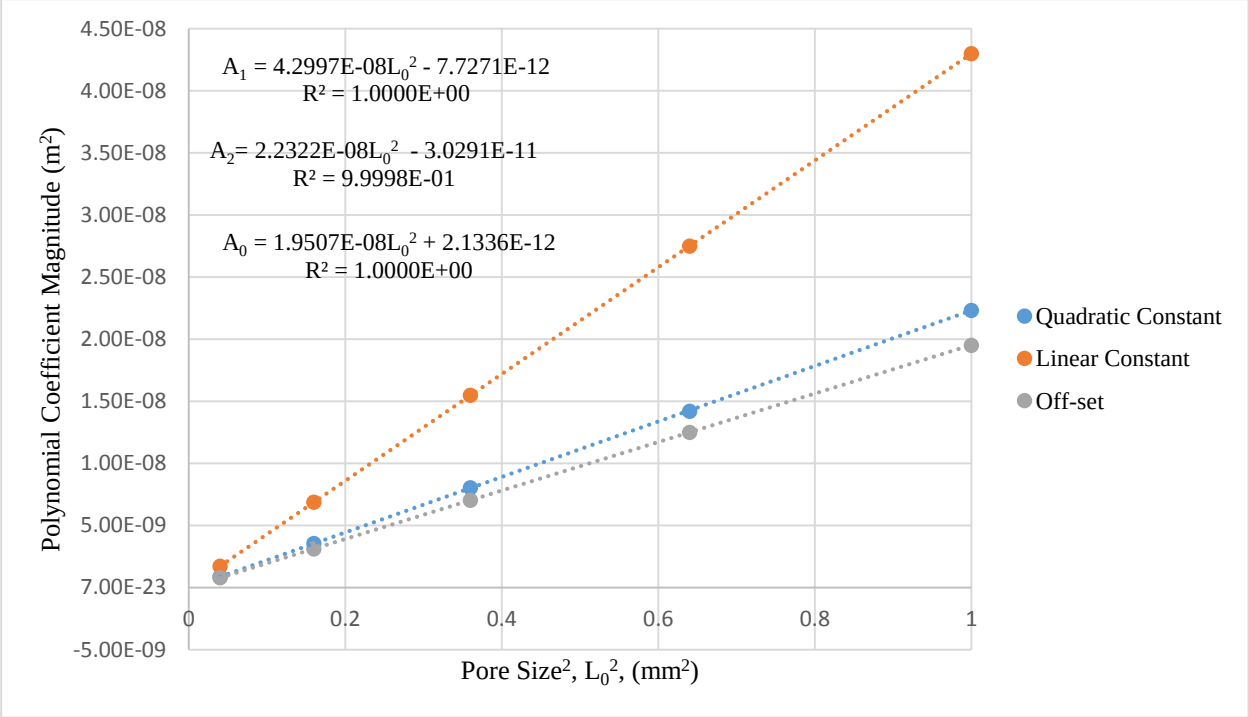


*Figure 10-3. Relationship between the polynomial coefficients from Table 10-3 and the square of un-varied pore length.*

If the y-intercept is taken to be negligible in Figure 10-3, $A_2$, $A_1$, and $A_0$ vary linearly with respect to the square of the un-varied pore length ( $L_0^{\,2}$ ). This relationship can be expressed as

$$\begin{aligned} A_2 &\approx a_2 L_0^{\,2} \\ A_1 &\approx a_1 L_0^{\,2} \\ A_0 &\approx a_0 L_0^{\,2} \end{aligned} \tag{10.4}$$

Where $a_2$, $a_1$ and $a_0$ are the linear coefficients from Figure 10-3. In a similar manner to the predictive equation from Section 9, by substituting in the expressions from (10.4) for $A_2$, $A_1$, and $A_0$ in (10.3) can be adapted to (10.5). Equation (10.5) now uses the obtained coefficients ( $a_2$, $a_1$ and $a_0$ ), length variation $(\varepsilon)$ and un-varied pore length $(L_0)$ to empirically predict local permeability (predicted local permeability is defined by $\left(K_L^P\right)$.

$$K_L^P(\varepsilon) = (a_2\varepsilon^2 - a_1\varepsilon + a_0)L_0^{\,2} \tag{10.5}$$

Where (from Figure 10-3)

$$\begin{aligned} a_2 &= 0.0223 \\ a_1 &= 0.0430 \\ a_0 &= 0.0195 \end{aligned}$$

The values for $a_2$, $a_1$ and $a_0$ are only applicable for the studied Cartesian geometries as specified in Chapter 4. At the current stage of research, there has not been an attempt by the group to investigate the use of the method on a different pore geometry. These values, along with Equation (10.5) can be used to predict the permeability of multiple element geometries that have no change in length variation such as those described in Figure 10-4 and Figure 10-5. The maximum relative error found between the predicted permeability and the simulated permeability is found to be 1.88% for a geometry with a length variation of 0.5.

There is also a noticeable discrepancy between the simulated local permeability values at the inlet and outlet compared to the bulk of the modelled geometry in Figure 10-4 and Figure 10-5. It is hypothesised that this may be due to inlet/outlet effects with developing flow or a form of numerical area. The reason behind this error was not investigated further at this stage of the research as it does not significantly influence results. It is also noticeable that that there is a systematic error between the predicted and simulated local permeability that increases as the length variation

increases with predicted permeability approximately 1-2% more inaccurate than what is predicted for un-varied geometry. This systematic error is due to a limitation of the empirical method as a slight difference in the relationship used in the predictive model compared to the simulated values will increase with magnitude as the length variation increases.

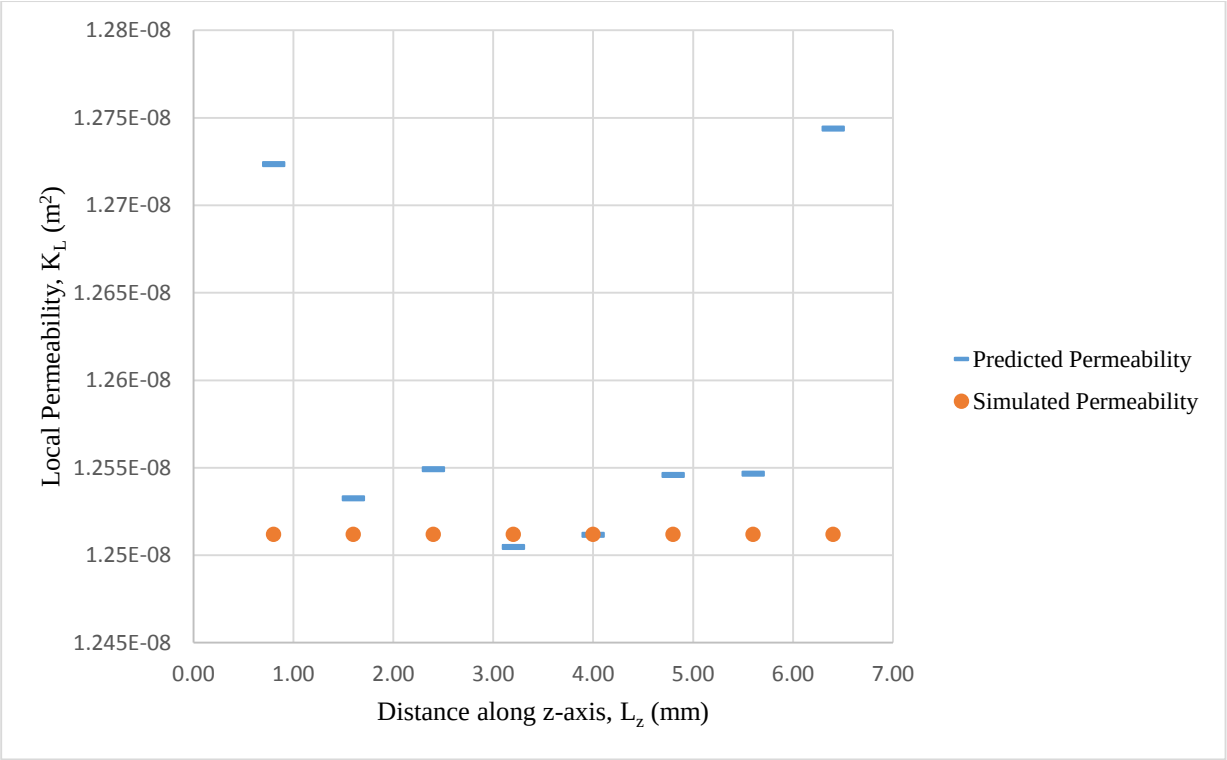


*Figure 10-4. Predicted and simulated permeability for a 2 element geometry ( $L_0 = 0.8mm$ ) where both elements experienced no length variation ($\Delta\varepsilon=\varepsilon=0$)*

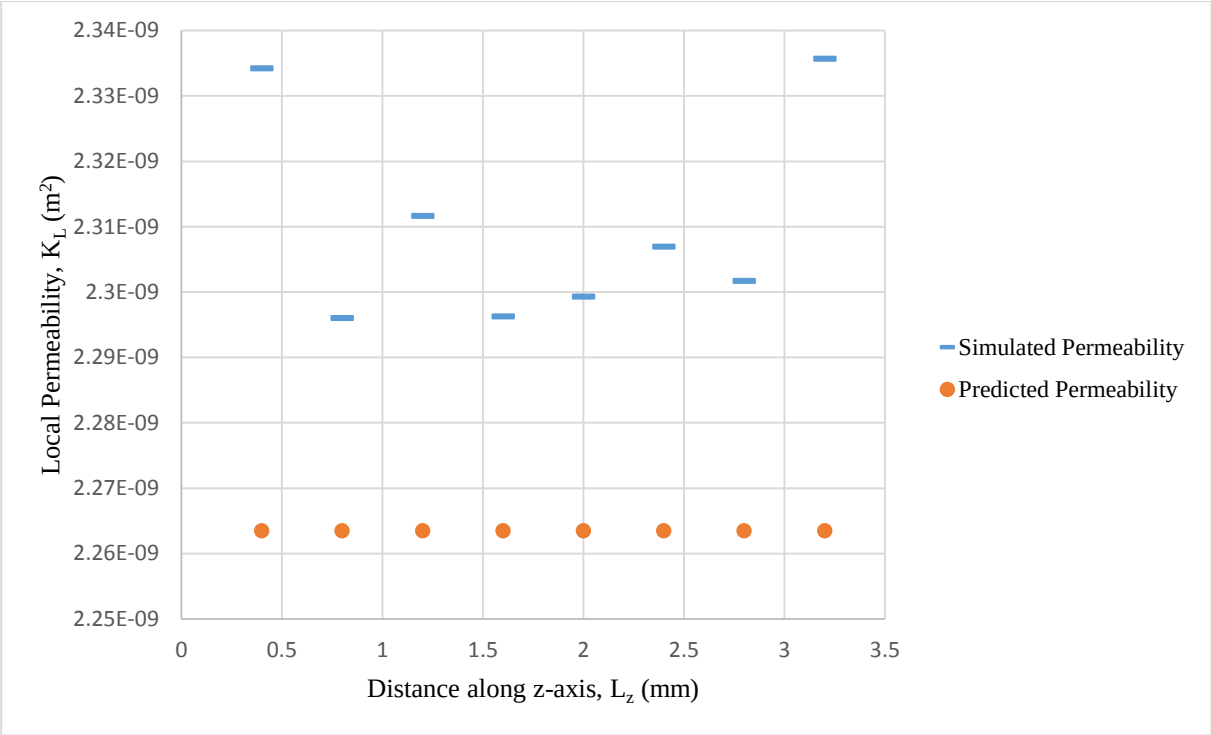


*Figure 10-5. Predicted and simulated permeability for a 2 element geometry where both elements experienced a length variation of 0.5(* $\Delta\varepsilon = 0, \varepsilon = 0.5$ *)*

To create an additional comparison to geometry which maintains a constant porosity under length variation, the simulation shown is recreated for the updated geometry with variable length variation in Figure 10-6. The most notable difference between the results of the two simulations is that unlike the constant porosity geometry, the predicted permeabilities for blocks at the transition between two different length variations are less accurate than the predicted permeabilities for a constant porosity geometry.

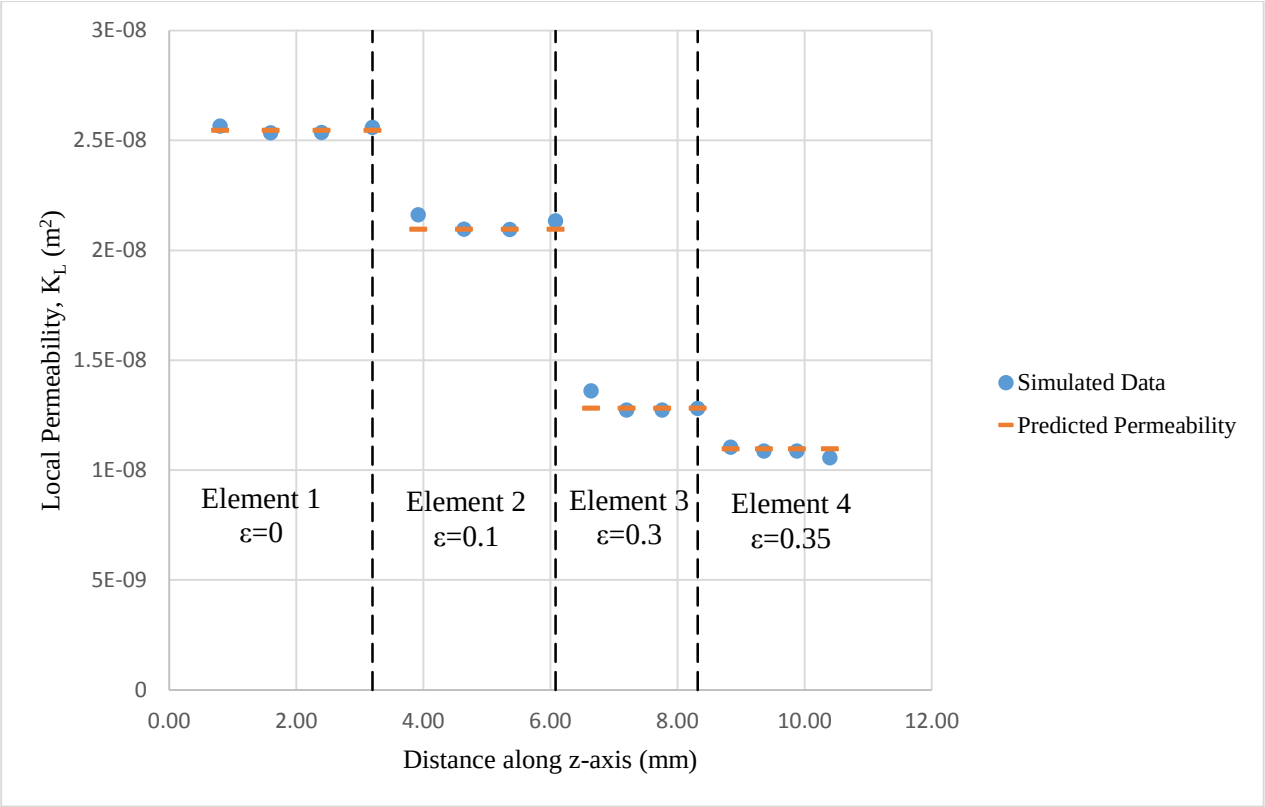


*Figure 10-6. Permeability of a 4 element geometry. Each element experienced a different length variation as shown.*

The apparent 'transition effect' was investigated further in Section 10.2. Some preliminary results are shown in Figure 10-7 and Figure 10-8. With a change in length variation of 0.5 $(\Delta\varepsilon = 0.5)$ used in Figure 10-7, the effects of a change in length variation on the simulated local permeability are clear. Compared to the error found from the simulations shown in Figure 10-4 and Figure 10-5 where no change in length variation occurs, the effect of the transition is substantial. There is a 21.3% error between the predicted and simulated value for the block permeability before the transition and 16.9% error for the local permeability of the block after the transition. The standard predictive equation (10.5) is unsuitable in the current state to model the permeability of geometries with variable porosity that do not have constant length variation.

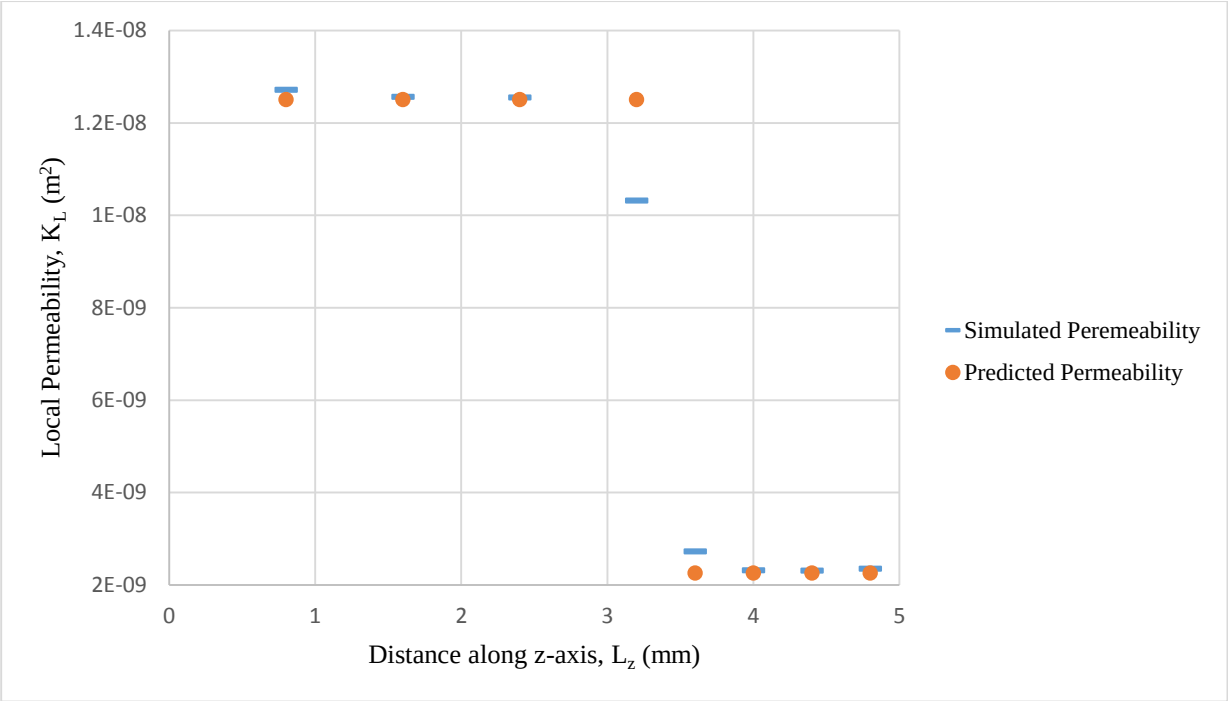


*Figure 10-7. A geometry with 2 elements. The first element experienced a length variation of 0 (ε=0) and the second element experienced a length variation of 0.5 (ε=0.5), causing a change in length variation of 0.5 (Δε=0.5)*

The consequences of the inability to accurately predict the local permeability of blocks that experience a change in length variation has a significant impact on the general predictability of permeability and local pressure in a geometry that has a varying length variation. Figure 10-8 and Figure 10-9 highlight the issue, using a simulation where each block has a prescribed length variation. Each data point represents the permeability of a block with a following length variation (from left-to-right) of 0, 0, 0.3, 0, 0, 0.3, 0. Two major points are made from this particular simulation. Firstly, the simulated values deviate from what is predicted for both increases and decreases in length variation. And secondly, the errors are additive such as in the case for the blocks in Figure 10-8 where they experience two changes in length variation, one at the inlet of the block and another at the outlet.

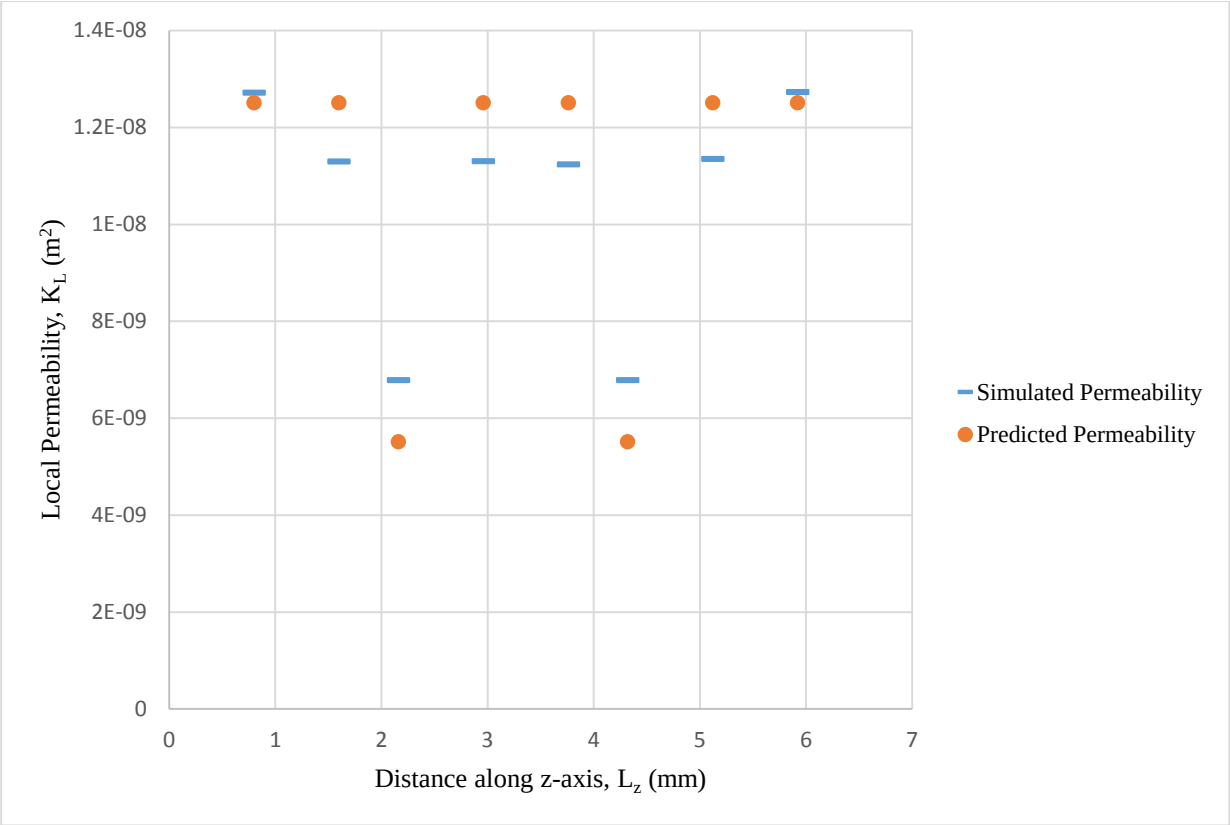


*Figure 10-8. The local permeability of a 2 element geometry where each data point represents a block undergoing a specific length variation. Moving from left-to-right along the z-axis the blocks experience the following length variation 0, 0, 0.3, 0, 0, 0.3, 0, 0*

The permeability error created by a variable length variation extends to the local pressure predictions for a geometry. From Section 9.5, the predicted local pressure is found by using the predicted permeability to determine resistance based upon the cross sectional area as defined by Section 5.3.1 and the length of the block ( $L_z$ ).

The predicted permeability of the geometry shown in Figure 10-8 was used to predict the local pressure for the geometry, with a single pressure value used to approximate the average pressure across each block interface. The results of the pressure prediction were compared to the simulated pressure in Figure 10-9.

To predict the local pressure variation inside a block, would require redefining the length variation to allow a change in length variation along the length of a block. It would however allow for a refined prediction of local pressure and is an aspect of the study that should be developed as discussed in Section 11.2.

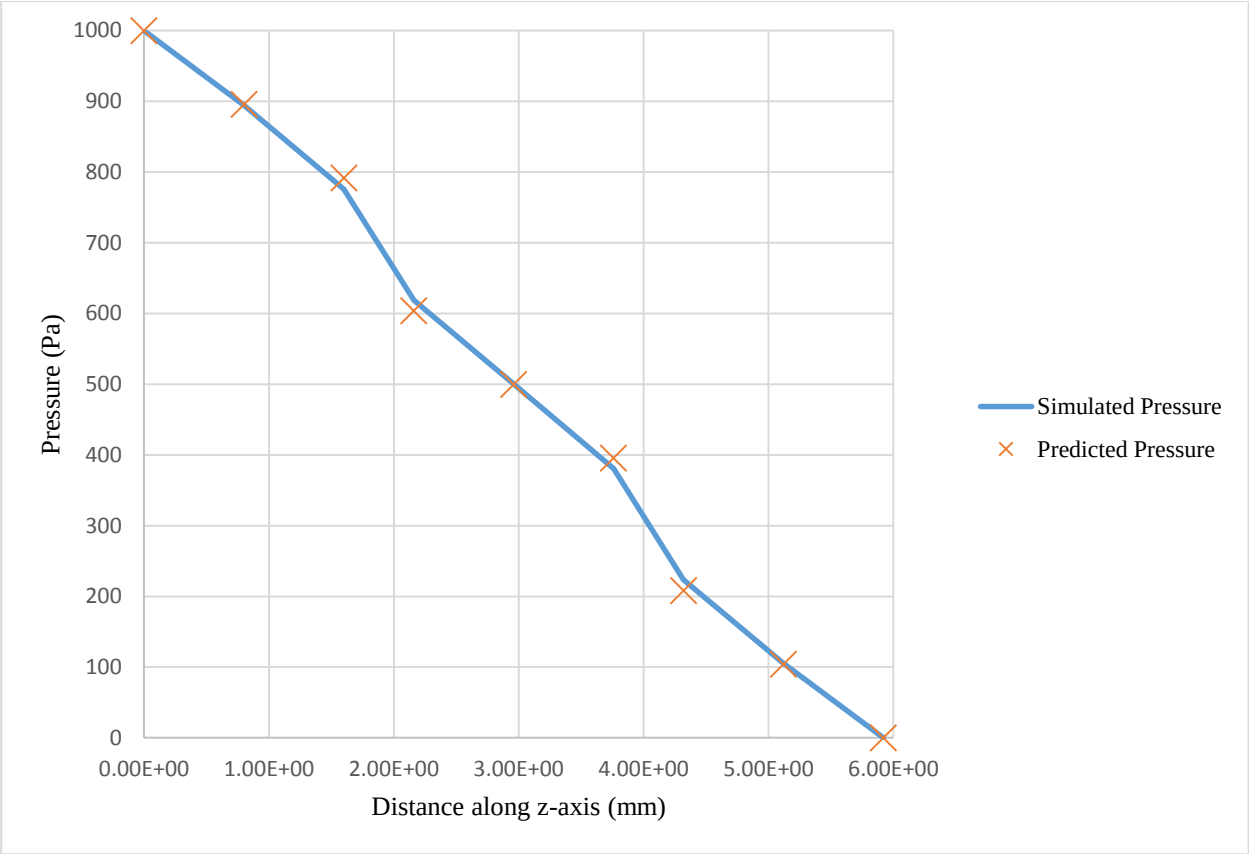


*Figure 10-9. The predicted and simulated local pressure in the two element geometry described in Figure 10-8.*

For the geometry used in Figure 10-8 and Figure 10-9, the error created by an inaccurate permeability prediction causes a difference of 15.3 Pa between the predicted and simulated values of local pressure for the blocks affected by the transition region. Figure 10-10 provides an illustration on the ability of the current model to predict local pressure for a geometry with no change in length variation. In this case, the maximum difference between the predicted values and simulated values for local pressure is 1.3 Pa. Therefore, the error caused by the transition effects are very significant source of error in predicting the local pressure for geometries that have experience changes in length variation.

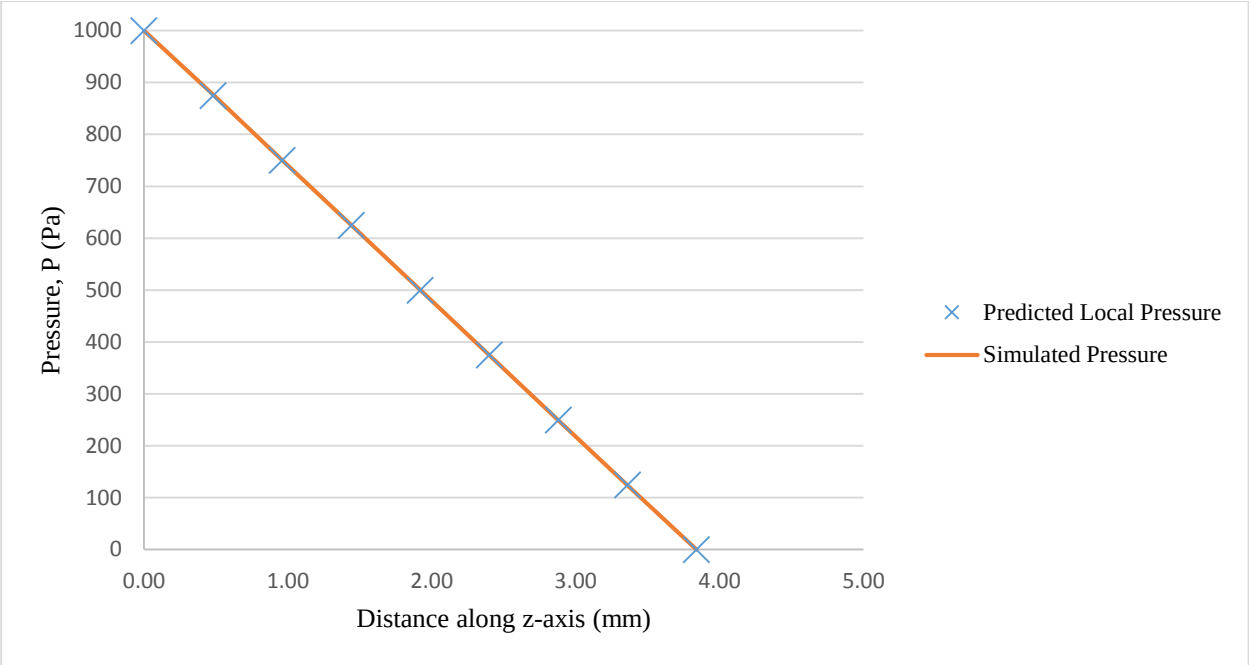


*Figure 10-10. Simulated and predicted local pressure values for a 2 element geometry with a constant length variation of ε=0.4*

To improve the accuracy of the model for geometries with a variable length variation and porosity the empirical relationship between the change in permeability from predicted permeability in affected blocks to the length variation experienced by the block and the change in permeability associated with the block.

## 10.2 Modelling and Prediction of length variation transition effects

To examine the effect of a variable length variation on the local permeability of a model, the geometry in Figure 10-11 was created. The initial simulation was run where element 1 experienced no length variation ( $\varepsilon = 0$ ) and element 2 experienced that maximum length variation ( $\varepsilon = 0.5$ ). Data from this particular case is shown in Figure 10-12. For this simulation, the error between predicted and simulated values for permeability is small (1-2%) for blocks away from the transition where length variation changes from 0 to 0.5. However, there is a significant error (15-20%) between predicted and simulated local permeability for the blocks that the transition occurs between (Blocks 4 and 5). The increased error in predicted permeability caused by the transition has the potential to be very detrimental to the determination of local pressure. An inaccurate permeability affects calculations of block resistance and the predicted flow rate.

In aim to reduce this transitional error, A method is developed that can modify (10.5) to account for $K_L^S$ where it is affected by a change in length variation. A difference in length variation is denoted by $\Delta\varepsilon$ and is the resultant of the

change in length variation between the block of interest ('Block i') and it's neighbouring blocks ('Block i+1' and 'Block i-1'). Therefore $\Delta\varepsilon$ can be defined as

$$\Delta\varepsilon = (\varepsilon_i - \varepsilon_{i+1}) + (\varepsilon_i - \varepsilon_{i-1})$$
$$\Delta\varepsilon = 2\varepsilon_i - \varepsilon_{i+1} - \varepsilon_{i-1} \quad (10.6)$$

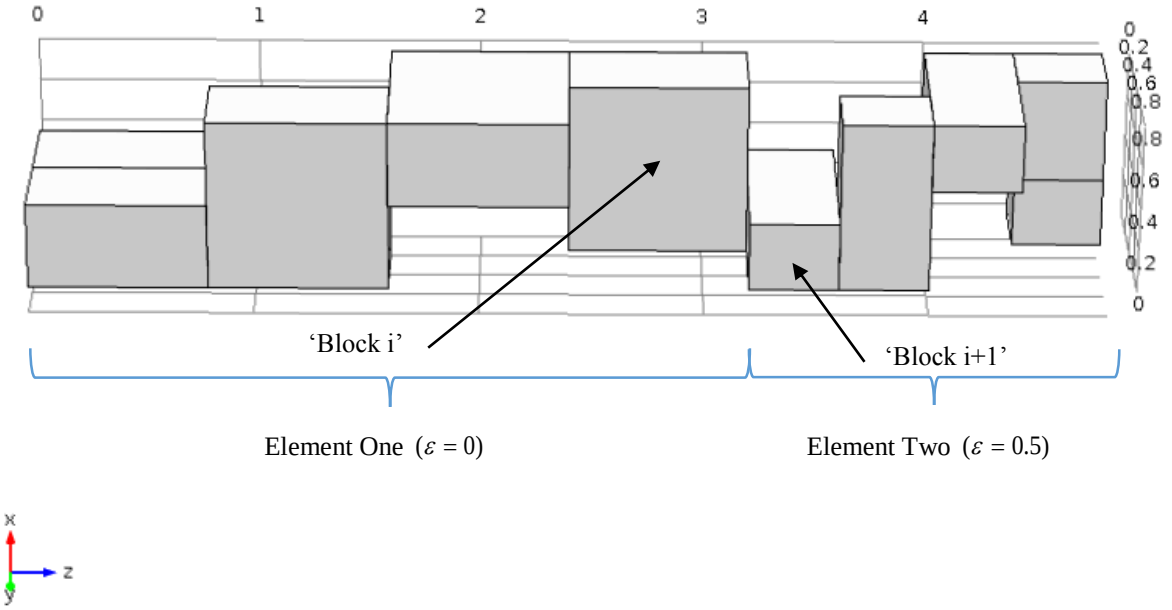





*Figure 10-11. Model Geometry used in determination of* $\Delta K$ *. All* $\Delta K$ *data was taken from 'Block i' and the length variation experienced by 'Block i+1' was varied for a given length variation experienced by 'Block i' to work through different combinations of* $\varepsilon$ *and* $\Delta\varepsilon$ *.*

To analyse how $\Delta K_L^S$ changes with respect to length variation the following relation is assumed.

$$\Delta K_L^S = f(\varepsilon, \Delta\varepsilon) \quad (10.7)$$

Where $\varepsilon$ is the length variation of the block and $\Delta\varepsilon$ is the change in length variation between block *i* and block *i*+1. In the case shown $\Delta\varepsilon$ is positive as the length variation increases from 0 to 0.5. However the model aims to cover positive and negative changes in length variation and effort should be made to predict $\Delta K_L^S$ using a single model regardless of whether the change in length variation is positive or negative.

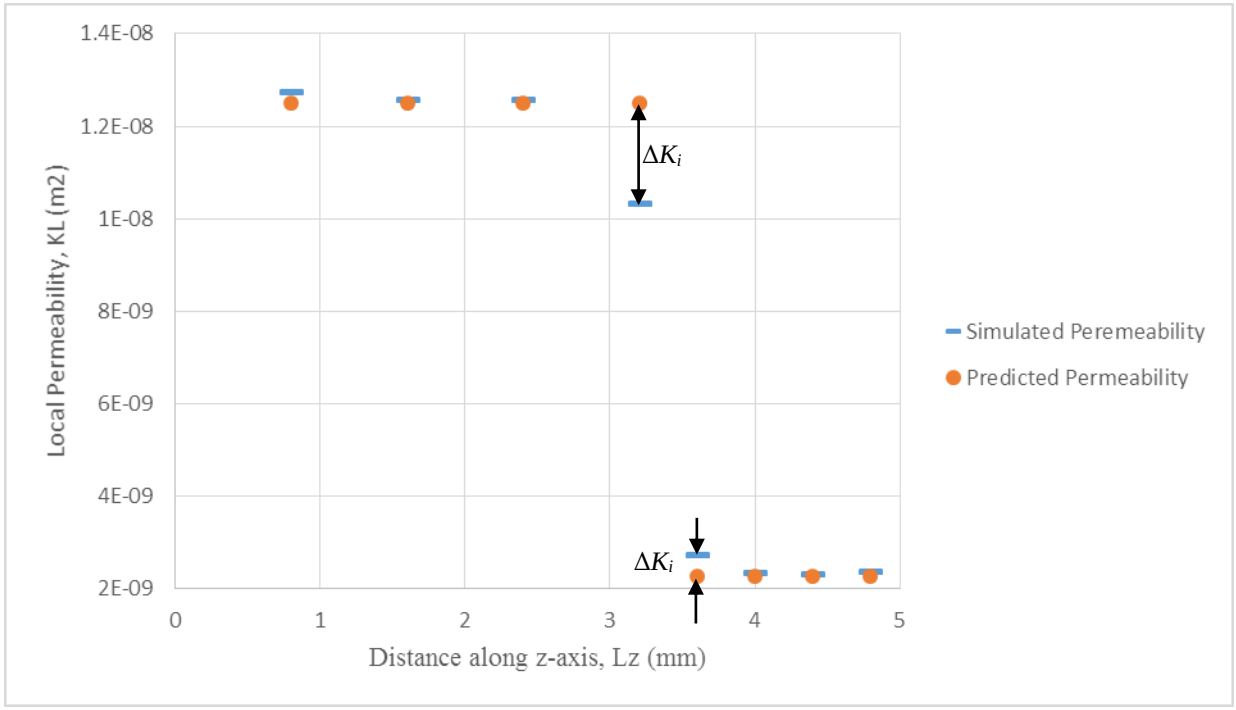


*Figure 10-12. Change in Permeability* $\left(\Delta K_L^S\right)$ *for an increase in length variation of 0.5* $\left(\Delta\varepsilon = 0.5\right)$

The length variation experienced by 'Block i' and 'Block i+1' are individually controlled in the model by altering the length variation of each element that they are a part of. The purpose of extending the modelled geometry beyond what is required to measure the change in Permeability at the transition is ensure that there are errors created at the inlet and outlet don't influence the simulated permeability. It also helps provide a comparative values to highlight the influence of the transition in length variation.

Simulations were conducted for a 2 element geometry with a pore size of 0.8 mm ( $L_0 = 0.8mm$ ) with a single change in length variation between the two elements as shown in Figure 10-11. The length variation experienced by the two elements was systemically altered to establish a full set of $\Delta K_L^S$ values for each combination of $\varepsilon_i$ and $\Delta\varepsilon_i$ . The results of the simulation are shown in Table 10-4. For each column, the length variation experienced by Block i was kept constant while the length variation for Block i+1 was changed to vary the change in length variation. $\Delta K$ was found by subtracting the simulated value of $K_L^S$ for block *i* from the value of $\Delta K_L^S$ for a block that did not experience any change in length variation. The greyed out boxes represent combinations of $\varepsilon$ and $\Delta\varepsilon$ that fall outside of the specified range of the model. These cases were not simulated.

*Table 10-4. Matrix of the simulated difference in local permeability and the permeability of blocks affected by a change in length variation. Each $K_i$ value corresponds to a stated change in length variation from a given reference length variation.*

| $\Delta\varepsilon$ | $\Delta K_i(m^2)$ $(\varepsilon_i = 0)$ | $\Delta K_i(m^2)$ $(\varepsilon_i = 0.1)$ | $\Delta K_i(m^2)$ $(\varepsilon_i = 0.2)$ | $\Delta K_i(m^2)$ $(\varepsilon_i = 0.3)$ | $\Delta K_i(m^2)$ $(\varepsilon_i = 0.4)$ | $\Delta K_i(m^2)$ $(\varepsilon_i = 0.5)$ |
|---|---|---|---|---|---|---|
| 0.5 | | | | | | 4.125E-10 |
| 0.4 | | | | | 5.118E-10 | 3.287E-10 |
| 0.3 | | | | 5.387E-10 | 3.841E-10 | 2.388E-10 |
| 0.2 | | | 4.787E-10 | 3.450E-10 | 2.458E-10 | 1.525E-10 |
| 0.1 | | 2.703E-10 | 2.191E-10 | 1.600E-10 | 1.127E-10 | 6.616E-11 |
| 0 | -7.768E-11 | -5.686E-11 | -2.444E-11 | -1.682E-11 | -1.726E-11 | -7.248E-12 |
| -0.1 | -4.782E-10 | -3.727E-10 | -3.024E-10 | -2.198E-10 | -1.517E-10 | |
| -0.2 | -8.980E-10 | -7.540E-10 | -5.697E-10 | -4.375E-10 | | |
| -0.3 | -1.312E-09 | -1.108E-09 | -8.601E-10 | | | |
| -0.4 | -1.786E-09 | -1.466E-09 | | | | |
| -0.5 | -2.275E-09 | | | | | |

The values from Table 10-4 were plotted in Figure 10-13 and linear regression was used to fit linear relationships to the data of the form $\Delta K_i = \frac{\partial \Delta K_i}{\partial \Delta \varepsilon_i} \cdot \Delta \varepsilon_i + C_1$ . To simplify the relationship the data all the linear fits are assumed to pass through (0,0) i.e. $\Delta K(\varepsilon_i = 0, \Delta\varepsilon_i = 0) = 0$ , reducing the relationship to $\Delta K = \frac{\partial \Delta K}{\partial \Delta \varepsilon_i} \cdot \Delta \varepsilon_i$ . The partial differential is determined through the method of least squares to give a numerical value that is constant for all values of $\Delta\varepsilon_i$ within the range tested by the study.

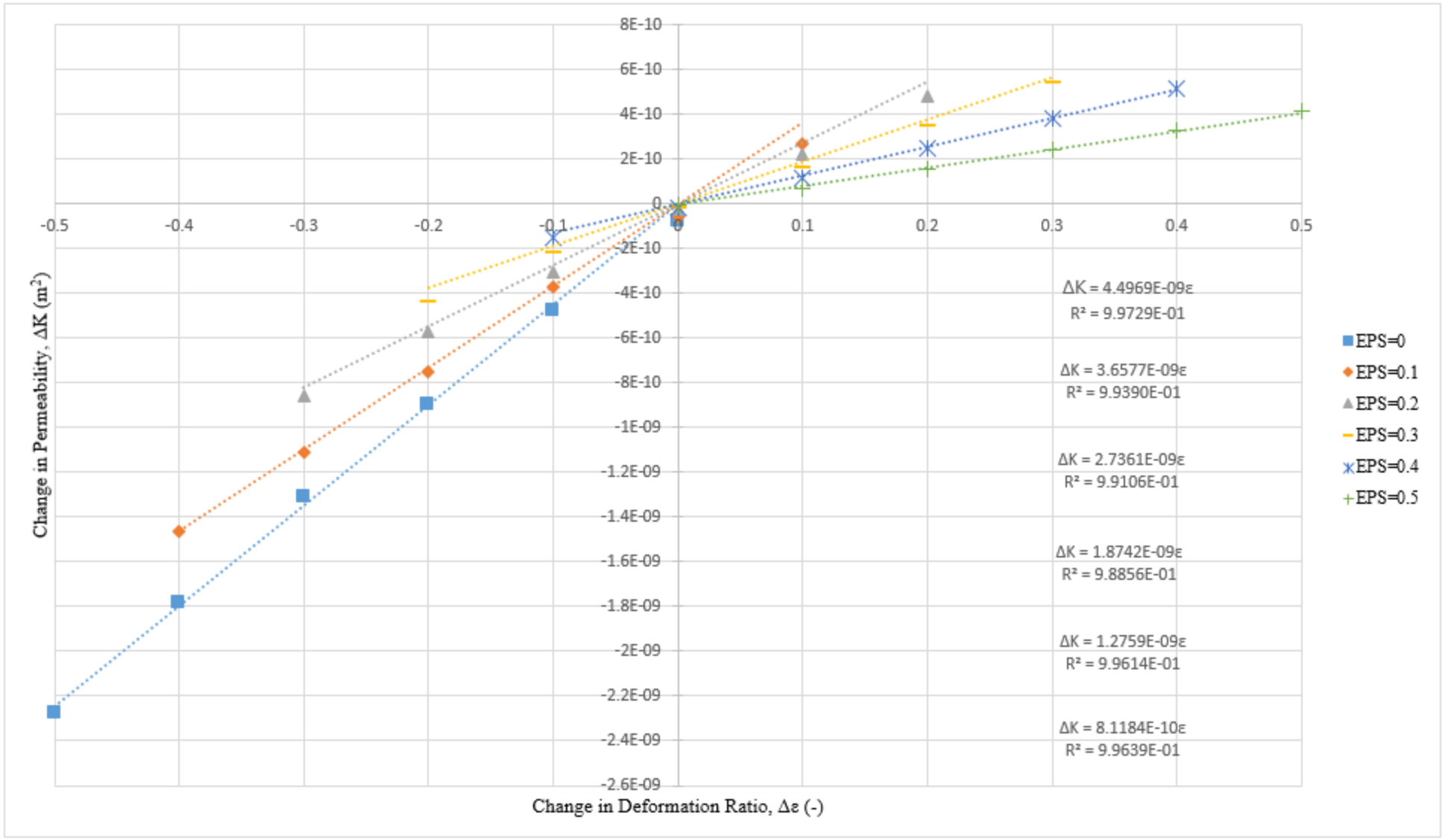


*Figure 10-13. Linear fits describing the transition permeability as it varies for a given change in length variation from a reference length variation*

The linear fits are shown on the right-hand side of the chart. The partial differential $\partial\Delta K_i/\partial\Delta\varepsilon$ describes how $\Delta K$ changes with $\Delta\varepsilon_i$, but from the linear fits it is clear that $\partial\Delta K_i/\partial\Delta\varepsilon$ is not constant for different values of $\varepsilon_i$. This being the case $\partial\Delta K_i/\partial\Delta\varepsilon = f(\varepsilon)$ must be found. This was completed by taking the values of $\partial\Delta K_i/\partial\Delta\varepsilon$ for each value of $\varepsilon_i$ and then plotting $\partial\Delta K_i/\partial\Delta\varepsilon$ on the y-axis and $\varepsilon_i$ on the x-axis as shown in Figure 10-14.

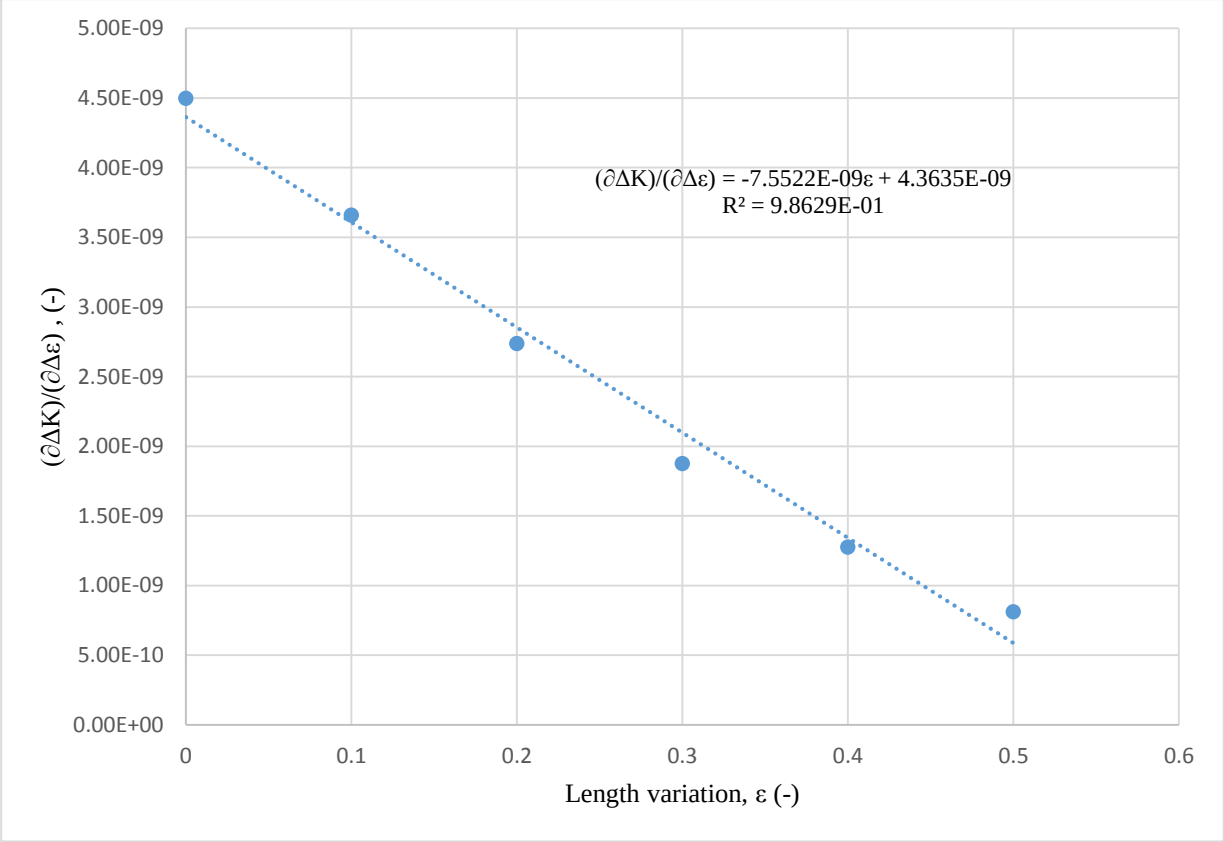


*Figure 10-14. Empirical relationship between $\partial\Delta K_i/\partial\Delta\varepsilon$ and the length variation of Block i*

The plotted data is approximated with a linear fit of the form $\partial\Delta K_i/\partial\Delta\varepsilon = \left(\partial^2\Delta K_i/\partial\varepsilon\partial\Delta\varepsilon\right)\cdot\varepsilon + \partial\Delta K_i/\partial\Delta\varepsilon$. Therefore we have two coupled equations relating $\Delta K$ to $\varepsilon_i$ and $\Delta\varepsilon$.

$$\Delta K = \frac{\partial\Delta K_i}{\partial\Delta\varepsilon}\cdot\Delta\varepsilon \tag{10.8}$$

$$\frac{\partial\Delta K_i}{\partial\Delta\varepsilon} = \frac{\partial^2\Delta K_i}{\partial\varepsilon\partial\Delta\varepsilon}\cdot\varepsilon + \frac{\partial\Delta K_i}{\partial\Delta\varepsilon} \tag{10.9}$$

If Eq. (10.8) is rearranged so that $\partial \Delta K_i / \partial \Delta \varepsilon = \Delta K_i / \Delta \varepsilon$, and is substituted into (10.9) then a single model is formed that approximates the change in $\Delta K_i$ to $\varepsilon_i$ and $\Delta \varepsilon_i$ as shown

$$\frac{\Delta K_i}{\Delta \varepsilon} = \frac{\partial^2 \Delta K_i}{\partial \varepsilon \partial \Delta \varepsilon} \cdot \varepsilon + \frac{\partial \Delta K_i}{\partial \Delta \varepsilon} \tag{10.10}$$

$$\Delta K = \frac{\partial^2 \Delta K}{\partial \varepsilon \partial \Delta \varepsilon} \cdot \varepsilon \cdot \Delta \varepsilon + \frac{\partial \Delta K}{\partial \Delta \varepsilon} \cdot \Delta \varepsilon \tag{10.11}$$

To allow the equation to be applicable to all pore sizes, the $\Delta K$ is divided through by $L_0{}^2$ to create the final form of the model

$$\frac{\Delta K}{L_0{}^2} = \frac{\partial^2 \Delta K}{\partial \varepsilon \partial \Delta \varepsilon} \frac{1}{L_0{}^2} \cdot \varepsilon \cdot \Delta \varepsilon + \frac{\partial \Delta K}{\partial \Delta \varepsilon} \frac{1}{L_0{}^2} \cdot \Delta \varepsilon \tag{10.12}$$

To simplify (10.12), $\partial^2 \Delta K_i \big/ (\partial \varepsilon_i \partial \Delta \varepsilon_i L_0{}^2)$ and $\partial \Delta K_i \big/ (\partial \Delta \varepsilon_i L_0{}^2)$ are labelled $b_1$ and $b_0$ respectively. Through the use of least squares to obtain linear fits, we can approximate both of these partial differential terms using constants. The resulting symbolic equation is shown in (10.13). Substituting in the gradient and y-intercept from Figure 10-14 creates (10.14) which can be used to predict $\Delta K_i$.

$$\frac{\Delta K_i}{L_0{}^2} = b_1 \cdot \varepsilon_i \cdot \Delta \varepsilon_i + b_0 \cdot \Delta \varepsilon_i \tag{10.13}$$

$$\frac{\Delta K_i}{L_0{}^2} = -0.0118 \cdot \varepsilon_i \cdot \Delta \varepsilon_i + 0.00682 \cdot \Delta \varepsilon_i \tag{10.14}$$

The final predicted permeability of a block can now be expressed by adding together the predicted value for $K_L^P$ and $\Delta K_i$ as shown

$$\begin{aligned} K_{total} &= K_L^P + \Delta K_i \\ K_{total} &= (a_2 \varepsilon_i{}^2 + a_1 \varepsilon_i + a_0) L_0{}^2 + \left(b_1 \cdot \varepsilon_i \cdot \Delta \varepsilon_i + b_0 \cdot \Delta \varepsilon_i\right) L_0{}^2 \\ K_{total} &= \left(a_2 \varepsilon_i{}^2 - a_1 \varepsilon_i + a_0 + \Delta \varepsilon_i (\mathrm{b}_1 \cdot \varepsilon_i + b_0)\right) L_0{}^2 \end{aligned} \tag{10.15}$$

If the values for the constants are input to the equation, the complete model can be written as

$$K_{total} = \left(0.0223 \cdot \varepsilon^2 - 0.0430 \cdot \varepsilon + 0.0195 + \Delta\varepsilon(-0.0118 \cdot \varepsilon \cdot +0.00682)\right) L_0^{\,2} \qquad (10.16)$$

A key behaviour of (10.16) is it that for predicting the permeability of blocks that do not experience a change in length variation, the equation reduces to (10.5). Therefore (10.16) can be solely used to predict permeability for all blocks in the geometry instead of requiring different equations depending on how length variation behaves within a geometry.

## 10.3 Analysis of New Model

The first step in testing the effectiveness of the modified model is to compare predictions made by (10.16) to predictions made by (10.5) and determine the reduction in error due to the use of $n$ and $d$ . The next step was to test the adaptability of the model to different pore sizes with various combinations of length variations for each block in the geometry. Finally the minimum number of required simulations are established to allow for acceptably accurate prediction of permeability and pressure in a given geometry must be determined.

### 10.3.1 Comparison to original model

The first comparative study conducted compares the predicted permeability and pressure for a single transition from $\varepsilon_i = 0$ to $\varepsilon_{i+1} = 0.5$. Making a comparison using the largest possible transition aims to highlight any error in the prediction and deviation from simulated behaviour. Figure 10-15 describes the permeability predicted by (10.16) compared to the same simulation data used in Figure 10-7. The accuracy of the predicted permeability values using (10.16) at the transition compared to the originally predicted values is vastly improved. The reduction in error is detailed in Table 10-5.

*Table 10-5. Simulated and predicted permeabilities for each block in a 2 element geometry where the length variation for the first element is 0 and for the second element is 0.5*

| Block | Transition Blocks | | | | | | | |
|---|---|---|---|---|---|---|---|---|
| | 1 ($\varepsilon = 0$) | 2 ($\varepsilon = 0$) | 3 ($\varepsilon = 0$) | 4 ($\varepsilon = 0$) | 5 ($\varepsilon = 0.5$) | 6 ($\varepsilon = 0.5$) | 7 ($\varepsilon = 0.5$) | 8 ($\varepsilon = 0.5$) |
| $K_L^S(m^2)$ | 1.27E-08 | 1.26E-08 | 1.26E-08 | 1.03E-08 | 2.72E-09 | 2.32E-09 | 2.31E-09 | 2.35E-09 |
| $K_{total}(m^2)$ | 1.25E-08 | 1.25E-08 | 1.25E-08 | 1.03E-08 | 2.70E-09 | 2.29E-09 | 2.29E-09 | 2.29E-09 |
| $\delta K_T(-)$ | -1.88% | -0.71% | -0.60% | -0.20% | -0.96% | -1.36% | -0.86% | -2.80% |
| $K_L^P(m^2)$ | 1.25E-08 | 1.25E-08 | 1.25E-08 | 1.248E-08 | 2.288E-09 | 2.29E-09 | 2.29E-09 | 2.29E-09 |
| $\delta K_L^P(-)$ | -1.88% | -0.71% | -0.60% | 20.95% | -16.00% | -1.36% | -0.86% | -2.80% |

For the geometry tested, blocks 4 and 5 are of most interest. Comparing $K_{total}$ to $K_L^P$ for these blocks show that the modified permeability model can reduce the error caused by the transition from 20.95% and -16.00% to -0.20% and -0.96% respectively. The error is calculated relative to the simulated value for permeability $\left(K_L^S\right)$ as shown.

$$\delta K = \frac{K_L^P - K_L^S}{K_L^S} \tag{10.17}$$

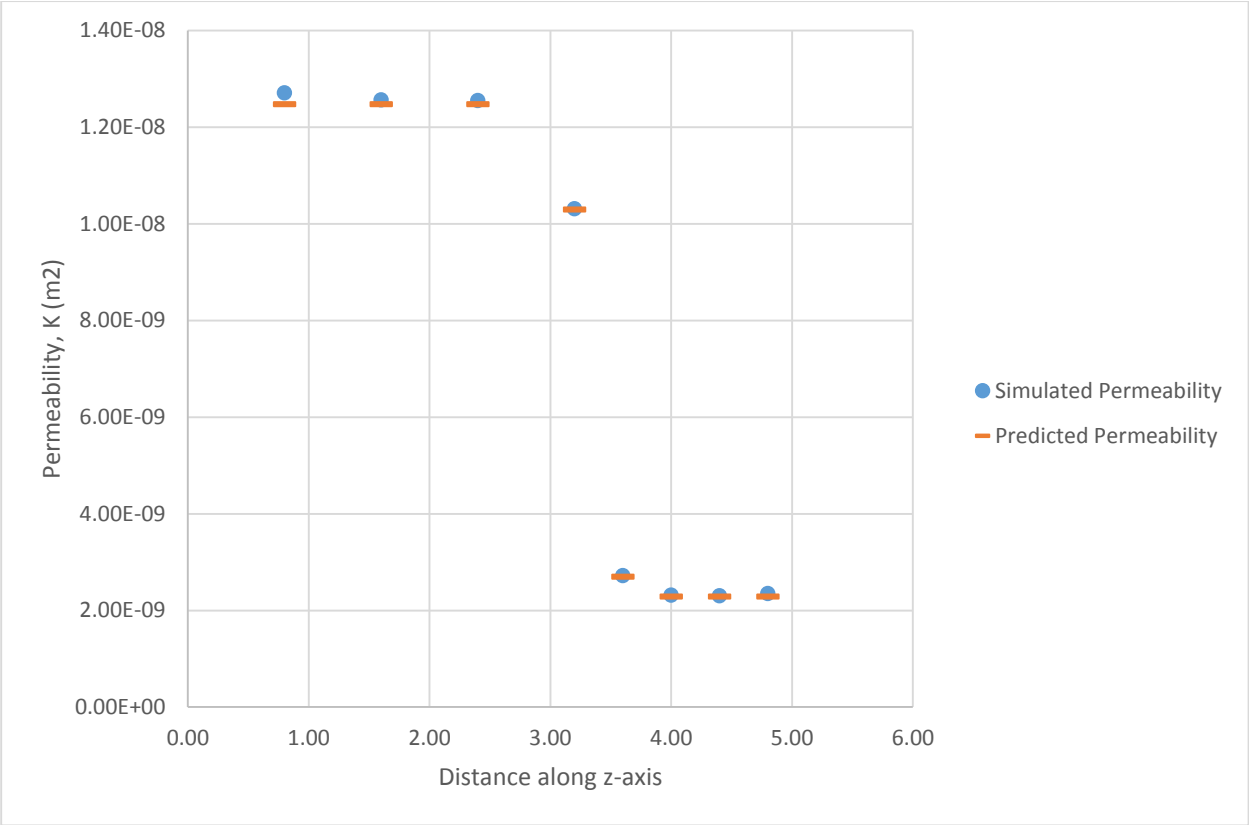


*Figure 10-15. Simulated and Predicted permeability for a 2 element geometry with length variation changing from* $\varepsilon = 0$ *to* $\varepsilon = 0.5$. *The permeability prediction is made using (10.16) to compensate for the transition effects on permeability.*

The next step is to test the model on the simulated data shown in Figure 10-8. The case has blocks that experience a change in length variation at both the inlet and outlet. It is important to understand the performance of the model when additive errors occur due to multiple changes in length variation over a single block. Table 10-6 compares the change in error using the modified predictive equation compared to the original model. The simulated values for pressure and permeability are also stated for reference.

*Table 10-6. Comparative data for predicted Pressure and Permeability for a 2 element geometry. Each block is given an individual length variation.*

| Block | 1 ($\varepsilon = 0$) | 2 ($\varepsilon = 0$) | 3 ($\varepsilon = 0.3$) | 4 ($\varepsilon = 0$) | 5 ($\varepsilon = 0$) | 6 ($\varepsilon = 0.3$) | 7 ($\varepsilon = 0$) | 8 ($\varepsilon = 0$) |
|---|---|---|---|---|---|---|---|---|
| $K_L^S(m^2)$ | 1.27E-08 | 1.13E-08 | 6.79E-09 | 1.13E-08 | 1.12E-08 | 6.79E-09 | 1.14E-08 | 1.27E-08 |
| $P^S(Pa)$ | 894.53 | 775.82 | 618.59 | 500.00 | 380.67 | 223.47 | 105.35 | 5.65E-48 |
| $K_{total}(m^2)$ | 1.25E-08 | 1.25E-08 | 1.25E-08 | 1.03E-08 | 2.70E-09 | 2.29E-09 | 2.29E-09 | 2.29E-09 |
| $\delta K_T(-)$ | -1.86% | -1.13% | 0.96% | -1.22% | -0.62% | 0.94% | -1.62% | -1.97% |
| $\delta P_{total}(Pa)$ | 1.29 | 1.85 | -0.68 | -0.0048 | -0.060 | -2.56 | -1.40 | 4.26E-13 |
| $K_L^P(m^2)$ | 1.25E-08 | 1.25E-08 | 5.51E-09 | 1.25E-08 | 1.25E-08 | 5.51E-09 | 1.25E-08 | 1.25E-08 |
| $\delta K_L^P(-)$ | -1.86% | 10.5% | -18.8% | 10.4% | 11.0% | -18.8% | 9.91% | -1.97% |
| $\delta P^P(Pa)$ | -1.35 | -15.9 | 14.5 | -0.0048 | -15.2 | 15.2 | 1.23 | 3.69E-13 |

*N.B. The predicted and simulated pressure values stated are taken at the outlet of the block*

Figure 10-16 and Figure 10-17 help visualise the improvement in model accuracy shown in Table 10-6. Similar to the improvements discussed in Table 10-5, the error for the predicted local permeability of this more complex geometry is reduced for blocks. The greatest improvement is found for Block 3 and Block 6, which have a length variation of 0.3. The permeability error is reduced from -18.8% to 0.96% and -18.8% to 0.94% respectively for each block. The predicted permeability is improved for all blocks apart from those at the inlet and outlet. These Blocks (Block 1 and Block 8) do not experience a transition in length variation ($\Delta\varepsilon = 0$) and therefore will not be influenced by the modified permeability prediction equation.

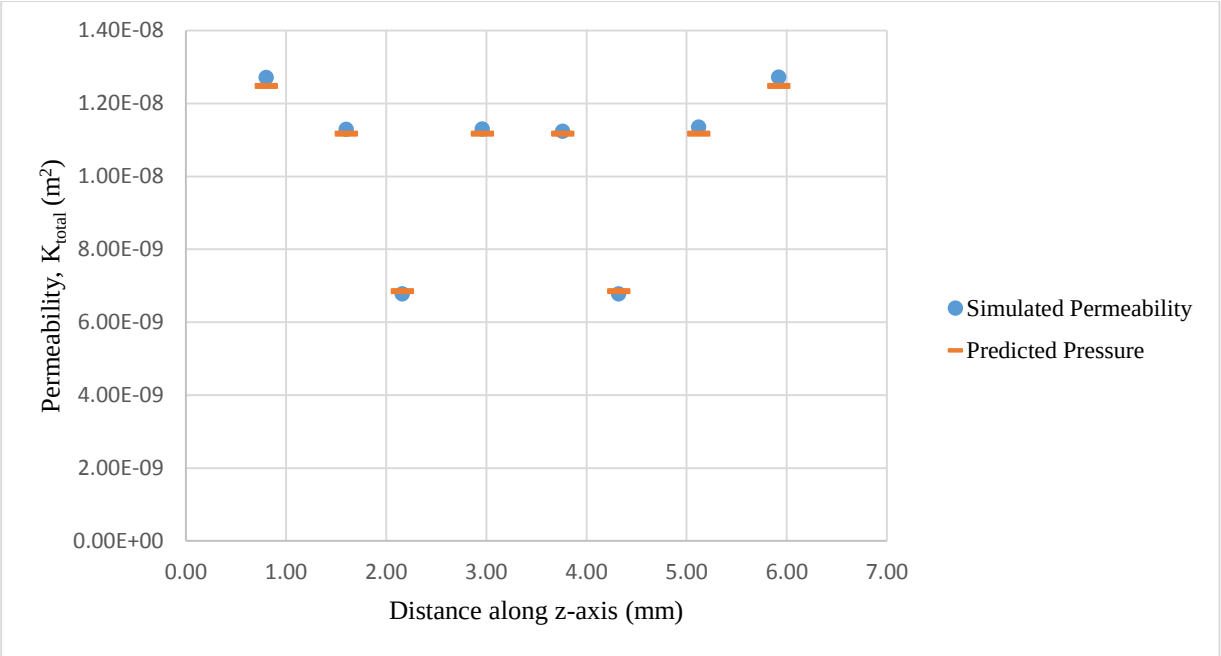


*Figure 10-16. Simulated and predicted permeability for the 2 element geometry in Table 10-6. The predicted permeability values are found using the modified model*

The reduction in permeability error also reduces the error between predicted and simulated values of pressure. The error in pressure values is a difference error. Using absolute error of relative error for permeability provides a more reasonable metric of error in the model across the pressure drop used. In the COMSOL™ models run, pressure was stated to be 1000 Pa at the inlet and 0 Pa at the outlet. The magnitude of the absolute pressure error was found to be independent of the pressure used at the inlet and outlet as long as the pressure drop across geometry remained constant (in this case 1000 Pa). This being the case, an absolute error of 2 Pa for example would create very different relative error values (as calculated in (10.17)) dependent on whether it was calculated for a block with a high local pressure or negligible local pressure. Therefore leading to the misrepresentation of pressure error behaviour that error increases as the local pressure drops. It appears that the pressure error that is still noticeable in the predicted pressure values (Table 10-6) made by the modified model is systematic, created by the periodic variation inherent in the geometry. Including this error, the modified model is able to reduce the range of absolute error values from 30.1 Pa to 4.41 Pa.

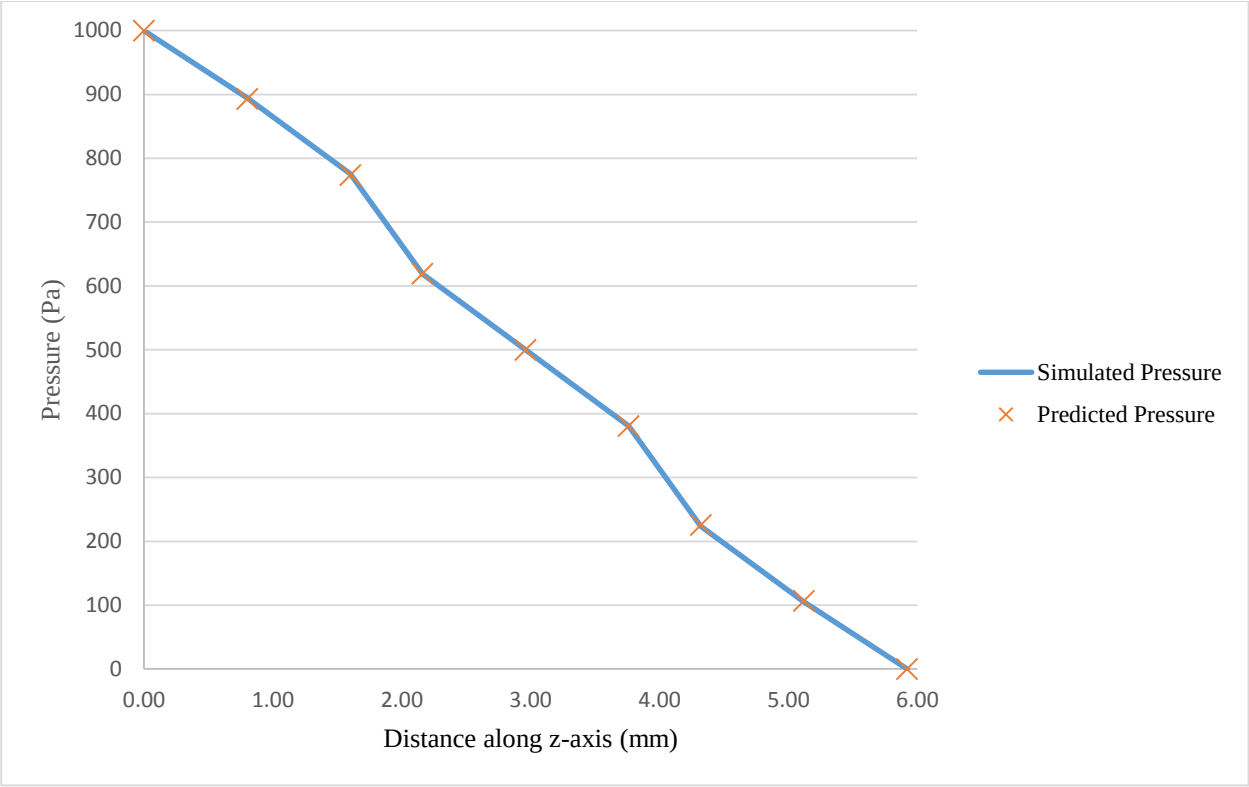


*Figure 10-17. Simulated and predicted Pressure for the 2 element geometry in Table 10-6. The predicted permeability values are found using the modified model.*

From the comparative studies conducted, the modified model can accurately predict simulated data for a geometry. Empirically modelling the transition effects allows for large improvement on the original model. The coefficients determined for use as shown in (10.16) were found using full sets of data. For the model to be shown as suitable for use without excessive simulation, the next step is to determine the minimum number of simulations required to create a model with coefficients that can accurately predict permeability and pressure for geometries of differing pore sizes.

### 10.3.2 Reduction of simulations required for application

The major benefit of consistent using linear and quadratic models is the reduction of data points required to apply a fit using least squares. It is then possible to approximate the relationship between permeability and geometry over a range of length variations. To develop Equation (10.16), three least square fits are made. The first is to make a quadratic approximation of the relationship between local permeability and length variation. The second is to linearly approximate how permeability is affected by a change in length variation from a constant reference length variation. Finally, the linear approximation between permeability and a change in length variation is found for variable length variations.

From Section 10.1, it is known that at least three data points are required for a least squares algorithm to produce coefficients for a quadratic fit and two data points are required to produce a linear fit coefficients. Therefore it is expected that at least 7 simulations are required to create coefficients for (10.16). Three simulations would be used to determine $a_2$ , $a_1$ and $a_0$ .The final four simulations would be needed to generate the two linear fits used to determine $\partial^2 \Delta K_i \big/ \partial \varepsilon_i \partial \Delta \varepsilon_i$ and $\partial \Delta K_i / \partial \Delta \varepsilon_i$ . However by careful selection of the geometries used in simulations to generate the coefficients, the 7 total simulations required could be reduced by allowing the same simulation to be used in multiple curve fitting exercises. To cover the range of length variations the model is specified to cover $\left(\varepsilon_i = 0 \rightarrow 0.5\right)$, it is also important that the chosen simulations use geometries that create curve fits are able to cover the full range of $\varepsilon_i$ and $\Delta \varepsilon_i$ values present in this range.

To create coefficients for (10.5), the local permeability for three simulations are found. Each simulation uses the local permeability in a block with 2 elements in the model.

$$K_L^P(\varepsilon_i = 0, \Delta\varepsilon_i = 0) \tag{10.18}$$

$$K_L^P(\varepsilon_i = 0.2, \Delta\varepsilon_i = 0) \tag{10.19}$$

$$K_L^P(\varepsilon_i = 0.5, \Delta\varepsilon_i = 0) \tag{10.20}$$

These three simulations provide sufficient data to construct a graph similar to Figure 10-2 and use the method of least squares to produce a quadratic relationship that approximates the permeability across the desired range. Equation (10.19) uses an arbitrary value for the modelled length variation. However it is preferred that the value for the length variation is kept central to the length variation range so as to prevent bias towards a particular end of the length variation spectrum.

To make the second linear fit as shown in (10.8) and Figure 10-13 the assumption is made that (10.21) is equal to zero and the simulation conducted for the fit is (10.22).

$$\Delta K_L^P(\varepsilon_i = 0, \Delta\varepsilon_i = 0) = 0 \tag{10.21}$$

$$\Delta K_L^P(\varepsilon_i = 0, \Delta\varepsilon_i = -0.5) \tag{10.22}$$

Finally, the third linear fit can be conducted by using the results of (10.21) and (10.22) along with the assumption that (10.23) is equal to zero and the $K_L^P$ value for (10.24).

$$K_L^P(\varepsilon_i = 0.5, \Delta\varepsilon_i = 0) = 0 \tag{10.23}$$

$$\Delta K_L^P(\varepsilon_i = 0.5, \Delta\varepsilon_i = 0.5) \tag{10.24}$$

So with assumptions, 5 simulations needed to approximate the behaviour of permeability. If these assumptions are not made, then still only 5 simulations are required because the results from (10.18) and (10.20) can be used in (10.21) and (10.23). Using the data from Figure 10-2 and Table 10-4 the approximate coefficients for (10.15) are shown in Table 10-7. All simulations were conducted using geometries with the same pore size $(L_0)$ to maintain consistency.

*Table 10-7. Empirically determined constants for the modified permeability prediction Equation* (10.15)*. The relative error is found for the approximated coefficients compared to the values obtained using a full data spread.*

| Constant | Reference Value | Approximated Value | Relative Error |
|---|---|---|---|
| $a_0$ | 0.0195 | 0.0195 | 0.00% |
| $a_1$ | 0.0430 | 0.0429 | -0.23% |
| $a_2$ | 0.0223 | 0.02216 | -0.63% |
| $n$ | -0.01108 | -0.0116 | 4.69% |
| $d$ | 0.00682 | 0.00711 | 4.25% |

From the relative error, the difference between the reference values and approximated values are very minor for $a_0$ $a_1$ and $a_2$. However, there is a relative error of over 4% for the coefficients used in determining the impact of $\Delta\varepsilon_i$. To test the ability of the approximated values to accurately predict the local pressure and permeability for a geometry with variable length variation, additional simulations were conducted for geometries of a different pore size that where each block was given an individual length variation.

### 10.3.3 Stress testing of approximated coefficients.

To determine the ability of the approximated coefficients to accurately predict permeability of blocks, flow through two geometries were simulated. The geometries had variable length variations as described in Table 10-8 and Table 10-9. In addition, the unvaried pore size $(L_0)$ was changed to 0.3 mm (from 0.8 mm) to test how the predictive model coped with a different length scale than what has been used to establish the model. The predicted permeabilities using the approximated coefficients are shown in Table 10-8 and Table 10-9. The simulated values for permeability as well

as those found using the reference coefficients are found to provide context and allow conclusions to be made about that validity of using approximated coefficients.

*Table 10-8. Comparative study between simulated and predicted values for permeability for a 2 element geometry with an un-varied pore size of 0.3 mm and variable length variation*

| Block | 1 | 2 | 3 | 4 | 5 | 6 | 7 | 8 |
|---|---|---|---|---|---|---|---|---|
| | $(\varepsilon_i = 0)$ | $(\varepsilon_i = 0)$ | $(\varepsilon_i = 0)$ | $(\varepsilon_i = 0)$ | $(\varepsilon_i = 0.5)$ | $(\varepsilon_i = 0)$ | $(\varepsilon_i = 0)$ | $(\varepsilon_i = 0)$ |
| $K_L^S(m^2)$ | 1.79E-09 | 1.45E-09 | 4.68E-10 | 1.23E-09 | 4.67E-10 | 1.46E-09 | 1.77E-09 | 1.79E-09 |
| $K_{total}(m^2)$ | 1.76E-09 | 1.45E-09 | 4.37E-10 | 1.14E-09 | 4.37E-10 | 1.445E-09 | 1.76E-09 | 1.76E-09 |
| $\delta K_{total}(-)$ | -1.83% | -0.44% | -6.54% | -7.17% | -6.34% | -0.48% | -0.60% | -1.86% |
| $K_L^P(m^2)$ *Approx.* | 1.76E-09 | 1.44E-09 | 4.41E-10 | 1.12E-09 | 4.41E-10 | 1.44E-09 | 1.76E-09 | 1.76E-09 |
| $\delta K_L^P(-)$ *Approx.* | -1.83% | -1.34% | -5.67% | -9.29% | -5.48% | -1.38% | -0.60% | -1.86% |

*Table 10-9. Comparative study between simulated and predicted values for permeability for a 2 element geometry with an un-varied pore size of 0.3 mm and variable length variation*

| Block | 1 | 2 | 3 | 4 | 5 | 6 | 7 | 8 |
|---|---|---|---|---|---|---|---|---|
| | $(\varepsilon_i = 0)$ | $(\varepsilon_i = 0.1)$ | $(\varepsilon_i = 0.2)$ | $(\varepsilon_i = 0.3)$ | $(\varepsilon_i = 0.5)$ | $(\varepsilon_i = 0)$ | $(\varepsilon_i = 0)$ | $(\varepsilon_i = 0)$ |
| $K_L^S(m^2)$ | 1.730E-09 | 1.39E-09 | 1.07E-09 | 7.43E-10 | 4.15E-10 | 1.46E-09 | 1.76E-09 | 1.79E-09 |
| $K_{total}(m^2)$ | 1.69E-09 | 1.39E-09 | 1.06E-09 | 7.43E-10 | 4.02E-10 | 1.45E-09 | 1.76E-09 | 1.76E-09 |
| $\delta K_{total}(-)$ | -2.16% | -0.21% | -0.53% | 0.08% | -3.06% | -0.78% | -0.36% | -1.88% |
| $K_L^P(m^2)$ *Approx.* | 1.69E-09 | 1.39E-09 | 1.06E-09 | 7.43E-10 | 4.06E-10 | 1.44E-09 | 1.76E-09 | 1.76E-09 |
| $\delta K_L^P(-)$ *Approx.* | -2.31% | -0.15% | -0.41% | 0.13% | -2.28% | -1.68% | -0.36% | -1.88% |

From the data, the use approximated coefficients cause negligible change in relative error compared to the reference values for blocks where $\Delta\varepsilon_i = 0$ . The accuracy of permeability predictions suffer most for blocks that experience a large $\Delta\varepsilon_i$ . For the study in Table 10-8, Blocks 3, 4 and 5 experience the biggest change in predicted permeability when using the approximated values. The relative error for these blocks is high (between 5-10%), but it is noted that these block are experiencing the greatest length variation change across a block permitted by the scope of the model.

In a quirk of the coefficients and their determination, some of the predicted permeabilities in Table 10-9 experience an increase in accuracy. This is due to the length variations used in the block and/or neighbouring block being similar to those used to create the approximate coefficients in the predictive model. Comparing the behaviour of the predicted permeabilities between the two tables, it is apparent that small changes in length variation allow for more accurate permeability predictions than large. Compared to the reference values, approximated constants sacrifice a relatively small amount of error to reduce the required simulations and therefore computer time by a significant amount. To obtain a strong indication of the maximum accuracy of the model, a combined total of 50 simulations were used to predict $a_2$, $a_1$ and $a_0$ as well as $\partial^2 \Delta K_L^S / \partial \varepsilon_i \partial \Delta \varepsilon_i$ and $\partial \Delta K / \partial \Delta \varepsilon$. For a relatively small drop in accuracy compared to the reference values, the approximated constants only required 5 simulations which is a significant improvement. Unless the application requires higher accuracy, it is suggested that the approximated values are more than sufficient for use instead of the reference values. More development should be focused on improving the accuracy for geometries that experience large, sudden changes in length variation.

# 11 Future Work

*The following sections expand of potential development ideas for the project, including work that needs to be conducted to broaden the applicability of the model and the optimisation for the specific field of deformable porous media. Section 11.1 suggests the steps that could be taken that allows the empirical permeability prediction to be applicable to various geometries and flow regimes. Section 11.2 outlines the process required to apply the method to a point where it can be used in place of Fluid-Solid Interface (FSI) simulations for deformable porous media. This goal is the major focus of development and where most of the potential in the method lies. FSI simulations are computationally expensive, and if the simulations can be decoupled effective by implementing strain as a novel boundary condition then significant improvement on current simulation methods for deformable porous media can be made.*

## 11.1 Broaden Applicability

The model developed here focused specifically on unit cells based on simple Cartesian geometry made up of repeating 'blocks'. The reason for choosing these was that they are easily described using well-defined parameters and can be linearly related to the length variation. However, it could be very useful for the modelling of soils and other granular porous medias if a similar model could be established for flow around non-Cartesian geometries such as spheres, cylinders and ellipsoids. Spheres in particular have seen frequent use as a representative model for the shape and dimensions of particles in porous solids [5, 18, 35, 36]. Spheres are also used in many test chambers to assess permeability [29].

However, the modelling of sphere bed poses problems during simulation, as the mesh has difficulty resolving around point contacts between spheres as shown in Figure 11-1. One solution would be to flatten the contact point and allow surfaces to be in contact rather than a singular point.

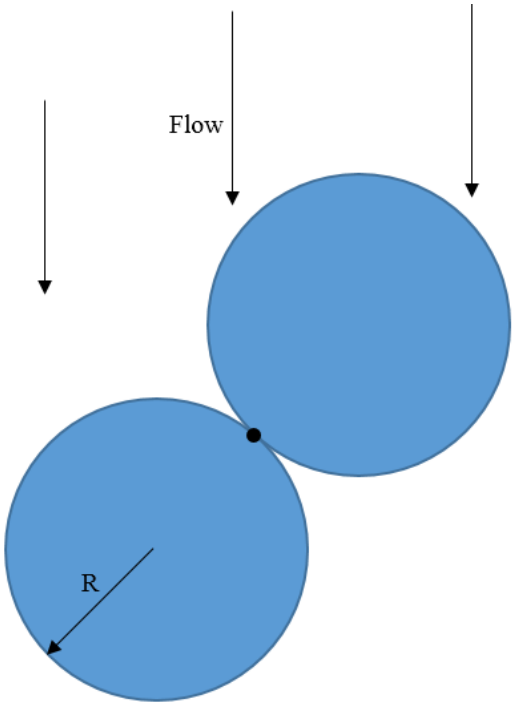


*Figure 11-1. Schematic representation of spheres immersed in fluid flow with point contact.*

A drawback of solving the problem in this manner would be that the geometry of the sphere could no longer be described by (11.1). Instead the flattened surface wouldn't allow the volume and surface areas of the modified spheres to be accurately described by the standard equations for the volume and surface areas of a sphere.

$$x^2 + y^2 + z^2 = r^2 \tag{11.1}$$

Another issue is that a sphere limits how length variation s can be expressed when the length variation is different between reference axes (i.e. the length variation in the z-direction is greater than the length variation in the x and y axes). Instead it may be beneficial to use ellipsoids, which allow for the dimensions of the ellipsoid to be altered for non-uniform changes in length variation between axes. The equation of an ellipsoid can be described as

$$\frac{x^2}{a^2} + \frac{y^2}{b^2} + \frac{z^2}{c^2} = 1 \tag{11.2}$$

Now $a$, $b$ and $c$ can be developed to be modified by a length variation. The use of ellipsoids also allow greater surface area to remain in contact between particles as well and should be less affected by the flattening of a contact surface. Another option for development of geometry is to use cylinders. These could particularly use for developing the method for modelling fluid flow through fibrous media and textiles as discussed in Section 12.1.

In addition to new unit cell geometries, another means of expanding the model applicability would be to investigate building the method to cope with additional channels. The current model only considers a single channel, but an investigation that determines how the model would scale with multiple or even a 2-D matrix of channels allows the model to predict the local pressure for highly ordered medias such as the media shown in Figure 11-2. Figure 11-2 was also the inspiration behind the 'block' and 'element' structure developed in Section 4.

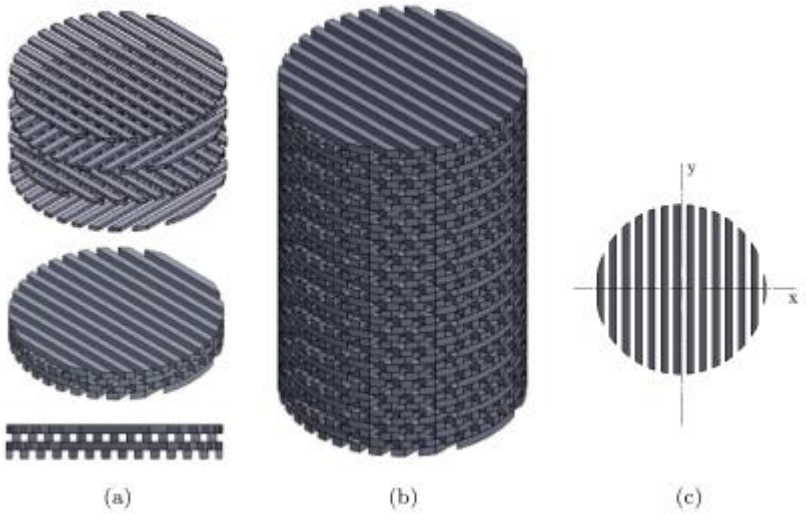


*Figure 11-2. 1.5 mm matrix (a) exploded, isometric and front view (b) full matrix (c) single unit layer. Extracted from [37].*

Finally, the Forcheimer regime has already been briefly discussed in Section 3.2.2. The Forcheimer equation is reiterated below.

$$\frac{dP}{dz} = \frac{\mu u}{K} + \beta \rho u^2 \tag{11.3}$$

Where $dP/dz$ is the pressure gradient, $\mu$ is the viscosity of the fluid, $K$ is the permeability, $\beta$ is the Forcheimer coefficient, $\rho$ is the fluid density, $u$ is the average fluid velocity. The first term in (11.3) is Darcy's law, which this study has already developed an empirical model for. The second term is also very simple with the Forcheimer coefficient linearly proportional to $dP/dz$. Simulation Data at $\mathrm{Re} > 1$ could potentially allow for the current permeability prediction model to be developed to be applicable in the Forcheimer regime, where inertial effects are no longer negligible. If the model be modified further to include the Forcheimer regime, then the prediction model becomes much more useful for studying metallic foams (Section 12.1). Metallic foams have a very well defined porous structure, with previous literature already using unit cell methods to model the repeating interior structure. Therefore making metallic foams a very suitable application for the method presented here.

## 11.2 Optimise for Deformable Porous Media

Another goal for future work is to bring the model to a point where it can accurately model the length deformable porous media in response to fluid flow. The work conducted here shows that for the geometry chosen, the length variation of a pore can be used to accurately predict local pressure. However the model needs refinement before it is applicable to deformable porous media and it's response to fluid flow. A major objective is to decouple the fluid and solid domains and remove the need for computationally expensive FSI simulations to examine deformable porous media response to fluid flow that permeates through the structure. The decoupling can be achieved by setting strain found through the empirical prediction as a boundary condition for the deformation of the solid. The strain can then be used as input to determine the deformation of the solid in response to fluid flow. The deformation then results in a new set of length variation s to be input back into the fluid side of the model. Being able to accurately predict local pressure is important as it is expected that the local pressure inside the pore causes a resistance to deformation that influences pore geometry and how it deforms under fluid flow.

The current model specifies the local pressure at the interface between two blocks in a geometry. To be able to determine how local pressure changes inside a block, investigation needs to be conducted on how local pressure drops across the interior of a block. The main focus is the functional relationship between pressure and location on the surface of the block. Depending on how the pressure changes along the length of the block, it may be possible to specify a linear drop in pressure across the block by using the two predicted values for pressure on either end of the block. If the pressure drop cannot be approximated accurately with a linear function, then determine the pressure acting on the surface between the fluid and the solid becomes more challenging.

The main motivation to determine the behaviour of fluid pressure acting on a block is to accurately model how the solid deforms along its length in response to a decreasing local fluid pressure. The deformation can then be combined with the length variation that is a result of driving pressure flow acting on the top surface of the block as shown in Figure 11-3.

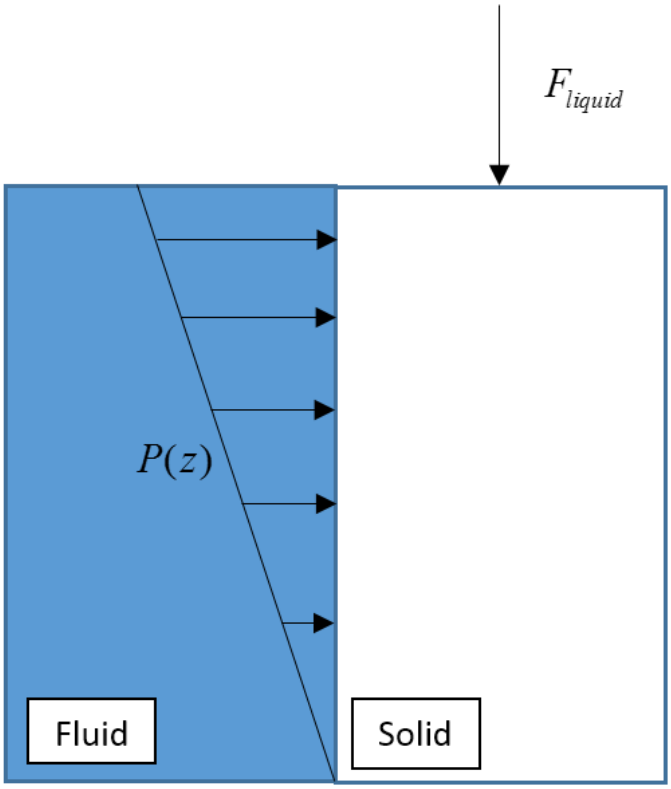


*Figure 11-3. Force Body Diagram of forces due to fluid flow acting on impermeable solid*

The current model does not consider this additional source of length variation , and importantly how it will partially negate the transverse length variation as a result of The variation ratio ( $\varepsilon_x$ and $\varepsilon_y$ ). If the pressure behaviour across the block can be determined, then the strain experienced by the block in response to fluid flow can be determined.

The calculated strain can then be utilised as a boundary condition for solid length deformation to decouple the fluid solid interaction. Instead of running computationally expensive FSI simulations, a new method for simulating the flow through deformable porous media can be established. A simulation on the fluid side for flow through a channel can be conducted and then input into an empirical model that determines the deformation it causes for a specified solid. The deformation response can then be input back into a fluid flow simulation by altering the geometry as required to match the length variation that was calculated previously. The cycle continues until a point of equilibrium between the solid and the fluid is reached for a given global pressure drop across the media. Once the method has been completed, it can be compared to FSI simulations and physical experiments to examine accuracy and applicability.

# 12 Applications

*Some additional research was conducted into potential applications of the empirical prediction equations and how they can be applied to physical problems in current literature. A selection of identified applications are organised into two sections. Section 12.1 details the porous media and deformable porous media applications for this technique. Particularly as a means to calculate pressures internal to media easily for multiple different cases. Section 12.2 lists some of the potential applications in microfluidics, where microscale channels are also used to control flow in the Darcy regime for a number of different applications including size-based particle separation and heat exchangers. The methods developed here will need continued development before they are capable with respect to useful application, but the literature listed offers some long term targets for development.*

## 12.1 Porous Media

Previous work on flow through geological porous medias created a model for flow through the soils based on Darcian inter-block conductivity [38]. In a similar manner to the work conducted here, the conductivity was based on Darcy's Law, using permeability as a measure of fluid flow conductivity. Using a model based on mass conversation, the method was found to reduce the inflow prediction error by 3.84-8.84 times. Another study developed Biot's fundamental research relating strain and flow [39-42] and applied to Aquifer mechanics [43].

A more recent development is the use of deformable porous media as a tool for measuring and simulating strain and its relation to flow inside modern, multi-component materials such as aerogels[44], biological materials including interstitial fluid through bone[8] and various fibre based textiles and fibre-polymer composites. Bone is a porous material with a hierarchical pore architecture. Previous studies have developed the governing equations for bones and its compressible components as they undergo small length variations. The result relates cyclic loading and the movement of fluid from one pore hierarchy to another and is essential to understanding the movement of fluid and therefore the distribution of nutrients through bones. If applicable, the pressure prediction method presented allows an alternative solution to examining flow characteristics in bone and allow for a simpler approach that takes into account the intricate structure. There are multiple applications for a model that predicts local pressure in the manufacture and processing of fibre laminates and textiles. For example, the infusion process for fibre-polymer composites[35], predicting permeability for fluid flow through matted fibres [45] and developing flow models for complex composite laminates [46]. Of particular interest is [45], where the permeability of paper fibres were experimentally assessed under mechanical compression using both water and air as the permeating fluid. The model developed here would be very well suited to such applications, especially for textiles that have an organised fibre

structure that allows a geometrical unit cell to be developed that represents the geometry. Extensive development of the current pressure prediction model needs to occur to become specifically applicable to the applications mentioned above. However the examples listed here and in Section 12.2 provide examples for some of the practical applications and some of the long term goals for continued development.

## 12.2 Microfluidics

Microfluidic devices and channels such as those found in heat exchangers, 'lab-on-a-chip' devices and fuel cells provide simpler geometries and applications that provide shorter term applications for the local pressure prediction model. The channels and features of microfluidic devices are often geometrically simple and their geometrical parameters can be easily defined [22, 23, 28]. The empirical method provides an alternative solution to analytical methods for determining the pressure drop through channels that are serpentine, change size or other undergo other changes in geometry. One example of where this method could be of use include microfluidic analogues for porous mediums [47]. The microfluidic analogue consists of a uni-directional channel composed of a series of contractions and expansions and the authors state the benefits of such models include the selection of a fluid to be used for a specific porous medium. The model presented here could be predictably applied to such a system, using length variation to simulate the contractions and expansions. It could allow for fluid properties to be tested for a wide range of geometries without requiring multiple simulations or the construction of multiple experimental geometries. Another example for potential applications in microfluidics is local pressure calculation for microfluidic devices such as a size-based separation device as described in [48]. Such a device combines a series of contractions and expansion to separate particles utilizing inertial forces generated by the geometry to separate out particles in the fluid based on their respective mass. Again, the method developed allows for many different geometry configurations to be iterated through without requiring repeated simulations or multiple experimental apparatus to determine pressure and flow rate for the geometry. There is large potential for shape optimization in general with regards to channel design and optimization for heat exchangers, fuel cells, and other commercial uses for micro channels [49].

# 13 Conclusion

This thesis provides a method for the prediction of Darcian flow characteristics through porous media that is non-homogeneous in the direction of bulk fluid flow. The model uses a non-dimensional relationship between the fluid flow and the media geometry, using the permeability of the geometries studied as a means of predicting the resistance to fluid flow. The developed model then uses this relationship to predict local and global flow behaviour. Over two case studies, the model has been shown to successfully predict the local pressure drop and the bulk fluid flow rate for complex geometries. Models produced in this thesis require prior knowledge of the geometric parameters and fluid properties along with the total pressure drop to successfully predict the flow characteristics for the non-homogeneous porous media studied. Two case studies were used in this thesis to build the predictive method. The first case study focused on a geometry that maintained a constant porosity, but varied the characteristic length along the direction of bulk fluid flow; the second case study focused on a geometry with variable porosity and characteristic length in the direction of bulk fluid flow.

The geometry developed was based on a tortuous Cartesian porous media. The media was chosen so that the pores within the media could be described in terms of the pore lengths parallel and perpendicular to fluid flow. In this thesis a pore was termed a 'block' which was the geometric unit that represents the fluid-filled space between the layers of the porous media. The 'blocks' were arranged in quasi-repeating units called 'elements' that were composed of four 'blocks' orientated to provide a fluid path that maintained a constant tortuosity throughout the media. Through an introduced parameter called the 'length variation' $(\varepsilon)$, the length in the direction of fluid flow for each 'block' was controlled and non-homogeneity was introduced. To change the porosity along the direction of bulk fluid flow, a 'variation ratio' $(\nu)$ was also introduced to relate the length variation parallel to the direction of fluid flow to the length variation perpendicular to fluid flow.

The dimensional analysis was conducted by using the commercial software COMSOL™ Multiphysics to determine the relationship between pore geometry and permeability. To build the non-dimensional model, flow simulations were conducted systematically through geometries with characteristic lengths ranging from $0.2mm$ to $1.0mm$ and length variations ranging from $0$ to $0.5$. Higher variations in length were not investigated in this thesis as their relationship to permeability could no longer be predicted accurately. The final non-dimensional equation for the first case study relating permeability to fluid flow is given in Equation (13.1) and accurately predicts permeability with a maximum error of 2.5% within the scope of the study. The accuracy of the predicted permeability was shown to not be affected if the variation in length was different for each block in the direction of bulk fluid flow.

The simulations in the first case study focused on geometries that varied in length scale in the direction of bulk fluid flow, but without variation in porosity. The first case study showed that for the geometry studied here that permeability scales with the squared characteristic length $\left(K \propto L_0^{\,2}\right)$ in agreement with literature. It was also shown that the frictional effects were linear with pressure gradient and that inertial effects were negligible.

$$\left(K^P = (C_0 - C_\varepsilon \cdot \varepsilon) L_0^{\,2}\right) \tag{13.1}$$

The predicted permeability could be input into a step wise equation (13.3) that uses the inlet pressure to predict pressure and flow rate through the media as shown with $p_i$ being the local pressure at the interface between each 'block' in the geometry. Flow rate (13.2) was predicted with a maximum error of 0.4% and the local pressure was predicted with a maximum error of 2 Pa when the total pressure drop across the geometry was 1000 Pa.

$$Q_G^P = \frac{\Delta p}{\mu}\frac{1}{R} \text{ where R is defined by } R = \frac{\Delta L}{K^P \cdot A} \tag{13.2}$$

$$p_i = p_{i-1} - Q_G^P \cdot \mu \cdot \sum_{i=1}^{n} \frac{L_i}{K_i \cdot A_i} \tag{13.3}$$

The second case study conducted flow simulations through a geometry whose characteristic length and porosity varied in the direction of bulk fluid flow. It was shown that the permeability as a function of the 'length variation' $(\varepsilon)$ could be predicted accurately using a polynomial relationship for a geometry where the characteristic length of each block was reduced equally. However, if the characteristic length of each block was not varied homogeneously along the direction of bulk fluid flow, the resulting non-homogeneous variation in porosity meant that the minor losses that occurred as a result of expansion and contraction of the cross-sectional area that produced minor losses which could no longer be accounted for as part of the permeability prediction. The change in porosity was shown to be dependent on the change in 'length variation' $(\Delta\varepsilon)$ between neighbouring 'blocks'. Additional flow simulations were carried out to determine a non-dimensional approximation of the change in permeability as a function of the 'length variation' for the minor losses. The final non-dimension relationship between permeability and pore geometry is presented in Equation (13.4) which was able to predict permeability for highly complex non-homogeneous geometries with a maximum error of 7.17% for the most extreme case studied. Equations (13.2) and (13.3) used for determining the flow rate and local pressure developed in the first case study remain applicable here. To determine the numerical values for the constants in the permeability prediction model, the minimum number of simulations required was shown to be five.

$$K_T^L = \left(a_2\varepsilon^2 - a_1\varepsilon + a_0 + \Delta\varepsilon(\mathrm{b}_1 \cdot \varepsilon \cdot + b_0)\right) {L_0}^2 \tag{13.4}$$

The next steps required to further develop the outcomes of this thesis is to extend the method to describe the flow characteristics for a matrix of elements that can be used to describe a non-homogeneous porous media with multiple flow paths and confirm that the non-dimensional model holds for higher order geometries. In addition, the applicability and scope of the method presented could be applied to Forcheimer flow cases, where inertial effects are taken into account. Another suggested option is to investigate different pore structures and geometries to develop non-dimensional flow descriptions through porous matrices that are non-Cartesian such as spheres or cylinders. The model can also be used for deformable porous media applications, with the potential to use the local pressure predictions as a tool to decouple fluid-solid interface simulations. Simulated local pressures predicted for the fluid phase could be used as boundary conditions for the deformation of the solid phase. The 'length variation' of the deformed solid could be returned to the fluid domain to provide boundary conditions in the determination of the change in fluid flow as a result of the deformation. Some current applications for the method in its current state include prediction of fluid flow through various non-homogenous materials and porous medias including biological materials, fibrous materials, paper and geological soils. The method could also be purposed for systematic prediction and analysis of flow characteristics through micro channels for use in microfluidics studies, which has an enormous range of application.

# 14 Bibliography


1. Whitaker, S., *The Forchheimer Equation: A Theoretical Development.* Transport in Porous Media, 1996. **25**: p. 27-61.
2. Various, *Heat transfer and pressure drop in empty, baffled, and packed tubes.* Industrial and Engineering Chemistry, 1931. **23**(8): p. 910-923.
3. Andrade Jr., J.S., et al., *Inertial Effects on Fluid Flow through disordered porous media.* Physical Review Letters, 1999. **82**(26).
4. Steinke, M.E. and S.G. Kandlikar, *Single-phase liquid friction factors in microchannels.* International Journal of Thermal Sciences, 2006. **45**(11): p. 1073-1083.
5. Markert, B., *A constitutive approach to 3-d nonlinear fluid flow through finite deformable porous continua.* Transport in Porous Media, 2007. **70**(3): p. 427-450.
6. du Plessis, J.P. and S. Woudberg, *Pore-scale derivation of the Ergun equation to enhance its adaptability and generalization.* Chemical Engineering Science, 2008. **63**(9): p. 2576-2586.
7. Nield, D.A. and A. Bejan, *Convection in Porous Media*. Third ed. 2006, USA: Springer. 640.
8. Cowin, S.C., G. Gailani, and M. Benalla, *Hierarchical poroelasticity: movement of interstitial fluid between porosity levels in bones.* Philosophical Transactions of the Royal Society A: Mathematical, Physical and Engineering Sciences, 2009. **367**(1902): p. 3401-3444.
9. S., S.H. and G.V. Chilingarian, *Influence of Porosity and Direction of Flow on Tortuosity in Unconsolidated Porous Media.* Energy Sources, 2000. **22**: p. 207-213.
10. Yang, X., T.J. Lu, and T. Kim, *An analytical model for permeability of isotropic porous media.* Physics Letters, Section A: General, Atomic and Solid State Physics, 2014. **378**(30-31): p. 2308-2311.
11. Dukhan, N. and K. Patel, *Effect of sample's length on flow properties of open-cell metal foam and pressure-drop correlations.* Journal of Porous Materials, 2011. **18**(6): p. 655-665.
12. Despois, J.F. and A. Mortensen, *Permeability of open-pore microcellular materials.* Acta Materialia, 2005. **53**(5): p. 1381-1388.
13. Bear, J., *Dynamics of Fluids in Porous Media*. 1972, Amsterdam, The Netherlands: Elsevier.
14. Vervoort, R.W. and C. S.R., *Linking hydraulic conductivity and tortuosity parameters to pore space geometry and pore-size distribution.* Journal of Hydrology, 2003. **272**: p. 36-49.
15. Barrande, M., R. Bouchet, and R. Denoyel, *Toruosity of Porous Particles.* Analytical Chemistry, 2007. **79**(23): p. 9115-9121.

16. Zeng, Z. and R. Grigg, *A Criterion for Non-Darcy Flow in Porous Media.* Transport in Porous Media, 2006. **63**: p. 57-69.

17. H., D., *Les Fontaines Publiques de la Ville de Dijon*. 1856, Paris: Dalmont.

18. Dullien, F.A.L., *Porous Media (Second Edition)*. Second ed. 1992, San Diego: Academic Press.

19. Beavers, G.S., K. Wittenberg, and E.M. Sparrow, *FLUID FLOW THROUGH A CLASS OF HIGHLY-DEFORMABLE POROUS MEDIA - 2. EXPERIMENTS WITH WATER.* Journal of Fluids Engineering, Transactions of the ASME, 1981. **103**(3): p. 440-444.

20. Beavers, G.S., A. Hajji, and E.M. Sparrow, *FLUID FLOW THROUGH A CLASS OF HIGHLY-DEFORMABLE POROUS MEDIA - 1. EXPERIMENTS WITH AIR.* Journal of Fluids Engineering, Transactions of the ASME, 1981. **103**(3): p. 432-439.

21. Renqiang, X. and J.N. Chung, *Flow characteristics of water in straight and serpentine micro-channels with miter bends.* Experimental Thermal and Fluid Science, 2006. **31**: p. 805-812.

22. Maharudrayya, S., S. Jayanti, and A.P. Deshpande, *Pressure losses in laminar flow through serpentine channels in fuel cell stacks.* Journal of Power Sources, 2004. **1**(13): p. 13.

23. Shiragami, N. and I. Inoue, *Pressure Losses in Square Section Bends.* Journal of Chemical Engineering of Japan, 1981. **14**(3): p. 173-177.

24. White, F.M., *Fluid Mechanics*. Sixth Edition ed. McGraw-Hill Series in Mechanical Engineering. 2008, New York, USA: McGraw-Hill.

25. Baviere, R., et al., *Experimental characterization of water flow through smooth rectangular microchannels.* Physics of Fluids, 2005. **17**(9): p. 1-4.

26. Judy, J., D. Maynes, and B.W. Webb, *Characterization of frictional pressure drop for liquid flows through microchannels.* International Journal of Heat and Mass Transfer, 2002. **45**(17): p. 3477-3489.

27. Koo, J. and C. Kleinstreuer, *Liquid flow in microchannels: Experimental observations and computational analyses of microfluidics effects.* Journal of Micromechanics and Microengineering, 2003. **13**(5): p. 568-579.

28. Pfund, D., et al. *Pressure drop measurements in a microchannel*. in *Proceedings of the 1998 ASME International Mechanical Engineering Congress and Exposition, November 15, 1998 - November 20, 1998*. 1998. Anaheim, CA, USA: ASME.

29. Whitaker, S., *FLOW IN POROUS MEDIA III: DEFORMABLE MEDIA.* Transport in Porous Media, 1986. **1**(2): p. 127-154.

30. Bear, J., Y. Bachmat, and F.M. Tiller, *Introduction to modeling of transport phenomena in porous media.* Applied Mechanics Reviews, 1991. **44**(1): p. B22-B22.

31. Munro, B., et al., *Fabrication and Characterization of Deformable Porous Matrices with Controlled Pore Characteristics.* Transport in Porous Media, 2015. **107**(1): p. 79-94.

32. Philpot, T.A., *Mechanics of Materials*. 2nd ed. ed. 2010, USA: John Wiley & Sons Inc.

33. Legendre, A.-M., *Nouvelles méthodes pour la détermination des orbites des comètes [New Methods for the Determination of the Orbits of Comets]*. 1805, Paris, France: F. Didot.

34. Marquardt, D.W., *An Algorithm for Least-Squares Estimation of Nonlinear Parameters.* Journal of the Society for Industrial and Applied Mathematics, 1963. **11**(2): p. 431-441.

35. Lopatnikov, S., et al., *A closed form solution to describe infusion of resin under vacuum in deformable fibrous porous media*. Modelling and Simulation in Materials Science and Engineering, 2004. **12**: p. 191-204.

36. Bryant, S.L., P.R. King, and D.W. Mellor, *Network Model Evaluation of Permeability and Spatial Correlation in a Real Random Sphere Packing.* Transport in Porous Media, 1992. **11**: p. 53-70.

37. Munro, B., et al., *Fabrication and Characterization of Deformable Porous Matrices with Controlled Pore Characteristics*. 2014, University of Canterbury.

38. Baker, D.L., *Darcian weighted interblock conductivity means for vertical unsaturated flow.* Ground Water, 1995. **33**(3): p. 385-390.

39. Biot, M.A. and F.M. Clingan, *Consolidation settlement of soil with impervious top surface.* Journal of Applied Physics, 1941. **12**(7): p. 578-581.

40. Biot, M.A., *General Solutions of the Equations of Elasticity and Consolidation for a Porous Material.* Journal of Applied Mechanics, 1956: p. 92-96.

41. Biot, M.A., *General theory of three-dimensional consolidation.* Journal of Applied Physics, 1941. **12**(2): p. 155-164.

42. Biot, M.A., *Theory of elasticity and consolidation for porous anisotropic solid.* Journal of Applied Physics, 1955. **26**(2): p. 182-185.

43. Helm, D.C. *Understanding Darcian flow leads to understanding aquifer mechanics*. in *International Symposium and 9th Asian Regional Conference of IAEG "Global View of Engineering Geology and the Environment", September 24, 2013 - September 25, 2013*. 2013. Beijing, China: Taylor & Francis - Balkema.

44. Gross, J. and G.W. Scherer, *Dynamic pressurization: Novel method for measuring fluid permeability.* Journal of Non-Crystalline Solids, 2003. **325**(1-3): p. 34-47.

45. Koivu, V., K. Mattila, and M. Kataja, *A method for measuring Darcian flow permeability of thin compressed fibre mats.* Nordic Pulp and Paper Research Journal, 2009. **24**(4): p. 395-402.

46. Hubert, P., R. Vaziri, and A. Poursartip, *A two-dimensional flow model for the process simulation of complex shape composite laminates.* International Journal for Numerical Methods in Engineering, 1999. **44**(1): p. 1-26.

47. Galindo-Rosales, F.J., et al., *Microfluidic systems for the analysis of viscoelastic fluid flow phenomena in porous media*. Microfluidics and Nanofluidics, 2012. **12**(1-4): p. 485-498.

48. Park, J.-S. and H.-I. Jung, *Multiorifice Flow Fractionation: Continuous Size-based Separation of Microspheres using a Series of Contraction/Expansion Microchannels.* 2009.

49. Lee, S.-M. and K.-Y. Kim, *Optimization of zigzag flow channels of a printed circuit heat exchanger for nuclear power plant application.* Journal of Nuclear Science and Technology, 2012. **49**(3): p. 343-351.

# Appendix A: Case Study 1 Raw Data

Pore Size vs. Permeability

*Table 0-1. Correlation coefficient data for constant porosity case study*

| **Pore Length** | **Pore Length$^2$** | **Linear Term** | **Off-set** | **Normalised Linear Term** | **Normalised off-set** | **Reynolds** |
|---|---|---|---|---|---|---|
| $L_0(mm)$ | $L_0{}^2(mm^2)$ | $C_e(mm)$ | $C_0(mm^2)$ | $C_e/L_0{}^2(mm^{-1})$ | $C_0/L_0{}^2(-)$ | Re(–) |
| 0.2 | 0.04 | 1.10E-09 | 7.89E-10 | 0.027608 | 0.019714 | 0.0097 |
| 0.4 | 0.16 | 4.42E-09 | 3.16E-09 | 0.027636 | 0.019723 | 0.039 |
| 0.6 | 0.36 | 9.96E-09 | 7.11E-09 | 0.027665 | 0.019741 | 0.088 |
| 0.8 | 0.64 | 1.77E-08 | 1.26E-08 | 0.027661 | 0.019733 | 0.16 |
| 1.0 | 1.0 | 2.77E-08 | 1.97E-08 | 0.027654 | 0.019739 | 0.24 |

Data table for Predicted and simulated permeability along channel with variable pore sizes

*Table 0-2. Simulation data for 4 element geometry with a non-homogeneous deformation along the direction of bulk fluid flow*

| **Variation Ratio** | **Simulated Local Permeability** | **Location** | **Predicted Local Permeability** | **Local Error** | **Global Error** | **Resistance** |
|---|---|---|---|---|---|---|
| $\varepsilon(-)$ | $K_L^S(m^2)$ | $z$(mm) | $K_L^P(m^2)$ | | | $\Delta R_i$ |
| 0 | 9.72E-09 | 0.5 | 9.9E-09 | -1.80% | -1.77% | 2.02E+11 |
| 0 | 1E-08 | 1 | 9.9E-09 | 1.15% | 1.17% | 2.02E+11 |
| 0 | 9.93E-09 | 1.5 | 9.9E-09 | 0.27% | 0.27% | 2.02E+11 |
| 0 | 9.92E-09 | 2 | 9.9E-09 | 0.24% | 0.24% | 2.02E+11 |
| 0.15 | 7.89E-09 | 0.425 | 7.84E-09 | 0.68% | 0.12% | 2.17E+11 |
| 0.15 | 8.07E-09 | 0.85 | 7.84E-09 | 2.78% | 2.27% | 2.17E+11 |
| 0.15 | 8.07E-09 | 1.275 | 7.84E-09 | 2.89% | 2.39% | 2.17E+11 |
| 0.15 | 7.94E-09 | 1.7 | 7.84E-09 | 1.27% | 0.71% | 2.17E+11 |
| 0.3 | 5.83E-09 | 0.35 | 5.78E-09 | 0.86% | 0.09% | 2.42E+11 |
| 0.3 | 5.87E-09 | 0.7 | 5.78E-09 | 1.49% | 0.73% | 2.42E+11 |
| 0.3 | 5.79E-09 | 1.05 | 5.78E-09 | 0.09% | -0.68% | 2.42E+11 |
| 0.3 | 5.95E-09 | 1.4 | 5.78E-09 | 2.85% | 2.14% | 2.42E+11 |
| 0.35 | 5.12E-09 | 0.325 | 5.10E-09 | 0.39% | -0.49% | 2.55E+11 |
| 0.35 | 5.22E-09 | 0.65 | 5.10E-09 | 2.44% | 1.60% | 2.55E+11 |
| 0.35 | 5.14E-09 | 0.975 | 5.10E-09 | 0.76% | -0.12% | 2.55E+11 |
| 0.35 | 5.11E-09 | 1.3 | 5.10E-09 | 0.34% | -0.54% | 2.55E+11 |

*Table 0-3. Simulation data as a result of length deformation where the undeformed pore length is 0.2mm*

| Variation Ratio $\varepsilon(-)$ | Local Pressure $P_5(Pa)$ | Local Pressure $P_6(Pa)$ | Block Length $L_z(mm)$ | Simulated Local Permeability $K_L^S(m^2)$ | Area $A(m^2)$ | Flow Rate $Q(m^3s^{-1})$ | Reynolds Re(−) |
|---|---|---|---|---|---|---|---|
| 0 | 500.14 | 375.25 | 0.2 | 7.79E-10 | 2E-08 | 9.73E-11 | 0.0097 |
| 0.1 | 500.01 | 375.27 | 0.18 | 6.83E-10 | 2E-08 | 9.46E-11 | 0.0085 |
| 0.2 | 499.97 | 375.05 | 0.16 | 5.75E-10 | 2E-08 | 8.98E-11 | 0.0072 |
| 0.3 | 500.30 | 375.67 | 0.14 | 4.62E-10 | 2E-08 | 8.22E-11 | 0.0058 |
| 0.4 | 499.85 | 375.32 | 0.12 | 3.45E-10 | 2E-08 | 7.15E-11 | 0.0043 |
| 0.5 | 500.00 | 375.50 | 0.1 | 2.31E-10 | 2E-08 | 5.76E-11 | 0.0029 |

*Table 0-4. Simulation data as a result of length deformation where the undeformed pore length is 0.4mm*

| **Variation Ratio** $\varepsilon(-)$ | **Local Pressure** $P_5(Pa)$ | **Local Pressure** $P_6(Pa)$ | **Block Length** $L_z(mm)$ | **Simulated Local Permeability** $K_L^S(m^2)$ | **Area** $A(m^2)$ | **Flow Rate** $Q(m^3s^{-1})$ | **Reynolds** Re(−) |
|---|---|---|---|---|---|---|---|
| 0 | 499.98 | 375.14 | 0.40 | 3.12E-09 | 1.6E-07 | 7.79E-10 | 0.039 |
| 0.1 | 499.828 | 375.00 | 0.36 | 2.73E-09 | 1.6E-07 | 7.57E-10 | 0.034 |
| 0.2 | 499.948 | 375.03 | 0.32 | 2.30E-09 | 1.6E-07 | 7.19E-10 | 0.029 |
| 0.3 | 500.278 | 375.64 | 0.28 | 1.85E-09 | 1.6E-07 | 6.58E-10 | 0.023 |
| 0.4 | 499.838 | 375.30 | 0.24 | 1.38E-09 | 1.6E-07 | 5.72E-10 | 0.017 |
| 0.5 | 499.99 | 375.48 | 0.20 | 9.25E-10 | 1.6E-07 | 4.61E-10 | 0.012 |

*Table 0-5. Simulation data as a result of length deformation where the undeformed pore length is 0.6 mm*

| **Variation Ratio** $\varepsilon(-)$ | **Local Pressure** $P_5(Pa)$ | **Local Pressure** $P_6(Pa)$ | **Block Length** $L_z(mm)$ | **Simulated Local Permeability** $K_L^S(m^2)$ | **Area** $A(m^2)$ | **Flow Rate** $Q(m^3s^{-1})$ | **Reynolds** Re(−) |
|---|---|---|---|---|---|---|---|
| 0 | 499.74 | 375.10 | 0.60 | 7.02E-09 | 1.8E-07 | 2.63E-09 | 0.086 |
| 0.1 | 500.07 | 375.28 | 0.54 | 6.14E-09 | 1.8E-07 | 2.56E-09 | 0.077 |
| 0.2 | 499.96 | 375.45 | 0.48 | 5.19E-09 | 1.8E-07 | 2.42E-09 | 0.065 |
| 0.3 | 499.97 | 375.32 | 0.42 | 4.16E-09 | 1.8E-07 | 2.22E-09 | 0.052 |
| 0.4 | 500.01 | 375.47 | 0.36 | 3.10E-09 | 1.8E-07 | 1.93E-09 | 0.039 |
| 0.5 | 499.80 | 375.20 | 0.30 | 2.08E-09 | 1.8E-07 | 1.56E-09 | 0.026 |

*Table 0-6. Simulation data as a result of length deformation where the undeformed pore length is 0.8mm*

| **Variation Ratio** $\varepsilon(-)$ | **Local Pressure** $P_5(Pa)$ | **Local Pressure** $P_6(Pa)$ | **Block Length** $L_z(mm)$ | **Simulated Local Permeability** $K_L^S(m^2)$ | **Area** $A(m^2)$ | **Flow Rate** $Q(m^3s^{-1})$ | **Reynolds** Re(−) |
|---|---|---|---|---|---|---|---|
| 0 | 499.99 | 375.26 | 0.80 | 1.25E-08 | 3.2E-07 | 6.23E-09 | 0.16 |
| 0.1 | 499.80 | 375.13 | 0.72 | 1.09E-08 | 3.2E-07 | 6.06E-09 | 0.14 |
| 0.2 | 499.85 | 374.93 | 0.64 | 9.20E-09 | 3.2E-07 | 5.75E-09 | 0.11 |
| 0.3 | 500.18 | 375.55 | 0.56 | 7.39E-09 | 3.2E-07 | 5.26E-09 | 0.092 |
| 0.4 | 499.75 | 375.22 | 0.48 | 5.51E-09 | 3.2E-07 | 4.58E-09 | 0.069 |
| 0.5 | 499.94 | 375.43 | 0.40 | 3.70E-09 | 3.2E-07 | 3.69E-09 | 0.046 |

*Table 0-7. Simulation data as a result of length deformation where the undeformed pore length is 1.0 mm*

| **Variation Ratio** $\varepsilon(-)$ | **Local Pressure** $P_5(Pa)$ | **Local Pressure** $P_6(Pa)$ | **Block Length** $L_z(mm)$ | **Simulated Local Permeability** $K_L^S(m^2)$ | **Area** $A(m^2)$ | **Flow Rate** $Q(m^3s^{-1})$ | **Reynolds** Re(−) |
|---|---|---|---|---|---|---|---|
| 0 | 499.93 | 375.23 | 1.00 | 1.95E-08 | 5.0E-07 | 1.22E-08 | 0.24 |
| 0.1 | 499.55 | 374.96 | 0.90 | 1.71E-08 | 5.0E-07 | 1.18E-08 | 0.21 |
| 0.2 | 499.51 | 374.97 | 0.80 | 1.44E-08 | 5.0E-07 | 1.12E-08 | 0.18 |
| 0.3 | 499.49 | 374.90 | 0.70 | 1.16E-08 | 5.0E-07 | 1.03E-08 | 0.14 |
| 0.4 | 499.49 | 374.99 | 0.60 | 8.62E-09 | 5.0E-07 | 8.94E-09 | 0.11 |
| 0.5 | 499.57 | 375.18 | 0.50 | 5.79E-09 | 5.0E-07 | 7.20E-09 | 0.072 |

# Appendix B: Case Study 2 Raw Data

*Table 0-1. Simulation data as a result of length deformation where the undeformed pore length is 0.2 mm*

| Variation Ratio | Local Pressure | Local Pressure | Block Length | Simulated Local Permeability | Area | Flow Rate | Reynolds |
|---|---|---|---|---|---|---|---|
| $\varepsilon(-)$ | $P_5(Pa)$ | $P_6(Pa)$ | $L_z(mm)$ | $K_L^S(m^2)$ | $A(m^2)$ | $Q(m^3s^{-1})$ | Re(−) |
| 0 | 500.14 | 375.26 | 0.20 | 7.79E-10 | 2.0E-08 | 9.73E-11 | 0.009728 |
| 0.1 | 499.85 | 375.06 | 0.18 | 6.18E-10 | 1.92E-08 | 8.23E-11 | 0.007717 |
| 0.2 | 499.90 | 375.00 | 0.16 | 4.72E-10 | 1.84E-08 | 6.78E-11 | 0.0059 |
| 0.3 | 499.95 | 375.67 | 0.14 | 3.45E-10 | 1.76E-08 | 5.39E-11 | 0.004288 |
| 0.4 | 499.75 | 375.54 | 0.12 | 2.35E-10 | 1.68E-08 | 4.08E-11 | 0.002913 |
| 0.5 | 500.43 | 376.26 | 0.10 | 1.44E-10 | 1.6E-08 | 2.86E-11 | 0.001785 |

*Table 0-2.Simulation data as a result of length deformation where the undeformed pore length is 0.4 mm*

| Variation Ratio | Local Pressure | Local Pressure | Block Length | Simulated Local Permeability | Area | Flow Rate | Reynolds |
|---|---|---|---|---|---|---|---|
| $\varepsilon(-)$ | $P_5(Pa)$ | $P_6(Pa)$ | $L_z(mm)$ | $K_L^S(m^2)$ | $A(m^2)$ | $Q(m^3s^{-1})$ | Re(−) |
| 0 | 499.98 | 375.14 | 0.40 | 3.12E-09 | 8.0E-08 | 7.79E-10 | 0.039 |
| 0.1 | 500.04 | 375.37 | 0.36 | 2.47E-09 | 7.68E-08 | 6.58E-10 | 0.031 |
| 0.2 | 499.88 | 374.98 | 0.32 | 1.89E-09 | 7.36E-08 | 5.43E-10 | 0.0249 |
| 0.3 | 499.93 | 375.65 | 0.28 | 1.38E-09 | 7.04E-08 | 4.31E-10 | 0.017 |
| 0.4 | 499.73 | 375.52 | 0.24 | 9.38E-10 | 6.72E-08 | 3.26E-10 | 0.012 |
| 0.5 | 500.41 | 376.25 | 0.20 | 5.75E-10 | 6.4E-08 | 2.28E-10 | 0.0071 |

*Table 0-3. Simulation data as a result of length deformation where the undeformed pore length is 0.6 mm*

| Variation Ratio | Local Pressure | Local Pressure | Block Length | Simulated Local Permeability | Area | Flow Rate | Reynolds |
|---|---|---|---|---|---|---|---|
| $\varepsilon(-)$ | $P_5(Pa)$ | $P_6(Pa)$ | $L_z(mm)$ | $K_L^S(m^2)$ | $A(m^2)$ | $Q(m^3s^{-1})$ | Re(−) |
| 0 | 499.74 | 375.095 | 0.60 | 7.02E-09 | 1.8E-07 | 2.63E-09 | 0.088 |
| 0.1 | 499.91 | 375.32 | 0.54 | 5.57E-09 | 1.728E-07 | 2.22E-09 | 0.069 |
| 0.2 | 500.27 | 375.55 | 0.48 | 4.25E-09 | 1.656E-07 | 1.83E-09 | 0.053 |
| 0.3 | 499.71 | 375.28 | 0.42 | 3.10E-09 | 1.584E-07 | 1.46E-09 | 0.039 |
| 0.4 | 499.89 | 375.58 | 0.36 | 2.11E-09 | 1.512E-07 | 1.10E-09 | 0.026 |
| 0.5 | 499.80 | 375.8 | 0.30 | 1.30E-09 | 14.4E-07 | 7.71E-10 | 0.016 |

*Table 0-4. Simulation data as a result of length deformation where the undeformed pore length is 0.8 mm*

| Variation Ratio | Local Pressure | Local Pressure | Block Length | Simulated Local Permeability | Area | Flow Rate | Reynolds |
|---|---|---|---|---|---|---|---|
| $\varepsilon(-)$ | $P_5(Pa)$ | $P_6(Pa)$ | $L_z(mm)$ | $K_L^S(m^2)$ | $A(m^2)$ | $Q(m^3s^{-1})$ | Re(−) |
| 0 | 499.99 | 375.26 | 0.80 | 1.25E-08 | 3.2E-07 | 6.23E-09 | 0.16 |
| 0.1 | 499.83 | 375.21 | 0.72 | 9.90E-09 | 3.072E-07 | 5.26E-09 | 0.12 |
| 0.2 | 499.80 | 374.902 | 0.64 | 7.56E-09 | 2.944E-07 | 4.34E-09 | 0.094 |
| 0.3 | 499.86 | 375.58 | 0.56 | 5.52E-09 | 2.816E-07 | 3.45E-09 | 0.069 |
| 0.4 | 499.68 | 375.46 | 0.48 | 3.75E-09 | 2.688E-07 | 2.61E-09 | 0.047 |
| 0.5 | 500.36 | 376.21 | 0.40 | 2.30E-09 | 2.56E-07 | 1.83E-09 | 0.029 |

*Table 0-5. Simulation data as a result of length deformation where the undeformed pore length is 1.0 mm*

| **Variation Ratio** $\varepsilon(-)$ | **Local Pressure** $P_5(Pa)$ | **Local Pressure** $P_6(Pa)$ | **Block Length** $L_z(mm)$ | **Simulated Local Permeability** $K_L^S(m^2)$ | **Area** $A(m^2)$ | **Flow Rate** $Q(m^3s^{-1})$ | **Reynolds** Re(−) |
|---|---|---|---|---|---|---|---|
| 0 | 499.93 | 375.23 | 1.0 | 1.95E-08 | 5.0E-07 | 1.22E-08 | 0.24 |
| 0.1 | 499.89 | 374.89 | 0.90 | 1.54E-08 | 4.8E-07 | 1.03E-08 | 0.19 |
| 0.2 | 499.79 | 375.07 | 0.80 | 1.18E-08 | 4.6E-07 | 8.48E-09 | 0.15 |
| 0.3 | 499.95 | 375.45 | 0.70 | 8.61E-09 | 4.4E-07 | 6.74E-09 | 0.11 |
| 0.4 | 500.14 | 375.79 | 0.60 | 5.86E-09 | 4.2E-07 | 5.10E-09 | 0.073 |
| 0.5 | 500.14 | 376.49 | 0.50 | 3.60E-09 | 4.0E-07 | 3.57E-09 | 0.045 |

*Table 0-6. Correlation coefficient data for variable porosity case study*

| **Pore Length** $L_0(mm)$ | **Pore Length** $^2$ $L_0^2(mm^2)$ | **Quadratic Coeffcients** $(\mathrm{mm}^2)$ | | | **Normalised Coefficients** $(-)$ | | | **Reynolds** Re(−) |
|---|---|---|---|---|---|---|---|---|
| | | $A_2$ | $A_1$ | $A_0$ | $a_2/L_0^2$ | $a_1/L_0^2$ | $a_0/L_0^2$ | |
| 0.2 | 0.04 | 8.76E-10 | 1.71E-09 | 7.80E-10 | 0.0219 | 0.0428 | 0.0195 | 0.0097 |
| 0.4 | 0.16 | 3.54E-09 | 6.87E-09 | 3.12E-09 | 0.0221 | 0.0429 | 0.0195 | 0.039 |
| 0.6 | 0.36 | 8.03E-09 | 1.55E-08 | 7.03E-09 | 0.0223 | 0.0430 | 0.0195 | 0.088 |
| 0.8 | 0.64 | 1.42E-08 | 2.75E-08 | 1.25E-08 | 0.0222 | 0.0423 | 0.0195 | 0.16 |
| 1 | 1.00 | 2.23E-08 | 4.30E-08 | 1.95E-08 | 0.0223 | 0.0430 | 0.0195 | 0.24 |

*Table 0-7. Simulation Data for a change in length variation ratio from 0 to 0.5 in a 2 element geometry*

| **Length Variation** $\varepsilon(-)$ | **Local Pressure** $P(Pa)$ | **Block Length** $L_z(mm)$ | **Simulated Permeability** $K_S^L(m^2)$ | **Predicted Permeability** $K_P^L(m^2)$ | **Absolute Error** $\delta K(m^2)$ | **Area** $A(m^2)$ |
|---|---|---|---|---|---|---|
| 0 | 1000 | 0 | - | - | - | 3.2E-07 |
| 0 | 942.6 | 0.8 | 1.27E-08 | 1.25E-08 | -0.016E-08 | 3.2E-07 |
| 0 | 884.5 | 0.8 | 1.26E-08 | 1.25E-08 | -0.0045E-08 | 3.2E-07 |
| 0 | 826.4 | 0.8 | 1.26E-08 | 1.25E-08 | -0.00344E-08 | 3.2E-07 |
| 0 | 755.7 | 0.8 | 1.03E-08 | 1.25E-08 | 0.212E-08 | 3.2E-07 |
| 0.5 | 588.2 | 0.4 | 2.72E-09 | 2.2635E-09 | -0.169E-08 | 2.56E-07 |
| 0.5 | 391.5 | 0.4 | 2.32E-09 | 2.2635E-09 | -0.0242E-08 | 2.56E-07 |
| 0.5 | 193.8 | 0.4 | 2.31E-09 | 2.2635E-09 | -0.0192E-08 | 2.56E-07 |
| 0.5 | 0 | 0.4 | 2.35E-09 | 2.2635E-09 | -0.0384E-08 | 2.56E-07 |

*Table 0-8. Simulation data for a 2 element geometry with no length variation*

| Length Variation $\varepsilon(-)$ | Local Pressure $P(Pa)$ | Block Length $L_z(mm)$ | Simulated Permeability $K_S^L(m^2)$ | Predicted Permeability $K_P^L(m^2)$ | Absolute Error $\delta K(m^2)$ | Area $A(m^2)$ |
|---|---|---|---|---|---|---|
| 0 | 1000 | 0 | - | - | - | 3.2E-07 |
| 0 | 876.394 | 0.8 | 1.27234E-08 | 1.2512E-08 | -0.0166 | 3.2E-07 |
| 0 | 750.904 | 0.8 | 1.25324E-08 | 1.2512E-08 | -0.00163 | 3.2E-07 |
| 0 | 625.5809 | 0.8 | 1.25491E-08 | 1.2512E-08 | -0.00295 | 3.2E-07 |
| 0 | 499.8118 | 0.8 | 1.25046E-08 | 1.2512E-08 | 0.000593 | 3.2E-07 |
| 0 | 374.1135 | 0.8 | 1.25116E-08 | 1.2512E-08 | 2.96E-05 | 3.2E-07 |
| 0 | 248.758 | 0.8 | 1.25458E-08 | 1.2512E-08 | -0.00270 | 3.2E-07 |
| 0 | 123.4094 | 0.8 | 1.25465E-08 | 1.2512E-08 | -0.00275 | 3.2E-07 |
| 0 | 0 | 0.8 | 1.27437E-08 | 1.2512E-08 | -0.0182 | 3.2E-07 |

*Table 0-9. Simulation data for a 2 element geometry with a length variation of 0.5*

| Length Variation $\varepsilon(-)$ | Local Pressure $P(Pa)$ | Block Length $L_z(mm)$ | Simulated Permeability $K_S^L(m^2)$ | Predicted Permeability $K_P^L(m^2)$ | Absolute Error $\delta K(m^2)$ | Area $A(m^2)$ |
|---|---|---|---|---|---|---|
| 0.5 | 1000 | 0.4 | - | - | - | 2.56E-07 |
| 0.5 | 876.29 | 0.4 | 2.33E-09 | 2.2635E-09 | -0.0303 | 2.56E-07 |
| 0.5 | 750.5214 | 0.4 | 2.30E-09 | 2.2635E-09 | -0.0142 | 2.56E-07 |
| 0.5 | 625.6034 | 0.4 | 2.31E-09 | 2.2635E-09 | -0.0208 | 2.56E-07 |
| 0.5 | 499.848 | 0.4 | 2.30E-09 | 2.2635E-09 | -0.0143 | 2.56E-07 |
| 0.5 | 374.2608 | 0.4 | 2.30E-09 | 2.2635E-09 | -0.0156 | 2.56E-07 |
| 0.5 | 249.0881 | 0.4 | 2.31E-09 | 2.2635E-09 | -0.0188 | 2.56E-07 |
| 0.5 | 123.6308 | 0.4 | 2.30E-09 | 2.2635E-09 | -0.0166 | 2.56E-07 |
| 0.5 | -1.2E-46 | 0.4 | 2.34E-09 | 2.2635E-09 | -0.0309 | 2.56E-07 |

*Table 0-10. Simulation data for a 2 element geometry with two blocks with a varied length and the remaining blocks unvaried*

| Length Variation $\varepsilon(-)$ | Local Pressure $P(Pa)$ | Block Length $L_z(mm)$ | Simulated Permeability $K_S^L(m^2)$ | Predicted Permeability $K_P^L(m^2)$ | Absolute Error $\delta K(m^2)$ | Area $A(m^2)$ |
|---|---|---|---|---|---|---|
| 0 | 1000 | 0 | | | | 3.2E-07 |
| 0 | 894.5316 | 0.8 | 1.2717E-08 | 1.2512E-08 | -0.0161 | 3.2E-07 |
| 0 | 775.8211 | 0.8 | 1.12984E-08 | 1.2512E-08 | 0.107 | 3.2E-07 |
| 0.3 | 618.5945 | 0.56 | 6.78572E-09 | 5.5163E-09 | -0.187 | 2.816E-07 |
| 0 | 499.9952 | 0.8 | 1.1309E-08 | 1.2512E-08 | 0.106 | 3.2E-07 |
| 0 | 380.6671 | 0.8 | 1.12399E-08 | 1.2512E-08 | 0.113 | 3.2E-07 |
| 0.3 | 223.4717 | 0.56 | 6.78707E-09 | 5.5163E-09 | -0.187 | 2.816E-07 |
| 0 | 105.3537 | 0.8 | 1.13551E-08 | 1.2512E-08 | 0.102 | 3.2E-07 |
| 0 | 5.65E-48 | 0.8 | 1.27308E-08 | 1.2512E-08 | -0.0172 | 3.2E-07 |

*Table 0-11. Simulation Data for a 4 element geometry with non-homogeneous length variation between each element*

| **Length Variation** $\varepsilon(-)$ | **Local Pressure** $P(Pa)$ | **Block Length** $L_z(mm)$ | **Simulated Permeability** $K_S^L(m^2)$ | **Predicted Permeability** $K_P^L(m^2)$ | **Absolute Error** $\delta K(m^2)$ | **Area** $A(m^2)$ |
|---|---|---|---|---|---|---|
| 0 | 1000 | 0 | - | - | - | 1.6E-07 |
| 0 | 958.5117 | 0.8 | 2.56561E-08 | 2.5472E-08 | -0.00718 | 1.6E-07 |
| 0 | 916.5429 | 0.8 | 2.53627E-08 | 2.5472E-08 | 0.00431 | 1.6E-07 |
| 0 | 874.5773 | 0.8 | 2.53647E-08 | 2.5472E-08 | 0.00423 | 1.6E-07 |
| 0 | 831.2756 | 0.8 | 2.56059E-08 | 2.5472E-08 | -0.00523 | 1.536E-07 |
| 0.1 | 783.195 | 0.72 | 2.16198E-08 | 2.0967E-08 | -0.0302 | 1.47456E-07 |
| 0.1 | 733.6191 | 0.72 | 2.09676E-08 | 2.0967E-08 | 0.00003 | 1.47456E-07 |
| 0.1 | 684.015 | 0.72 | 2.09556E-08 | 2.0967E-08 | 0.000541 | 1.47456E-07 |
| 0.1 | 630.8883 | 0.72 | 2.13434E-08 | 2.0967E-08 | -0.0176 | 1.35168E-07 |
| 0.3 | 560.2086 | 0.56 | 1.3611E-08 | 1.28282E-08 | -0.0575 | 1.23904E-07 |
| 0.3 | 484.7032 | 0.56 | 1.2741E-08 | 1.28282E-08 | 0.00685 | 1.23904E-07 |
| 0.3 | 409.2376 | 0.56 | 1.27477E-08 | 1.28282E-08 | 0.00631 | 1.23904E-07 |
| 0.3 | 332.4596 | 0.56 | 1.28212E-08 | 1.28282E-08 | 0.000551 | 1.21088E-07 |
| 0.35 | 247.7806 | 0.52 | 1.10455E-08 | 1.09751E-08 | -0.00638 | 1.18336E-07 |
| 0.35 | 161.8112 | 0.52 | 1.08795E-08 | 1.09751E-08 | 0.00878 | 1.18336E-07 |
| 0.35 | 75.79595 | 0.52 | 1.0874E-08 | 1.09751E-08 | 0.00930 | 1.18336E-07 |
| 0.35 | 0 | 0.52 | 1.05763E-08 | 1.09751E-08 | 0.0377 | 1.18336E-07 |

*Table 0-12. Processed data for a 4 element geometry with non-homogeneous length variation*

| **Length Variation** $\varepsilon(-)$ | **Local Pressure** $P(Pa)$ | **Resistance** $R_i(m^3)$ | **Local Pressure Prediction** $P_p(Pa)$ | **Absolute Pressure Error** $\delta P(Pa)$ |
|---|---|---|---|---|
| 0 | 1000 | - | 1000 | - |
| 0 | 958.5117 | 1.96294E+11 | 958.8056 | 0.2939 |
| 0 | 916.5429 | 1.96294E+11 | 917.6112 | 1.068365 |
| 0 | 874.5773 | 1.96294E+11 | 876.4169 | 1.839571 |
| 0 | 831.2756 | 2.04473E+11 | 833.5061 | 2.230463 |
| 0.1 | 783.195 | 2.32881E+11 | 784.6335 | 1.438458 |
| 0.1 | 733.6191 | 2.32881E+11 | 735.7609 | 2.141794 |
| 0.1 | 684.015 | 2.32881E+11 | 686.8883 | 2.873366 |
| 0.1 | 630.8883 | 2.54052E+11 | 633.5728 | 2.684489 |
| 0.3 | 560.2086 | 3.52319E+11 | 559.6349 | -0.57375 |
| 0.3 | 484.7032 | 3.52319E+11 | 485.697 | 0.993811 |
| 0.3 | 409.2376 | 3.52319E+11 | 411.7591 | 2.521481 |
| 0.3 | 332.4596 | 3.60513E+11 | 336.1017 | 3.642106 |
| 0.35 | 247.7806 | 4.00387E+11 | 252.0763 | 4.295637 |
| 0.35 | 161.8112 | 4.00387E+11 | 168.0508 | 6.23965 |
| 0.35 | 75.79595 | 4.00387E+11 | 84.02542 | 8.229473 |
| 0.35 | 0 | 4.00387E+11 | -2.6E-13 | -2.6E-13 |